

Impact of Electrode Properties on Charge Transport
Dynamics of Molecular Devices

Olgun Adak

Submitted in partial fulfillment of the
requirements for the degree of
Doctor of Philosophy
in the Graduate School of Arts and Sciences

COLUMBIA UNIVERSITY

2016

©2015

Olgun Adak

All rights reserved

ABSTRACT

Impact of Electrode Properties on Charge Transport Dynamics of Molecular Devices

Olgun Adak

This thesis aims to provide insights into two challenging problems in the field of molecular electronics: Understanding the role of the electronic and the mechanical properties of electrodes in determining the charge transport dynamics of molecular devices and achieving the optical control of charge transport through single-molecule junctions by exploiting the optical properties of electrodes.

We start by investigating the impact of electrode band structure on the charge transport characteristics of molecular devices. To this end, we conduct two independent, yet highly related studies. In the first study, we demonstrate how the metallic band structure dictates the molecular orbital coupling at metal-molecule interfaces by studying charge transport through pyridine-based single-molecule junctions with Au and Ag electrodes using a newly developed scanning tunneling microscope-based spectroscopy technique and performing density functional theory calculations. We find that pyridine derivatives couple well to Au electrodes compared with Ag electrodes. The density functional theory calculations show that the increase in the molecular orbital coupling to Au compared with Ag is due to an enhanced density of d-states near the Fermi level resulting from relativistic effects.

Second, we study the interfacial charge transport properties of molecular devices with

metal, semimetal and semiconductor electrodes using X-ray photoemission based spectroscopy techniques. In particular, we probe the hot electron dynamics of 4,4'-bipyrdine on Au (metal), epitaxial graphene (semimetal) and graphene nanoribbon (semiconductor) surfaces. We find that charge transfer from the molecule to the substrate is fastest on the metal surface and slowest on the semiconductor surface. We attribute this trend to a reduced electronic interaction between the molecule and the surface as a results of a decrease in the density of electronic states near the Fermi level as the metallic character of the substrate is reduced. Furthermore, we provide evidence for fast phase decoherence of hot electrons via an interaction with the substrate in these systems.

Third, we shed light onto the origin of flicker noise in single-molecule junctions, tunnel junctions and gold point-contacts at room temperature. We find that the switching of gold atoms between metastable sites in the electrodes due to the thermal energy leads to conductance fluctuations in these systems. We further demonstrate how the flicker noise characteristics of single-molecule junctions can be used to infer the nature of the electronic interaction at metal-molecule interfaces. Specifically, we find that flicker noise exhibits a power dependence on junction conductance that can distinguish between through-space and through-bond charge transport. This work demonstrates how the mechanical properties of electrodes affect charge transport through single-molecule junctions and how noise can be used to understand the electronic properties of metal-molecule interfaces.

Lastly, we explore the possibility of driving currents through single-molecule junctions using electromagnetic radiation. To this end, we perform photocurrent measurements on single-molecule junctions, tunnel junctions and gold point-contacts obtained using the scanning tunneling microscope-based break-junction technique. We find that the primary source of photocurrents in these systems is the laser induced local heating and the subsequent thermal expansion when probed using a lock-in type technique in which the light

intensity is being modulated. We further develop an experimental method that differentiates between the photocurrents due to thermal expansion and the optical currents in single-molecule junctions, and provide evidence for optical currents due to electron-photon interaction during charge transport through single-molecule junctions. By using this method we estimate the plasmonic electric field enhancement factor in single-molecule junctions formed by 4,4'-bipyridine. Our estimate is in very good agreement with values inferred from tip enhanced Raman spectroscopy measurements and field emission measurements.

We believe that the results presented in this thesis provide original insights into the fundamentals of the physics that govern charge transport across metal-molecule interfaces. Furthermore, the new experimental techniques introduced in this thesis offer new ways for investigating the rich physics present in nanoscale systems.

Contents

List of Figures	v
1 Introduction	1
1.1 Theoretical Background	2
1.1.1 Charge Transport in Single-Molecule Junctions	2
1.1.2 Effect of Light on Transport Through Single-Molecule Junctions . .	4
1.2 Experimental Techniques	6
1.2.1 Scanning Tunneling Microscope-Based Break-Junction Technique .	6
1.2.2 X-Ray Photoemission-Based Spectroscopy Techniques	8
1.2.2.1 X-Ray Photoemission Spectroscopy	8
1.2.2.2 Near-Edge X-Ray Absorbance Fine Structure	9
1.2.2.3 Resonant Photoemission Spectroscopy	11
1.3 Outline	13
2 Effect of Metallic Band Structure on Charge Transport Through Single-Molecule Junctions	16
2.1 Preface	16
2.2 Abstract	17
2.3 Introduction	17

2.4	Experimental Technique	20
2.5	Results and Discussion	22
2.6	Conclusion	28
2.7	Methods	29
2.7.1	AC Measurement Technique	29
2.7.2	Theoretical Methods	30
2.8	Supporting Information	31
2.8.1	Experimental Set-up and Measurement Details	31
2.8.2	Two-Dimensional Conductance versus Displacement Histograms . .	33
2.8.3	Derivation of Model Equations	34
2.8.4	Finite Temperature Effects	37
2.8.5	Impact of Bias Voltage on Level Alignment and Coupling in Au Junctions	37
2.8.6	Comparison Between Experimental and Simulated IV's	39
2.8.7	Impact of Asymmetric Coupling on the Experimental Technique .	42
2.8.8	Relativistic and non-Relativistic DFT Calculations	45
3	Charge Transport at Hybrid Interfaces	47
3.1	Preface	47
3.2	Abstract	47
3.3	Introduction	48
3.4	Results and Discussion	50
3.5	Conclusion	57
3.6	Supporting Information	58
3.6.1	Measurement Details and Sample Preparation	58

3.6.2	X-Ray Photoemission Spectroscopy and Near Edge X-Ray Absorption Fine Structure Spectroscopy Measurements	59
3.6.3	RPES Measurement and Data	60
3.6.4	RPES Core-Hole Clock Method with Charge Back Donation	62
4	Flicker Noise Characteristics of Single-Molecule Junctions	66
4.1	Preface	66
4.2	Abstract	67
4.3	Introduction	67
4.4	Experimental Technique	70
4.5	Results and Discussion	71
4.6	Conclusion	81
4.7	Supporting Information	82
4.7.1	Set-up and Measurement Details	82
4.7.2	Gold Point-Contacts with Mechanical Perturbation	87
4.7.3	Scaling of Flicker Noise in Tunnel Junctions	88
4.7.4	Scaling of Flicker Noise in Gold Point-Contacts	89
4.7.5	Voltage Dependence of Flicker Noise	90
4.7.6	DFT Calculation Details	91
4.7.7	Scaling of Flicker Noise in Molecular Junctions	93
4.7.8	Model for Scaling of Flicker Noise Power in Molecular Junctions	95
4.7.9	Rotations and Rupture of the Au-S Linker Bond	99
5	Evidence for Optically Induced Charge Transfer Through Single-Molecule Junctions	102
5.1	Preface	102

5.2	Abstract	102
5.3	Introduction	103
5.4	Results and Discussion	107
5.5	Conclusion	115
5.6	Supporting Information	116
5.6.1	Hot Electron Transport	116
5.6.2	Experimental Set-up	116
5.6.3	Wavelength Dependence of Photocurrent in Gold Point-Contacts and Tunnel Junctions	118
5.6.4	Dependence of the Ratio between Photocurrent and Mechanical Current on Junction Conductance	119
5.6.5	Effect of Reduction in Coupling on Optical Current	120
6	Conclusion and Outlook	123
6.1	Conclusion	123
6.2	Outlook	125
6.3	Complete List of Work	126
	Bibliography	128

List of Figures

1.1	Schematic Representation of the Transmission Model	3
1.2	Transmission Through a Single-Molecule Junction under Electromagnetic Radiation	5
1.3	Formation of a Single-Molecule Junction using the STM-BJ Technique.	6
1.4	A Sample Single-Molecule Junction Trace	7
1.5	Schematic Representation of XPS and NEXAFS	9
1.6	Nitrogen K-Edge NEXAFS Spectrum of 4,4'-Bipyridine	11
1.7	Schematic Representation of RPES	13
2.1	Conductance Histograms of Pyridine-Linked Junctions with Au and Ag Electrodes	19
2.2	AC Spectroscopy: Experimental Technique	21
2.3	Level Alignment and Coupling Strength in 4,4'-Vinylenedipyridine Junctions with Au and Ag Electrodes	24
2.4	DFT-Based Transmission Curves for Pyridine-Linked Junctions with Au and Ag Electrodes	25
2.5	Scattering States and Density of States in 4,4'-Vinylenedipyridine Junctions with Au Electrodes	27
2.6	Block Diagram of STM-BJ Set-up and Circuit Representation	32

2.7	Two-Dimensional Conductance-Displacement Histograms of Pyridine-Linked Junctions	33
2.8	Bias Dependence of Level Alignment and Coupling Strength in 4,4'-Vinylenedipyridine and 4,4'-Bipyridine Junctions with Au Electrodes	39
2.9	Experimental and Simulated IV Histograms for 4,4'-Vinylenedipyridine and 4,4'-Bipyridine Junctions with Au Electrodes	41
2.10	Sorted IV Histograms for 4,4'-Vinylenedipyridine and 4,4'-Bipyridine Junctions with Au Electrodes	43
2.11	Monte Carlo Simulations for Asymmetrical Coupling	45
2.12	DFT-Based Transmission Curves With and Without Relativistic Effects for 4,4'-Vinylenedipyridine	46
3.1	Schematic Representation of Photoemission Processes	50
3.2	The XPS and NEXAFS of 4,4'-Bipyridine on Au, Epitaxial Graphene and Graphene Nanoribbons	51
3.3	Nitrogen K-Edge RPES Line Scans for 4,4'-Bipyridine on Au, Epitaxial Graphene and Graphene Nanoribbons	54
3.4	Angle Dependent Nitrogen K-Edge RPES Measurements on Au and Epitaxial Graphene	56
3.5	Nitrogen K-Edge RPES Spectra for 4,4'-Bipyridine on Au, Epitaxial Graphene and Graphene Nanoribbons	61
4.1	Systems of Study and Frequency Dependence of Conductance Noise	69
4.2	Flicker Noise in Gold Point-Contacts	71
4.3	Low Temperature Noise Measurement in Tunnel Junctions and DFT-Based Atom Dynamics Calculations	75

4.4	Molecular Junctions: Flicker Noise versus Conductance	79
4.5	Block Diagram of STM-BJ and Circuit Representation	83
4.6	Experimental Noise Floor	84
4.7	Flicker Noise versus Conductance in Gold Point-Contacts	88
4.8	Temperature and Voltage Dependence of Flicker Noise in Tunnel Junctions and Gold Point-Contacts	91
4.9	Scaling of Flicker Noise in Molecular Junctions	93
4.10	Scaling of Flicker Noise in Molecular Junctions - Additional Systems . . .	94
4.11	Monte-Carlo Simulations of Flicker Noise	98
4.12	Rotations and Rupture of the Au-S Linker Bond	101
5.1	Systems of Study and Measurement Technique	107
5.2	Photocurrent and Mechanical Current Measurements on Tunnel Junctions and Gold Point-Contacts under 658 nm Light	109
5.3	Photocurrent and Mechanical Current Measurements on BP Single- Molecule Junctions under 980 nm Light	111
5.4	Electrode Push Experiments on BP Single-Molecule Junctions	113
5.5	Block Diagram of Measurement Set-Up	117
5.6	Photocurrent and Mechanical Current Measurements on Tunnel Junctions and Gold Point-Contacts under 405 nm and 980 nm Light	118
5.7	Two-Dimensional Histogram of Junction Conductance against I_P/I_M . . .	120
5.8	Level Alignment and Coupling Strength in BP Single-Molecule Junctions .	121
5.9	Relation between Coupling Strength and the Ratio between the Optical Current and the DC Current	122

Acknowledgements

This thesis would not have been completed if I had not had the opportunity to work under the guidance of my adviser, Prof. Latha Venkataraman. I first would like to extend my gratitude to Prof. Latha Venkataraman for her support and mentorship during my Ph.D. education.

I feel deeply indebted to Prof. Dean Cvekto, Prof. Alberto Morgante and Dr. Gregor Kladnik for their vast contribution to this thesis. I am very grateful to Dr. Mark Hybertsen for his insightful discussions and very glad to have worked with Prof. Ferdinand Evers and Dr. Richard Korytar. And I thank my first research adviser Prof. Phillip Duxbury, without him I would not had the opportunity to meet these excellent scientists.

Finally, I would like to thank my family, especially Ayça, for their immense support, encouragement and believing in me.

Olgun

Ayça'ya

Chapter 1

Introduction

In 2015, IBM announced that they had fabricated the first working chip made of 20 billion transistors with a feature size of 7 nm. Notwithstanding IBM's marvelous achievement, sooner or later silicon-based technology will not be able to meet the demand for miniaturization and will need to be replaced with a new technology. The idea of using molecules as building blocks for electronic circuits stands out as the most appealing and interesting of all. [1]–[4] This is partly due to the rich physics arising from the interplay between many subtle local phenomena at nanoscale and partly due to the immense possibilities for designing organic components that requires lots of imagination and an equivalent amount of synthetic chemistry knowledge. Clearly, the pursuit of commercial organic electronic devices necessitates a complete understanding of the physical processes and the interactions that govern charge transport in molecular junctions and across interfaces containing organic constituents.

In this thesis, we seek to provide new insights into two fundamental problems in the field of molecular electronics. These are understanding the effect of the mechanical and the electronic properties of electrodes on charge transport through molecular devices, and achieving the optical control of charge transport through single-molecule junctions by

CHAPTER 1. INTRODUCTION

exploiting the optical properties of electrodes. The remainder of this section provides a brief theoretical background for charge transport through single-molecule junctions as well as light single-molecule interactions, and introduces the experimental techniques employed in this work.

1.1 Theoretical Background

1.1.1 Charge Transport in Single-Molecule Junctions

A single-molecule junction is a molecule connected to two electrodes; the electrodes are typically gold due to its malleability and resistance to oxidation. The central problem in the field of molecular electronics is understanding how charge is transported from one electrode to the other through the molecule.

Charge transport through a single-molecule junction can be understood by a model where an electron incident from one electrode to the molecule has an energy dependent probability for tunneling across (see Figure 1.1A). [5], [6] The strong energy dependence of the tunneling probability is a consequence of discrete molecular orbitals that hybridize with the electrode bands. In fact, it is the hybridization that allows for charge transport through a single-molecule junction. [7] Equally important in determining the charge transport properties of a single-molecule junction is the alignment of the molecular orbitals relative to the Fermi level of the system. [7] The level alignment is determined by the molecule's internal electronic structure [8]–[12], the band structure of the electrodes [13]–[17] and the interplay between local phenomena including surface dipole formation, static and dynamic charge screening by the electrodes, charge donation to the molecule, the Coulomb blockade effects, the Kondo effect, and the Stark effect. [18]–[24]

CHAPTER 1. INTRODUCTION

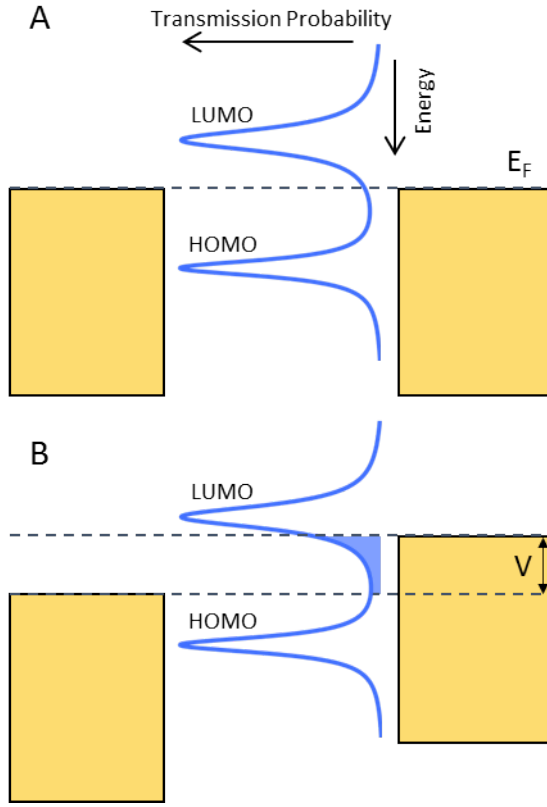


Figure 1.1: Schematic representation of the transmission model. (A) Zero-bias, equilibrium system. (B) System driven out of equilibrium with an external bias voltage.

In this transmission model, externally biasing a single-molecule junction results in a net current due to the difference between the electrode chemical potentials as shown in Figure 1.1B. The DC current through the junction is given by [6], [25], [26]

$$I(V) = \frac{2e}{h} \int_{-\infty}^{\infty} [f(E + eV/2) - f(E - eV/2)]T(E)dE \quad (1.1)$$

where $f(E)$ denotes the Fermi-Dirac distribution function, $T(E)$ is the energy dependent transmission function, V is the bias voltage.

Therefore, in this picture, understanding the charge transport characteristics funda-

CHAPTER 1. INTRODUCTION

mentally boils down to understanding how the electronic, optical and mechanical properties of single-molecule junctions impact the transmission function.

1.1.2 Effect of Light on Transport Through Single-Molecule Junctions

When light is incident onto a single-molecule junction, there are two separate effects that could alter the junction conductance. The first effect is optically induced transitions in the electrodes. This leads to the electronic heating as well as the creation of a hot electron population above the Fermi level. [27] Incorporating this effect into the transmission model is straightforward and involves replacing the equilibrium Fermi-Dirac distribution functions with the non-equilibrium ones in Eq. 1.1. However, due to the fast relaxation of hot electrons in metals, it is not possible to create a substantial steady state hot electron population without heating the lattice significantly. [27]–[32]

The second effect of the incident electromagnetic radiation is the creation of a photovoltage between the electrodes which oscillates at the radiation frequency. [33] The presence of this AC voltage between the electrodes opens up the possibility for electrons to absorb or emit photons during transport. [33] This effect is very similar to the first one with a minor but crucial difference: In the second case, the hot electron is transported before interacting with the electron and the phonon bath. Therefore, the second mechanism does not suffer from the fast relaxation of hot electrons in metals.

In the presence of an optical AC voltage across the junction, the junction current under an external bias voltage is given by [34], [35]

$$I(V) = \frac{2e}{h} \int_{-\infty}^{\infty} \sum_{n=-\infty}^{\infty} J_n \left(\frac{eV_{opt}}{\hbar\omega} \right) (f(E + eV/2) - f(E - eV/2)) T(E + n\hbar\omega) dE \quad (1.2)$$

CHAPTER 1. INTRODUCTION

where V_{opt} is the optical voltage that builds across the junction due to the electromagnetic radiation, J_n denotes the n^{th} order Bessel function of the first kind which gives the transition amplitude for emitting and absorbing n photons during transport, ω is the light frequency, $f(E)$ denotes the Fermi-Dirac distribution function, $T(E)$ is the energy dependent transmission function and V is the external bias voltage.

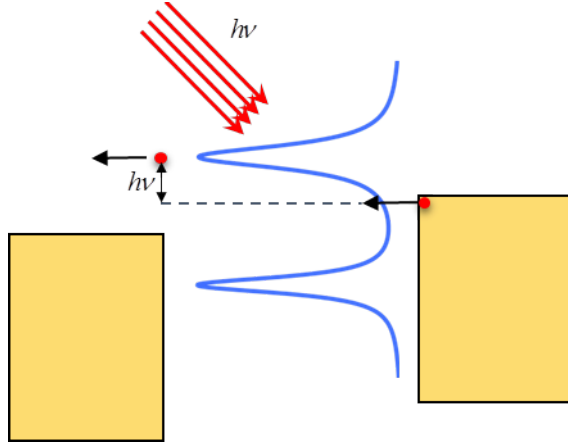


Figure 1.2: Transmission through a single-molecule junction under electromagnetic radiation

Eq. 1.2 implies that an electron that undergoes an optical transition is transported through the junction with an effective probability determined by its final energy. Figure 1.2 is the schematic representation of the case where an electron is transported with unity probability upon absorbing a photon. Therefore, in principle, the conductance of a single-molecule junction can be enhanced by matching the photon energy with a molecular orbital energy. Thus, the question that we aim to address is whether the photovoltage generation in single-molecule junctions formed using the scanning tunneling microscope-based break-junction (STM-BJ) technique is large enough to result in a significant or a measurable photocurrent.

1.2 Experimental Techniques

1.2.1 Scanning Tunneling Microscope-Based Break-Junction Technique

The STM-BJ technique is a very powerful and versatile tool for investigating the transport properties of single-molecule junctions. [36]–[41] Using this technique, single-molecule junctions can be formed rapidly, allowing us to probe a large number of single-molecule junctions to draw statistically significant conclusions. [42] Furthermore, an STM-BJ setup can be readily modified to perform thermoelectricity, spin transport or Raman spectroscopy measurements. [38], [43]–[45]

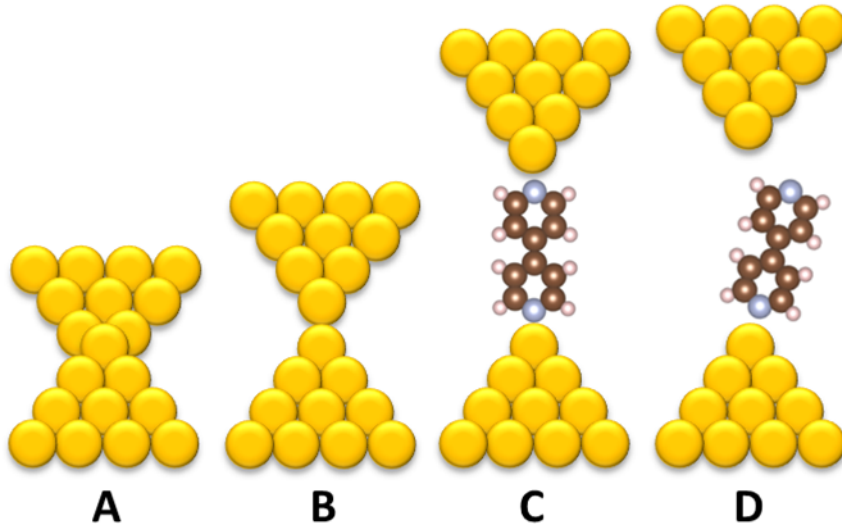


Figure 1.3: Formation of a single-molecule junction using the STM-BJ technique. (A) A gold point-contact. (B) A single atom gold point-contact. (C) A single-molecule junction. (D) A broken single-molecule junction.

The STM-BJ technique involves moving a metal tip in and out of contact with a metal substrate while measuring the current through the junction under an external bias voltage

CHAPTER 1. INTRODUCTION

(see Figure 1.3). [36], [37] As the tip is retracted from the substrate, the metal junction thins out and the conductance of the junction drops in steps of $2e^2/h$ (G_o). The discrete decrease in conductance is due to the quantization of conductance in a one-dimensional mesoscopic conductor. [46]–[48] The thinning out continues until a point-contact forms. Upon further elongation, the junction ruptures and opens up a sub-nanometer gap. In the presence of a molecular solution, a molecule could bridge the gap and form a molecular junction. In order to probe the charge transport properties of a single-molecule junction, a stable junction needs to be maintained. To achieve this, the junction elongation procedure is paused at a position where a stable single-molecule junction is expected to form (see Figure 1.4 for a representative single-molecule junction trace).

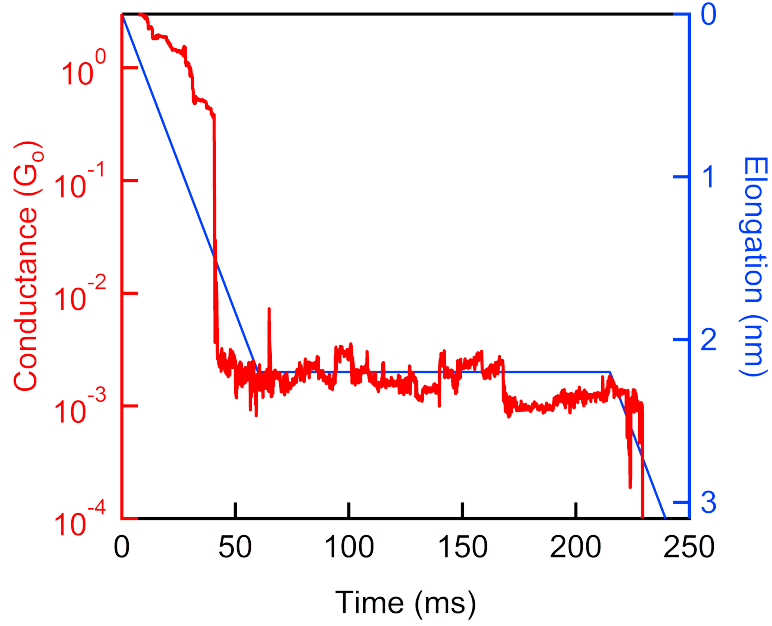


Figure 1.4: A sample single-molecule junction trace formed by 4,4'-di(methylthio)stilbene and Au electrodes. The elongation procedure is paused for 160 ms after elongating the junction for 2.2 nm.

In all STM-BJ-based studies in this thesis, we perform spectroscopy on stable single-

CHAPTER 1. INTRODUCTION

molecule junctions. The spectroscopy may involve shining light onto the junction to measure photocurrents through it, applying an AC voltage across the junction to probe its transport parameters or measuring the junction current to probe the noise characteristics.

1.2.2 X-Ray Photoemission-Based Spectroscopy Techniques

In this thesis, we use three X-ray photoemission-based photoemission techniques to probe charge transport across hybrid interfaces containing organic constituents: X-ray photoemission spectroscopy (XPS), near-edge X-ray absorbance fine structure (NEXAFS) spectroscopy and resonant photoemission spectroscopy (RPES). The primary advantage of using X-ray-based techniques for studying charge transport across interfaces is that using these techniques, we can probe the electronic structure as well as the hot electron dynamics of the interface. [49]–[52]

1.2.2.1 X-Ray Photoemission Spectroscopy

X-ray photoemission spectroscopy (XPS) is a surface science technique based on the photoelectric effect. [50], [53]–[55] In XPS, the surface of interest is illuminated with a monochromatic synchrotron X-ray beam and the kinetic energy of electrons emitted from the surface is measured using an electron analyzer (see Figure 1.5). The measured kinetic energy of the emitted electrons is then converted to the electron binding energy by subtracting the photon energy and the sample work function. XPS is a surface sensitive technique, because electrons emitted below the surface lose their energy rapidly due to inelastic scattering events inside the material and cannot reach the electron analyzer. [54] In this thesis, XPS is used to determine the chemical composition of the surface and quantify the local electrostatic screening effects. [56]

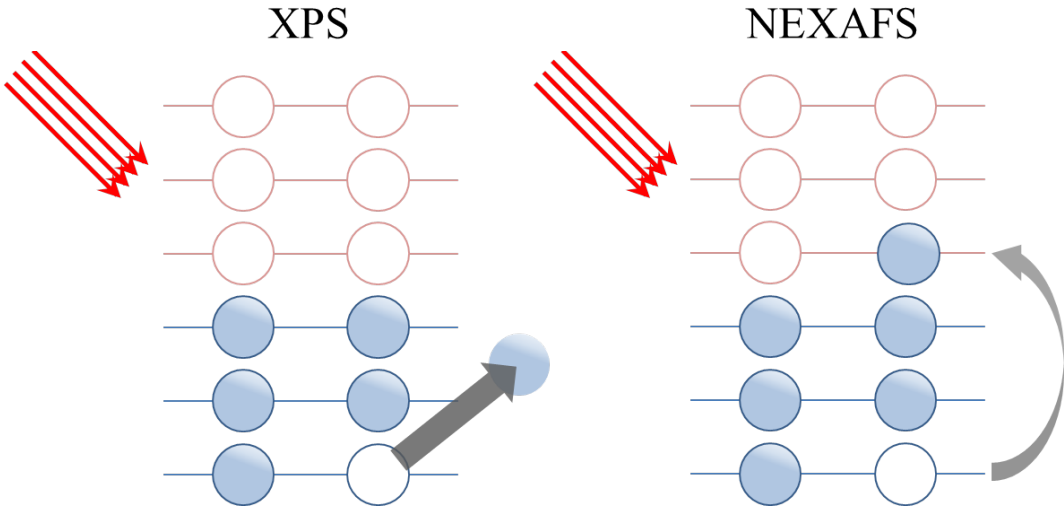


Figure 1.5: Schematic representation of XPS and NEXAFS

1.2.2.2 Near-Edge X-Ray Absorbance Fine Structure

In near-edge X-ray absorbance fine structure (NEXAFS), instead of directly emitting an electron from an occupied orbital, an internal transition is induced in the system; this involves exciting a core-level electron to an unoccupied energy level (see Figure 1.5). This excited state decays via emission of electrons or photons. By measuring the number of emitted electrons as a function of the photon energy, one can obtain the internal absorption spectrum of the system across a particular excitation edge. [57], [58] This spectrum corresponds to a set of internal transition probabilities from a core-level as a function of the photon energy, and thus maps the unoccupied molecular orbitals relative to the core-level.

The transition probability from an occupied orbital to an unoccupied orbital can be obtained from the Fermi's golden rule [51]

$$P_{if} = \frac{2\pi}{\hbar} | < f | V | i > |^2 \sigma_f(E) \quad (1.3)$$

CHAPTER 1. INTRODUCTION

Here, $|i\rangle$ and $|f\rangle$ are the initial and final states of the transition, $\sigma_f(E)$ is the density of final states and V is the time dependent perturbation induced by a plane electromagnetic wave.

When the X-ray wavelength is much larger than the core electron shell diameter, the electric dipole approximation is valid and the transitions are subject to the dipole transition rules. [51] Therefore, the optical transition probabilities have a strong dependence on the light polarization. [51] This strong polarization dependence can be used to determine the molecular orientation on a surface. [59]

In Figure 1.6, the nitrogen K-edge NEXAFS spectrum for 4,4'-bipyridine on an Au(111) surface is shown with s-polarized and p-polarized light. We see that in s-polarization, the N1s to LUMO* transition (399 eV) is strongly suppressed. We know that the LUMO of 4,4'-bipyridine has π character with its nodal plane coinciding with the molecular aromatic ring. [60] Thus, this transition is forbidden with light polarized in the plane of the aromatic ring (*s-pol*) which implies that the molecules lay approximately flat on the surface.

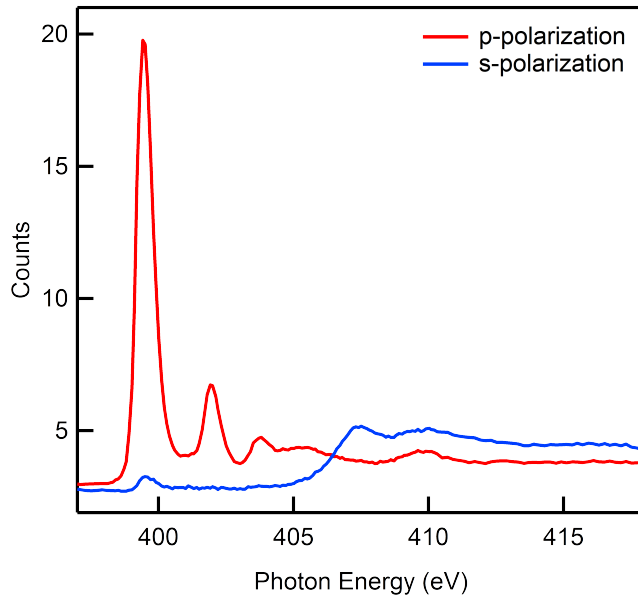


Figure 1.6: Nitrogen K-edge NEXAFS spectrum for 4,4'-bipyridine with s-polarized and p-polarized light

1.2.2.3 Resonant Photoemission Spectroscopy

Resonant photoemission spectroscopy (RPES) is central to probing the hot electron dynamics of interfaces. This technique allows us to measure the interfacial charge transfer time with femtosecond accuracy. [61]–[68] This is achieved by inducing internal transitions in the system at different photon energies, similar to NEXAFS, and measuring the kinetic energy distribution of the emitted electrons due to the relaxation of the excited system, similar to XPS. Therefore, in an RPES measurement, a two dimensional map of electron yield as a function of the photon energy and the electron kinetic energy is obtained.

After a core-electron is excited to an unoccupied molecular orbital or to the free electron continuum via an optical transition which leaves a core-hole in the molecule, the system decays by filling the core-hole and emitting a photon or an electron. There are two primary decay channels in an isolated molecular system that involves the emission

CHAPTER 1. INTRODUCTION

of an electron (see Figure 1.7). The first process is the filling of the core-hole and the subsequent emission of an electron, leaving the LUMO empty; this decay process is called participator decay. The second decay process results in the filling of the core-hole and the subsequent electron emission, leaving the system with two holes and an additional electron in the LUMO; this decay process is called spectator decay.

A third possibility arises when the molecule is electronically coupled to the substrate. In this case, if the electronic coupling is strong enough, the excited electron can escape to the substrate before filing the the core-hole. This leads to the suppression of the participator and the spectator decays. Therefore, by comparing the participator intensities in the isolated system and the coupled system, the charge transfer time across the interface can be obtained using the core-hole clock implementation of the RPES technique. [52]

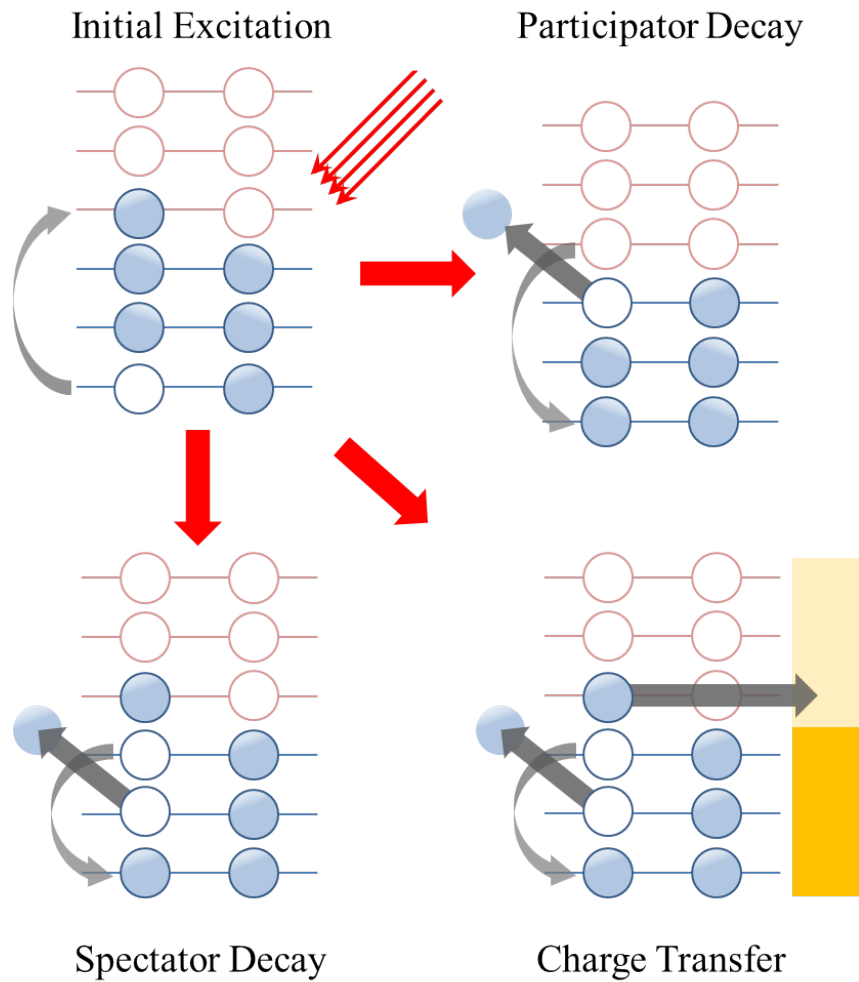


Figure 1.7: Schematic representation of RPES

1.3 Outline

The remainder of this thesis focuses on understanding how the mechanical, electronic and optical properties of electrodes come into play in determining the charge transport characteristics of molecular devices and is comprised of five chapters as follows:

In **Chapter 2**, we investigate the importance of the electrode band structure on

CHAPTER 1. INTRODUCTION

the charge transport properties of single-molecule junctions. In particular, we probe how the conductance of three pyridine-based single-molecule junctions is altered when Au electrodes are replaced with Ag electrodes. Using a newly developed spectroscopy technique, we show that pyridine-based junctions couple strongly to Au compared with Ag due to an enhanced density of d-states near the Fermi level dictated by relativistic effects.

In **Chapter 3**, we present our study of charge transport across metal/organic, semimetal/organic and semiconductor/organic interfaces. We focus on 4,4'-bipyridine (organic) on Au (metal), on epitaxial graphene (semimetal), and on graphene nanoribbon (semiconductor) surfaces. Our main finding is that interfacial charge transfer becomes slow as the metallic character of the substrate is reduced; this is likely due to a decrease in the density of electronic states near the Fermi level, leading to a reduction in the electronic interaction between the molecule and the substrate. Finally, we provide evidence for fast hot electron phase decoherence via an interaction with the substrate in these systems.

In **Chapter 4**, we present our study of flicker noise in single-molecule junctions. In this work, we first reveal the mechanism behind flicker noise in single-molecule junctions, tunnel junctions and gold point-contacts at room temperature. Next we describe how flicker noise can be used to distinguish between through-space and through-bond charge transfer at metal-molecule interfaces. This work demonstrates how the mechanical properties of electrodes effect the conductance of single-molecule junctions and how noise can be used to infer the nature of the electronic interaction at metal-molecule interfaces.

In **Chapter 5**, we investigate the possibility of driving currents through single-molecule junctions using electromagnetic radiation. We first demonstrate that in lock-in type measurements in which the intensity of the electromagnetic radiation is being modu-

CHAPTER 1. INTRODUCTION

lated, local heating and the subsequent thermal expansion lead to spurious photocurrents. Next, we develop an experimental technique that distinguishes between the photocurrents resulting from laser induced local heating and the optical currents resulting from the changes in the electron transport dynamics of the junction. Using this technique, we first provide evidence for optical currents due to photon absorption of electrons during tunneling through 4,4'-bipyridine junctions. We further estimate the plasmonic electric field enhancement factor in these junctions to be around 20; this is in good agreement with the values obtained from tip enhanced Raman spectroscopy and field emission measurements.

We end this thesis with a summary and a brief outlook in **Chapter 6**.

Chapter 2

Effect of Metallic Band Structure on Charge Transport Through Single-Molecule Junctions

2.1 Preface

This chapter is based on the manuscript entitled *Impact of Electrode Band Structure and Relativistic Effects on Transport through Pyridine-Linked Single-Molecule Junctions* by Olgun Adak, Richard Korytar, Andrew Y. Joe, Ferdinand Evers, and Latha Venkataraman published in Nano Letters. [69]. The experimental work was done by Olgun Adak and Andrew Y. Joe. Theoretical work was conducted by Richard Korytar and Ferdinand Evers at Karlsruhe Institute for Technology, Karlsruhe, Germany.

2.2 Abstract

We study the impact of electrode band structure on transport through single-molecule junctions by measuring the conductance of pyridine-based molecules using Ag and Au electrodes. Our experiments are carried out using the scanning tunneling microscope-based break-junction technique and are supported by density functional theory-based calculations. We find from both experiments and calculations that the coupling of the dominant transport orbital to the metal is stronger for Au-based junctions when compared with Ag-based junctions. We attribute this difference to relativistic effects, which result in an enhanced density of d-states at the Fermi energy for Au compared with Ag. We further show that the alignment of the conducting orbital relative to the Fermi level does not follow the work function difference between two metals and is different for conjugated and saturated systems. We thus demonstrate that the details of the molecular level alignment and electronic coupling in metal-organic interfaces do not follow simple rules, but are rather the consequence of subtle local interactions.

2.3 Introduction

Understanding the interplay between different phenomena that govern charge transport at metal-molecule interfaces is fundamentally important for creating functional organic electronic devices. [5], [70], [71] The charge transport properties of metal point-contacts and metal/molecule interfaces are dictated by the band structure of the metal [13]–[17], [46], [72], [73] and the electronic structure of the molecule, [8]–[12] along with many local effects arising from their interaction such as hybridization, dynamic and static charge screening, surface dipole formation. [18]–[21] Here, we study charge transport through pyridine-terminated systems with conjugated and saturated backbones. Specifically we compare

CHAPTER 2. EFFECT OF METALLIC BAND STRUCTURE ON CHARGE TRANSPORT THROUGH SINGLE-MOLECULE JUNCTIONS

the experimental and theoretical charge transport properties of 4,4'-vinylenedipyridine (**1**), 4,4'-bipyridine (**2**), and 4,4'-ethylenedipyridine (**3**) with Au and Ag electrodes to investigate how the band structure of the metal mediates charge transport in single-molecule junctions. We find that the conductance of the conjugated molecules; **1** and **2**, is greatly reduced when bound to Ag electrodes compared to Au electrodes; while conductance of **3**, which has a saturated bridge, is not changed significantly. To understand the origin of these trends, we probe the energy level alignment of the conducting molecular orbital and its coupling strength to the electrodes in these systems through a combination of experiment and density functional theory (DFT) calculations. We find that all systems exhibit significantly enhanced molecular orbital coupling to Au compared to Ag due to an enhanced density of d-states of Au around and above the Fermi energy. In the conjugated systems, we show that the level alignment is similar for both metals; for the saturated system, however, the lowest unoccupied molecular orbital (LUMO), which mediates the charge transfer, is significantly closer to the Fermi level with Ag electrodes. For the conjugated systems, this results in a smaller conductance for the Ag junctions; while for the saturated system, the measured conductance values are similar because the reduction in the molecular orbital coupling strength is compensated by the change in the alignment of the LUMO relative to the metal Fermi level.

CHAPTER 2. EFFECT OF METALLIC BAND STRUCTURE ON CHARGE TRANSPORT THROUGH SINGLE-MOLECULE JUNCTIONS

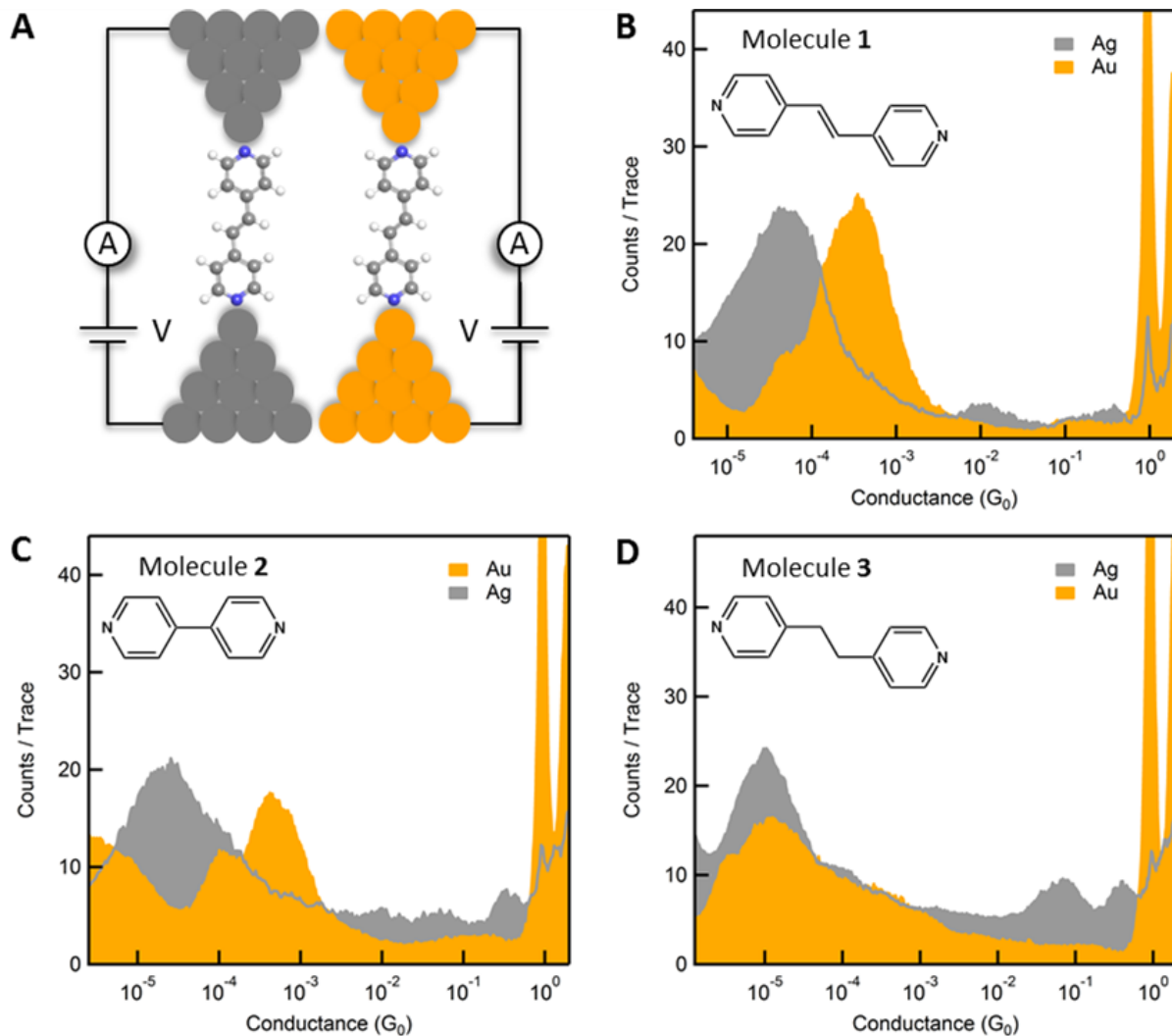


Figure 2.1: (A) Schematic of molecular junctions formed using the STM-BJ technique. (B-D) Logarithmically binned conductance histograms for measurements of Ag and Au junctions formed with molecules 1, 2 and 3, respectively. Inset shows molecular structures. Note that histograms with Ag metal show additional features around 1 - 10 G_0 due to the formation of junctions with oxygen incorporated in parallel or series. [74]

2.4 Experimental Technique

In this work, single-molecule junctions are created using the scanning tunneling microscope-based break-junction technique (STM-BJ), where a Au/Ag tip is repeatedly moved in and out of contact with a Au/Ag substrate in a molecular solution (see Figure 2.1 for schematic and Figure 2.6A for details). [36] A metal point-contact is first formed and once this is broken, a molecule could bridge the gap between the broken electrodes to form a single-molecule junction. Thousands of conductance versus displacement traces are obtained from these repeated measurements and compiled into logarithmically binned one-dimensional histograms [9] without data selection for each system (see Figure 2.1B-D). We observe a clear peak in the conductance histogram, which is a signature of single-molecule junction formation (see Figure 2.7 for two-dimensional conductance-displacement histograms). All molecules show a double-peak conductance signature with Au electrodes, as has been previously demonstrated for pyridine-terminated molecules. [75] The lower peak is attributed to a vertical junction geometry, while the higher peak is due to a tilted junction geometry, which enhances the coupling to the electrodes. [76] The absence of such a double-peak with silver electrodes indicates that there is likely no distinct transition from tilted to vertical geometry during elongation which could be due to the reduced molecule-electrode van der Waals interaction for silver. [77], [78] For **1** and **2**, we find that Au junctions have a higher conductance than Ag junctions, as shown in Figure 2.1B, C, while **3** shows the same conductance with both metals (Figure 2.1D).

CHAPTER 2. EFFECT OF METALLIC BAND STRUCTURE ON CHARGE TRANSPORT THROUGH SINGLE-MOLECULE JUNCTIONS

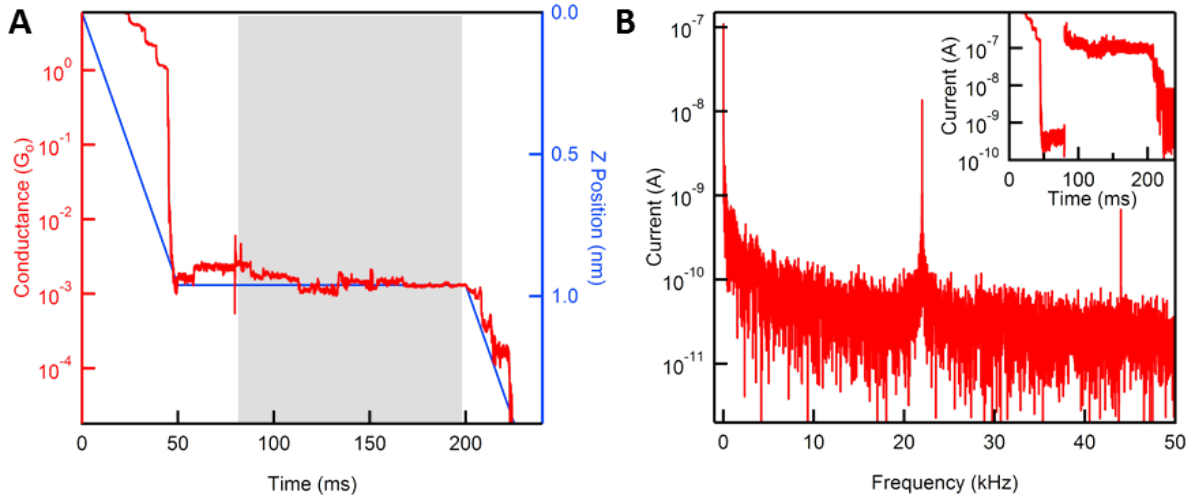


Figure 2.2: (A) A representative conductance and displacement trace plotted against time for the modified break-junction technique. An AC voltage is applied between 80 and 200 ms as indicated by the shaded gray region. (B) Inset: Current measured for the trace shown in (A). The magnitude of the DC current when the AC voltage is applied is around $10^{-7} A$. Main Panel: Frequency domain representation of the current measured while the AC voltage is applied. The first and second harmonic peaks at 22 kHz and 44 kHz with magnitude around $10^{-8} A$ and $10^{-9} A$ are clearly visible in the frequency domain. These values are used to determine the level alignment and the molecular orbital coupling as detailed in the text.

Charge transport through a molecule bonded to metal electrodes involves a coherent transmission of electrons/holes from one lead to the other through the molecular orbital that dominates transport. Often, the transmission probability can be described using a Lorentzian form with only two parameters: the alignment of the molecular orbital relative to the metal Fermi level (E_{level}) and the broadening of this orbital due to hybridization

CHAPTER 2. EFFECT OF METALLIC BAND STRUCTURE ON CHARGE TRANSPORT THROUGH SINGLE-MOLECULE JUNCTIONS

with the metal electrode (Γ). [79], [80]

$$T(E) = \frac{\Gamma^2/4}{(E - E_{level})^2 + \Gamma^2/4} \quad (2.1)$$

Depending on E_{level} and Γ , the current-voltage characteristics could be highly non-linear; [81], [82] in such cases, they can be used to determine the junction transport parameters. [83] Here, we demonstrate a new and general experimental method that employs AC techniques to determine the transport parameters. Unlike measurements of conductance and thermopower that allow one to obtain junction transport parameters, our method is applicable not only in the STM-BJ technique but also for molecular junctions formed using the mechanically controlled, [73], [84] and electromigrated break-junction method. [85], [86] We apply an AC voltage in addition to a DC voltage across the molecular junction and measure the current over a bandwidth larger than twice the AC voltage frequency. We use a modified break-junction technique for these measurements where instead of pulling the tip continuously away from the substrate, the tip is held at fixed displacement after the junction is pulled apart as illustrated in Figure 2.2A. The current through the junction is then measured using a 50 kHz bandwidth while a 150 mV AC voltage is applied at 22 kHz in addition to a 1 V DC voltage. The currents at the first and second harmonic frequencies are obtained by looking at the frequency domain representation of the measured current using the discrete Fourier transform (Figure 2.2B). By using these, we obtain E_{level} and Γ following the procedure detailed in Section 2.7.

2.5 Results and Discussion

We first determine E_{level} and Γ in molecules **1** and **2** with Au electrodes. These systems have been well studied experimentally and shown to have transmission functions that

CHAPTER 2. EFFECT OF METALLIC BAND STRUCTURE ON CHARGE TRANSPORT THROUGH SINGLE-MOLECULE JUNCTIONS

are well approximated by a single-Lorentzian form allowing us to benchmark the AC measurement technique. [22], [75], [76], [87] For these systems, we do not see any evidence that the low conducting vertical geometry junctions sustain the entire fixed displacement section. This is not surprising since these low-conducting junctions form at the apex of the electrodes, and there is no room for mechanical and thermal perturbations. We therefore focus our analysis on junctions in the tilted, high-conducting geometry. We find that on average E_{level} and Γ are 1.1 eV and 40 meV for **1**, while 1.2 eV and 60 meV for **2** with Au electrodes. These values are in good agreement with previously reported values for these systems measured under zero external bias. [87] This is interesting because in our measurements, these systems are driven out of equilibrium under the high applied DC bias. There are several effects that would alter the transport characteristics of a single-molecule junction under high bias voltages. First, under an external electric field, the molecular energy levels could be Stark-shifted. [22] Second, the external electric field could polarize the molecule and change the molecular orbital coupling strengths. [88] Third, charging of molecular orbitals due to the external bias voltage could modify the level alignment. [89] Fourth, molecular vibrational modes could get excited due to an increase in the local temperature or due to inelastic scattering of electrons; this would result in sharp features in the dG/dV spectrum. [40], [90] As detailed in Section 2.8.5, control AC measurements performed at different bias voltages show that the effect of bias voltage on the level alignment is small and the transmission characteristics measured at high bias voltages reflect the zero bias transmission. In addition, current-voltage measurements of these systems show that a slight asymmetry in the coupling to the two electrodes does not impact the results presented here (see Section 2.8.7).

CHAPTER 2. EFFECT OF METALLIC BAND STRUCTURE ON CHARGE TRANSPORT THROUGH SINGLE-MOLECULE JUNCTIONS

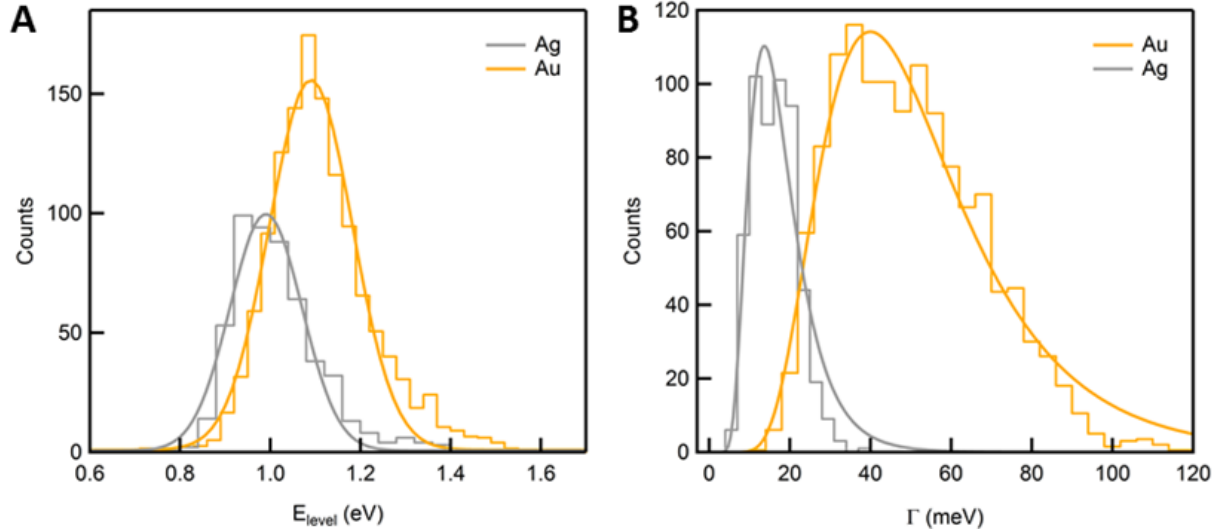


Figure 2.3: Histograms of (A) the energy of the LUMO relative to the metal Fermi level (E_{LUMO}) and (B) the molecular orbital coupling (Γ) for Ag and Au junctions with molecule 1.

Having established that our method yields accurate transport parameters, we next use it to probe E_{level} and Γ in molecule **1** with Ag electrodes as the transmission in this system is well approximated by a single-Lorentzian as will be shown further below. We find that E_{level} and Γ are 1.0 eV and 14 meV respectively (see Figure 2.3A, B). For **2** with Ag, we cannot determine E_{level} and Γ due to a signal-to-noise limitation of our instrument as the current at the second harmonic frequency is at or below the experimental noise floor. This is consistent with the fact that **2** with Ag exhibits even smaller conductance than **1** with Ag. We note that the difference in the LUMO energies relative to the Fermi level between Au and Ag junctions for **1** is quite small (0.1 eV) compared to the work-function difference between the two metals, which is reported as ranging from 0.6 eV to 0.8 eV. [89]

To gain further understanding into charge transfer characteristic of these systems, we turn to DFT calculations of model junctions for all three molecules bound to both Au and Ag electrodes (see Section 2.7 for details). We show in Figure 2.4, the transmission

CHAPTER 2. EFFECT OF METALLIC BAND STRUCTURE ON CHARGE TRANSPORT THROUGH SINGLE-MOLECULE JUNCTIONS

curves for all three molecules bound in a vertical geometry. Although this geometry is different from the one studied experimentally, the trends in our theoretical results across the two electrode materials are independent of the actual junction geometry as has been shown earlier. [76] On a qualitative level we see that in all cases the conductance is dominated by the LUMO. Moreover, for molecules **1** and **2**, the transmissions functions are reasonably well approximated by single-Lorentzians as visible from the fits overlaid, which validates the single-Lorentzian assumption for the experimental method. For molecule **3**, the peak shape is more complicated because of the proximity of higher unoccupied molecular orbitals. We see that for all molecules the LUMO level broadening is larger with Au than with Ag. Specifically, the Lorentzian fits comparing Au and Ag transmissions indicate that the broadening is larger by about a factor of two for **1** and **2**. This is surprising because the Ag-N and Au-N bonding lengths differ only by 2%, and the total density of states of Ag and Au near the Fermi energy differ by roughly 10%.

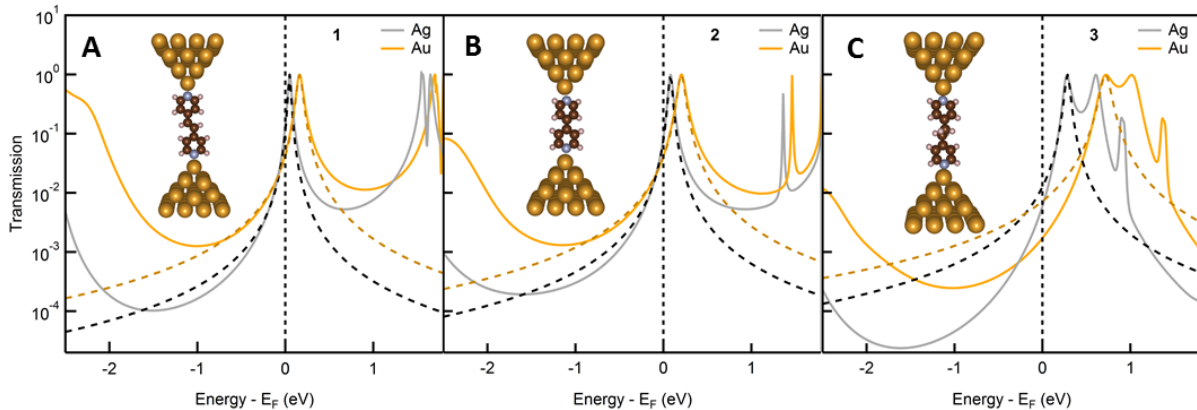


*Figure 2.4: Calculated DFT-based transmission curves for Au and Ag junctions formed with (A) **1**, (B) **2**, and (C) **3**. Dashed lines are Lorentzian fits to the data. Inset: Junction structure for each system is shown with Au.*

To understand the origin of this difference between Au and Ag electrodes, we look

CHAPTER 2. EFFECT OF METALLIC BAND STRUCTURE ON CHARGE TRANSPORT THROUGH SINGLE-MOLECULE JUNCTIONS

at the cluster eigenstates with energies close to the transmission resonance, and focus on junctions formed with **1** (Figure 2.5A). We see that on the molecule the eigenstates resemble the LUMO of the gas-phase. For the Au junction, the wave function on the apex atom has angular nodes which are characteristic of $Au - d_{yz}$. In addition, one can see the presence of the $Au - p_y$ orbital because the lobes that point to the molecule are bigger. These orbitals have the right symmetry to couple to the LUMO. In the case of Ag, we also see four lobes reminiscent of an $Au - d_{yz}$ orbital on the apex atom; however, these are rotated, which diminishes the coupling to the LUMO. These eigenstates indicate the importance of the d-states in hybridizing with the LUMO. In the next step, we look at the density of states of the apex orbitals involved in coupling. We focus here on the apex atom as pyridines bind selectively to under-coordinated gold atoms. [76] As shown in Figure 2.5B, we observe that the spectral density of the d_{yz} -states is three times larger in Au than in Ag while the p_y -states have very similar spectral density at the Fermi level. The enhanced presence of d-states in Au is due to the higher position of the d-band edge, reflecting known relativistic effects. [91], [92] To demonstrate the role of relativity, we perform nonrelativistic DFT calculations for molecule **1**. We observe that the relativistic corrections increase the width of the LUMO by 48% with Au, whereas with Ag the width is enhanced only 10% (see Figure 2.12). Therefore, we conclude that Au gives rise to an enhanced level broadening due to the larger contribution of d-states at the Fermi level. We note here that past DFT calculations that have compared the transmission of junctions formed with **2** using Pt and Au electrodes have found a similar increase in coupling with Pt when compared with Au, which was also attributed to an enhanced density of d-states at the Fermi level. [13]

CHAPTER 2. EFFECT OF METALLIC BAND STRUCTURE ON CHARGE TRANSPORT THROUGH SINGLE-MOLECULE JUNCTIONS

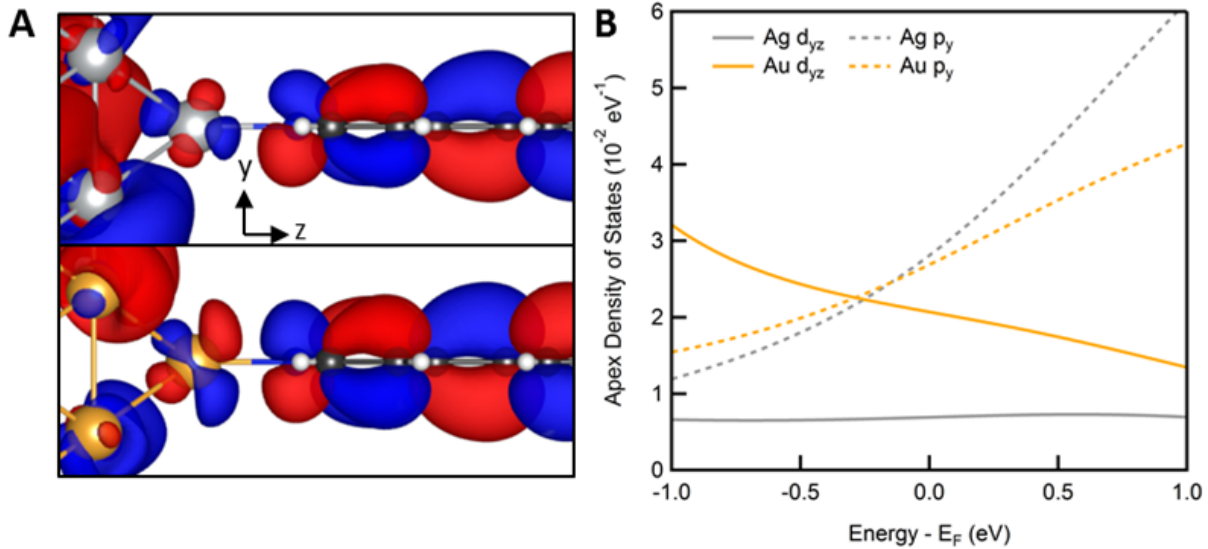


Figure 2.5: (A) Isosurface plots of scattering state close to the resonance for molecule 1 junctions with Ag (top) and Au (bottom). (B) Density of states for d_{yz} and p_y orbitals in Au and Ag.

We cannot extend our theoretical analysis to compare the level alignment across these molecules, because these are inaccurate due to approximations inherent in the exchange-correlation functionals. Specifically, the DFT-based HOMO and LUMO are artificially close to the Fermi level due to self-interaction and polarization errors. [93]–[95] Therefore, one cannot take the transmission value at E_F as a measure of conductance or shift E_F along the transmission curve to estimate conductances for these systems since this would bring E_F too close to the occupied orbitals. However, both the polarization correction and the self-interaction errors are molecule specific, and thus one would expect these to be largely unaffected by the nature of the electrode material as long as the electrode is a metal. Therefore, we can compare the level alignment for a given molecule with different metal electrodes, while keeping in mind that the absolute level alignment is not correct. Our experimental analysis of molecule 1 has shown that the level positions differ only

CHAPTER 2. EFFECT OF METALLIC BAND STRUCTURE ON CHARGE TRANSPORT THROUGH SINGLE-MOLECULE JUNCTIONS

by 0.1 eV between Ag and Au and a similar small difference is obtained from the DFT calculations as well. This is much smaller than the work-function difference between Ag and Au. For **3**, we see that LUMO is 0.4 eV closer to the Fermi level with Ag compared to Au while the coupling for Ag is smaller than that of Au. Thus, for **3**, the reduction in coupling compensates the change in the level alignment explaining the similar measured conductances with Au and Ag electrodes.

2.6 Conclusion

By comparing the experimental and calculation results presented here, we find that the molecule-metal coupling strength is largely controlled by the metal density of states. However, unlike what one would expect for noninteracting systems, [96] the observed relative molecular level alignment between Ag and Au junctions for the three molecules studied here cannot be explained by simply considering the difference in the metal work function. There are several factors that alter the level alignment when a molecule is brought into contact with a metal: Charge screening by the metal brings the molecular orbitals closer to the Fermi level, [97] while charge transfer from/to the molecule and any dipole formed due the metal-molecule bond could alter alignment. [16], [17], [98], [99] Because of these local interactions, level alignment of a molecular system with different metals does not strictly follow the difference in the work functions. Our results further show that even the molecular backbone plays role in how the local interactions dictate the level alignment. We thus demonstrate that pyridine-linked molecules couple poorly to Ag electrodes compared to Au electrodes due to the reduced density of d-states, while the energy level alignment is dictated in part by the molecular backbone. These findings shed light onto the role of the electrode band structure and the local electrostatic effects in determining the charge transport properties of metal-molecule interfaces. A detailed

CHAPTER 2. EFFECT OF METALLIC BAND STRUCTURE ON CHARGE TRANSPORT THROUGH SINGLE-MOLECULE JUNCTIONS

study of the electrode band structure is therefore equally important as understanding the electronic structure of organic constituents for designing better metal-organic electronic devices.

2.7 Methods

2.7.1 AC Measurement Technique

We apply an AC voltage in addition to a DC voltage across the molecular junction and measure the currents over a bandwidth that goes beyond twice the AC frequency. The currents at the first and the second harmonic frequencies can be analyzed by looking at the Taylor series expansion of the junction current at V_{DC}

$$I(t) = \left(I(V_{DC}) + \frac{V_{AC}^2}{4} \frac{d^2I}{dV^2} \Big|_{V=V_{DC}} + \frac{V_{AC}^4}{64} \frac{d^4I}{dV^4} \Big|_{V=V_{DC}} \right) \\ + \text{Sin}(\omega_{AC}t) \left(\frac{dI}{dV} \Big|_{V=V_{DC}} V_{AC} + \frac{V_{AC}^3}{8} \frac{d^3I}{dV^3} \Big|_{V_o} \right) \\ - \text{Cos}(2\omega_{AC}t) \left(\frac{V_{AC}^2}{4} \frac{d^2I}{dV^2} \Big|_{V=V_{DC}} + \frac{V_{AC}^4}{48} \frac{d^4I}{dV^4} \Big|_{V=V_{DC}} \right) + \text{higher harmonics} \quad (2.2)$$

Here, I is the current through the junction, V_{DC} is DC voltage, V_{AC} is the amplitude of the AC voltage, and ω_{AC} is the frequency of the AC voltage. The terms in the first parentheses correspond to the DC current, while the terms in the second and third parentheses represent the currents at the first and the second harmonic frequencies respectively. We obtain the analytic expressions for the terms in the second and the third parentheses in terms of E_{level} and Γ using the single-Lorentzian model. In this model, assuming that the voltage drop across the junction is symmetric and the coupling to the left and right

CHAPTER 2. EFFECT OF METALLIC BAND STRUCTURE ON CHARGE TRANSPORT THROUGH SINGLE-MOLECULE JUNCTIONS

electrodes is the same, the current through the junction can be written as

$$I(V) = \frac{G_0}{e} \int_{-\infty}^{\infty} dE \frac{\Gamma^2/4}{(E - E_{level})^2 + \Gamma^2/4} (f(E - eV/2) - f(E + eV/2)) \quad (2.3)$$

where E_{level} is the energy of the frontier molecular orbital relative to the metal Fermi level, Γ is the molecular orbital coupling strength, V is the bias voltage, $G_0 = 2e^2/h$ is the conductance quantum and $f(E)$ is the Fermi-Dirac distribution.

Since all energy scales are much higher than the average thermal energy (25 meV), we can neglect the finite temperature effects as justified in Section 2.8.4, and can therefore simplify the expression for the junction current to yield

$$I(V) = \frac{1}{2e} G_0 \Gamma \tan^{-1} \left(\frac{eV - 2E_{level}}{\Gamma} \right) + \frac{1}{2e} G_0 \Gamma \tan^{-1} \left(\frac{eV + 2E_{level}}{\Gamma} \right) \quad (2.4)$$

By differentiating Eq. 2.4 with respect to the voltage, one can obtain the terms in the Taylor series expansion of the junction current as a function of E_{level} and Γ as shown explicitly in Section 2.8.3. With these expressions, we solve a set of two nonlinear equations with two unknowns using the currents at the first and the second harmonic frequencies to get the E_{level} and Γ values.

2.7.2 Theoretical Methods

Our first-principles calculations of the electronic transmission are based on a finite cluster approach that uses the PBE generalized gradient-corrected exchange-correlation functional, [100] as implemented in the FHI-AIMS code. [101] The junction contacts are modeled with two Au or Ag pyramids containing 31 atoms each cut from a face-centered lattice (lattice parameter 2.9387 Å for Au and 2.9331 Å for Ag). The junction axis is

CHAPTER 2. EFFECT OF METALLIC BAND STRUCTURE ON CHARGE TRANSPORT THROUGH SINGLE-MOLECULE JUNCTIONS

along the crystalline (100) direction. The molecules are bound to the apex atoms on each pyramid as shown in Figure 2.4A-C, modeling a vertical geometry, which allows for a direct comparison of the three systems. Furthermore, identical junction structures are used here with different metals to focus on the effect of band structure on transport properties. The positions of H, C, and N atoms were optimized with a variant of the Broyden-Fletcher-Shanno-Goldfarb algorithm [101], until the forces dropped below 0.01 eV/Å. The electron transmission through the junction was calculated with a Green's function approach applied to the composite electrode-molecule system and a simplified embedding self-energy. [102], [103]

2.8 Supporting Information

2.8.1 Experimental Set-up and Measurement Details

The block diagram of the experimental set-up is shown in Figure 2.6A. A voltage is applied to the junction using a digital to analog converter (NI PXI-4461), while the current through the junction is converted to voltage using a transimpedance amplifier (Femto DLPCA-200) with bandwidth 200 kHz. The voltage output of the transimpedance amplifier is recorded at 100 kHz using A/D inputs on the NI PXI-4461.

CHAPTER 2. EFFECT OF METALLIC BAND STRUCTURE ON CHARGE TRANSPORT THROUGH SINGLE-MOLECULE JUNCTIONS

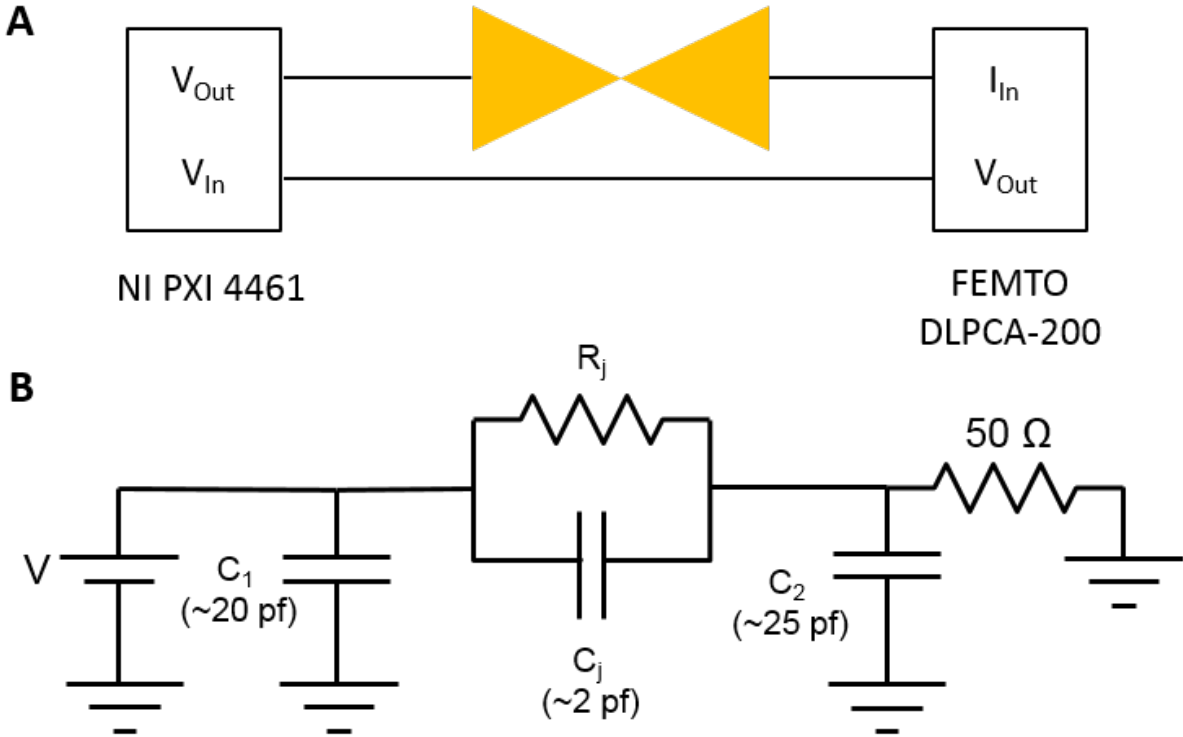


Figure 2.6: (A) Block diagram of STM-BJ set-up. (B) Details of the circuit showing all resistances and capacitances.

Figure 2.6B shows the circuit diagram: C_1 , C_2 are the cable capacitances, C_j denotes the junction capacitance. The transimpedance amplifier has a 50Ω input impedance. Since any current that passes through C_1 does not go through the junction, C_1 does not affect the measured current. C_2 is in parallel with the transimpedance amplifier. At 50 kHz, the impedance of C_2 is $1.3 \times 10^5 \Omega$ which is not comparable to 50Ω input impedance of the amplifier thus C_2 does not affect the measurement. C_j gives rise to capacitive currents. Therefore, the tunneling current is extracted by considering only the component of the measured current that is in-phase with the applied voltage.

CHAPTER 2. EFFECT OF METALLIC BAND STRUCTURE ON CHARGE TRANSPORT THROUGH SINGLE-MOLECULE JUNCTIONS

2.8.2 Two-dimensional Conductance versus Displacement

Histograms

In Figure 2.7, we show two-dimensional conductance versus displacement histograms for all the molecular systems studied. We observe a clear molecular feature indicative of junction formation and rupture. We note that the molecular feature extends to longer lengths with Ag electrodes when compared to Au electrodes, as has been observed and explained previously. [17]

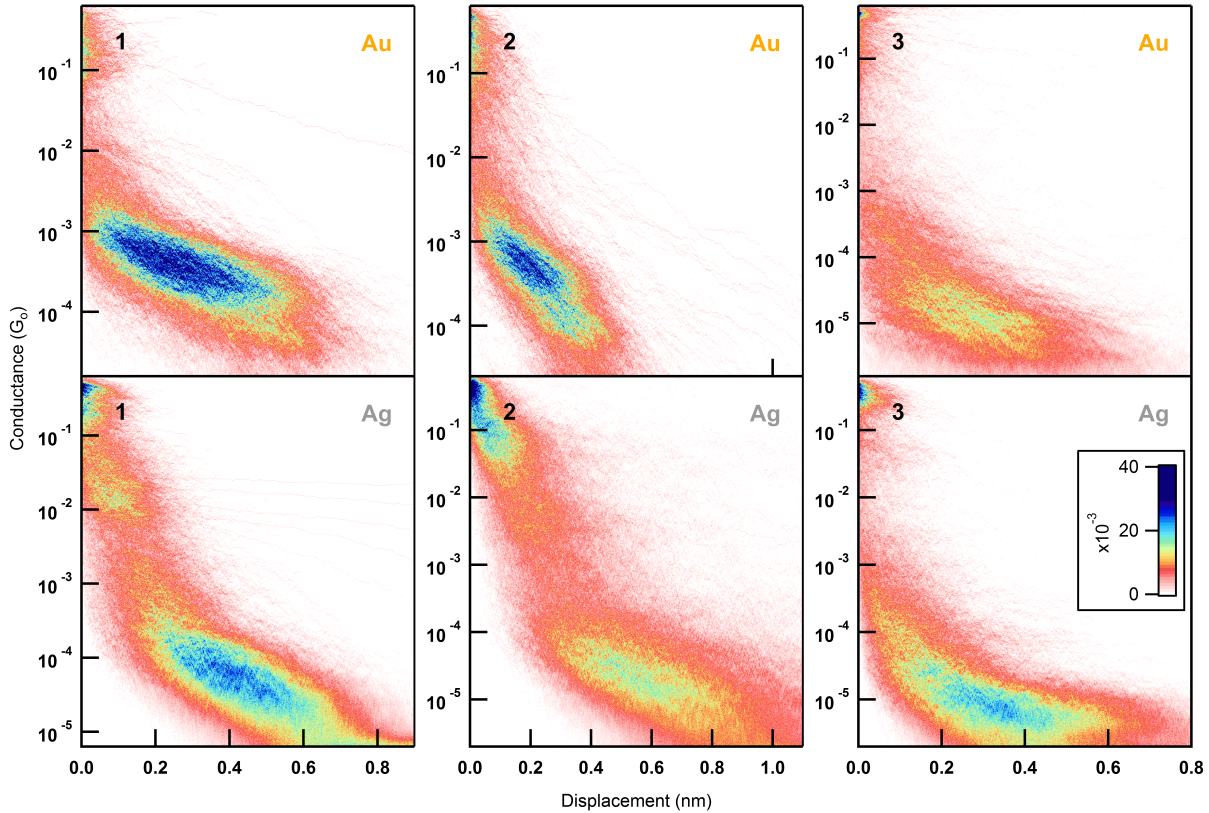


Figure 2.7: Normalized two-dimensional conductance-displacement histograms for measurements with Au (upper panel) and Ag (lower panel) electrodes using molecules 1, 2 and 3.

CHAPTER 2. EFFECT OF METALLIC BAND STRUCTURE ON CHARGE TRANSPORT THROUGH SINGLE-MOLECULE JUNCTIONS

2.8.3 Derivation of Model Equations

Taylor expansion of $I(V)$ at V_o is given as

$$\begin{aligned} I(V) &= I(V_o) + \frac{dI}{dV}\Big|_{V=V_o} (V - V_o) + \frac{1}{2} \frac{d^2I}{dV^2}\Big|_{V=V_o} (V - V_o)^2 \\ &\quad + \frac{1}{6} \frac{d^3I}{dV^3}\Big|_{V_o} (V - V_o)^3 + \frac{1}{24} \frac{d^4I}{dV^4}\Big|_{V=V_o} (V - V_o)^4 \\ &\quad + \frac{1}{120} \frac{d^5I}{dV^5}\Big|_{V=V_o} (V - V_o)^5 + \frac{1}{720} \frac{d^6I}{dV^6}\Big|_{V=V_o} (V - V_o)^6 + \dots \end{aligned} \quad (2.5)$$

Using $V = V_{DC} + V_{AC} \sin \omega_{AC} t$ and $V_o = V_{DC}$, we obtain

$$\begin{aligned} I(t) &= I(V_{DC}) + \frac{dI}{dV}\Big|_{V=V_{DC}} V_{AC} \sin \omega_{AC} t + \frac{1}{2} \frac{d^2I}{dV^2}\Big|_{V=V_{DC}} (V_{AC} \sin \omega_{AC} t)^2 \\ &\quad + \frac{1}{6} \frac{d^3I}{dV^3}\Big|_{V_o} (V_{AC} \sin \omega_{AC} t)^3 + \frac{1}{24} \frac{d^4I}{dV^4}\Big|_{V=V_{DC}} (V_{AC} \sin \omega_{AC} t)^4 \\ &\quad + \frac{1}{120} \frac{d^5I}{dV^5}\Big|_{V=V_{DC}} (V_{AC} \sin \omega_{AC} t)^5 + \frac{1}{720} \frac{d^6I}{dV^6}\Big|_{V=V_{DC}} (V_{AC} \sin \omega_{AC} t)^6 + \dots \end{aligned} \quad (2.6)$$

where V_{DC} is the DC voltage, V_{AC} is the AC voltage with angular frequency ω_{AC} . Using

CHAPTER 2. EFFECT OF METALLIC BAND STRUCTURE ON CHARGE TRANSPORT THROUGH SINGLE-MOLECULE JUNCTIONS

the Fourier series expansion including terms up to the sixth order, we find

$$\begin{aligned}
I(t) = & I(V_{DC}) + \frac{V_{AC}^2}{4} \frac{d^2 I}{dV^2} \Big|_{V=V_{DC}} + \frac{V_{AC}^4}{64} \frac{d^4 I}{dV^4} \Big|_{V=V_{DC}} + \frac{V_{AC}^6}{2304} \frac{d^6 I}{dV^6} \Big|_{V=V_{DC}} \\
& + \text{Sin}(\omega_{AC}t) \left(\frac{dI}{dV} \Big|_{V=V_{DC}} V_{AC} + \frac{V_{AC}^3}{8} \frac{d^3 I}{dV^3} \Big|_{V_o} + \frac{V_{AC}^5}{192} \frac{d^5 I}{dV^5} \Big|_{V=V_{DC}} \right) \\
& - \text{Cos}(2\omega_{AC}t) \left(\frac{V_{AC}^2}{4} \frac{d^2 I}{dV^2} \Big|_{V=V_{DC}} + \frac{V_{AC}^4}{48} \frac{d^4 I}{dV^4} \Big|_{V=V_{DC}} + \frac{V_{AC}^6}{1536} \frac{d^6 I}{dV^6} \Big|_{V=V_{DC}} \right) \\
& - \text{Sin}(3\omega_{AC}t) \left(\frac{V_{AC}^3}{24} \frac{d^3 I}{dV^3} \Big|_{V_o} + \frac{V_{AC}^5}{384} \frac{d^5 I}{dV^5} \Big|_{V=V_{DC}} \right) \\
& + \text{Cos}(4\omega_{AC}t) \left(\frac{V_{AC}^4}{192} \frac{d^4 I}{dV^4} \Big|_{V=V_{DC}} + \frac{V_{AC}^6}{3840} \frac{d^6 I}{dV^6} \Big|_{V=V_{DC}} \right) \\
& + \text{Sin}(5\omega_{AC}t) \frac{V_{AC}^5}{1920} \frac{d^5 I}{dV^5} \Big|_{V=V_{DC}} \\
& - \text{Cos}(6\omega_{AC}t) \frac{V_{AC}^6}{23040} \frac{d^6 I}{dV^6} \Big|_{V=V_{DC}}
\end{aligned} \tag{2.7}$$

When the transmission function takes a Lorentzian form, and when the applied bias voltage drops symmetrically across the junction, the relation between current and voltage in the zero-temperature limit becomes

$$I(V) = \frac{G_0}{e} \int_{-eV/2}^{eV/2} \frac{\Gamma^2/4}{(E - E_{level})^2 + \Gamma^2/4} dE \tag{2.8}$$

where E_{level} is the energy of the frontier molecular orbital relative to the metal Fermi level, Γ is the molecular orbital coupling strength, V is the bias voltage, $G_0 = 2e^2/h$ is the conductance quantum.

Upon integration, one obtains

$$I(V) = \frac{1}{2e} G_0 \Gamma \tan^{-1} \left(\frac{eV - 2E_{level}}{\Gamma} \right) + \frac{1}{2e} G_0 \Gamma \tan^{-1} \left(\frac{eV + 2E_{level}}{\Gamma} \right) \tag{2.9}$$

CHAPTER 2. EFFECT OF METALLIC BAND STRUCTURE ON CHARGE TRANSPORT THROUGH SINGLE-MOLECULE JUNCTIONS

The first six derivatives of $I(V)$ with respect to V are:

$$\frac{dI}{dV} = \frac{G_0}{2e} \frac{1}{\left(\frac{4(\frac{eV}{2} - E_{level})^2}{\Gamma^2} + 1 \right)} + \frac{G_0}{2e} \frac{1}{\left(\frac{4(\frac{eV}{2} + E_{level})^2}{\Gamma^2} + 1 \right)} \quad (2.10)$$

$$\frac{d^2I}{dV^2} = -\frac{2G_0}{e\Gamma^2} \frac{\left(\frac{eV}{2} + E_{level}\right)}{\left(\frac{4(\frac{eV}{2} + E_{level})^2}{\Gamma^2} + 1\right)^2} - \frac{2G_0}{e\Gamma^2} \frac{\left(\frac{eV}{2} - E_{level}\right)}{\left(\frac{4(\frac{eV}{2} - E_{level})^2}{\Gamma^2} + 1\right)^2} \quad (2.11)$$

$$\begin{aligned} \frac{d^3I}{dV^3} = & -\frac{G_0}{e\Gamma^2 \left(\frac{4(\frac{eV}{2} + E_{level})^2}{\Gamma^2} + 1 \right)^2} - \frac{G_0}{e\Gamma^2 \left(\frac{4(\frac{eV}{2} - E_{level})^2}{\Gamma^2} + 1 \right)^2} \\ & + \frac{16G_0 \left(\frac{eV}{2} - E_{level}\right)^2}{e\Gamma^4 \left(\frac{4(\frac{eV}{2} - E_{level})^2}{\Gamma^2} + 1\right)^3} + \frac{16G_0 \left(\frac{eV}{2} + E_{level}\right)^2}{e\Gamma^4 \left(\frac{4(\frac{eV}{2} + E_{level})^2}{\Gamma^2} + 1\right)^3} \end{aligned} \quad (2.12)$$

$$\begin{aligned} \frac{d^4I}{dV^4} = & -\frac{192G_0 \left(\frac{eV}{2} - E_{level}\right)^3}{e\Gamma^6 \left(\frac{4(\frac{eV}{2} - E_{level})^2}{\Gamma^2} + 1\right)^4} - \frac{192G_0 \left(\frac{eV}{2} + E_{level}\right)^3}{e\Gamma^6 \left(\frac{4(\frac{eV}{2} + E_{level})^2}{\Gamma^2} + 1\right)^4} \\ & + \frac{24G_0 \left(\frac{eV}{2} - E_{level}\right)}{e\Gamma^4 \left(\frac{4(\frac{eV}{2} - E_{level})^2}{\Gamma^2} + 1\right)^3} + \frac{24G_0 \left(\frac{eV}{2} + E_{level}\right)}{e\Gamma^4 \left(\frac{4(\frac{eV}{2} + E_{level})^2}{\Gamma^2} + 1\right)^3} \end{aligned} \quad (2.13)$$

$$\begin{aligned} \frac{d^5I}{dV^5} = & \frac{3072G_0 \left(\frac{eV}{2} - E_{level}\right)^4}{e\Gamma^8 \left(\frac{4(\frac{eV}{2} - E_{level})^2}{\Gamma^2} + 1\right)^5} + \frac{3072G_0 \left(\frac{eV}{2} + E_{level}\right)^4}{e\Gamma^8 \left(\frac{4(\frac{eV}{2} + E_{level})^2}{\Gamma^2} + 1\right)^5} \\ & - \frac{576G_0 \left(\frac{eV}{2} - E_{level}\right)^2}{e\Gamma^6 \left(\frac{4(\frac{eV}{2} - E_{level})^2}{\Gamma^2} + 1\right)^4} - \frac{576G_0 \left(\frac{eV}{2} + E_{level}\right)^2}{e\Gamma^6 \left(\frac{4(\frac{eV}{2} + E_{level})^2}{\Gamma^2} + 1\right)^4} \\ & + \frac{12G_0}{e\Gamma^4 \left(\frac{4(\frac{eV}{2} - E_{level})^2}{\Gamma^2} + 1\right)^3} + \frac{12G_0}{e\Gamma^4 \left(\frac{4(\frac{eV}{2} + E_{level})^2}{\Gamma^2} + 1\right)^3} \end{aligned} \quad (2.14)$$

CHAPTER 2. EFFECT OF METALLIC BAND STRUCTURE ON CHARGE TRANSPORT THROUGH SINGLE-MOLECULE JUNCTIONS

$$\frac{d^6 I}{dV^6} = -\frac{61440G_0 \left(\frac{eV}{2} - E_{level}\right)^5}{e\Gamma^{10} \left(\frac{4\left(\frac{eV}{2} - E_{level}\right)^2}{\Gamma^2} + 1\right)^6} - \frac{61440G_0 \left(\frac{eV}{2} + E_{level}\right)^5}{e\Gamma^{10} \left(\frac{4\left(\frac{eV}{2} + E_{level}\right)^2}{\Gamma^2} + 1\right)^6} \\ + \frac{15360G_0 \left(\frac{eV}{2} - E_{level}\right)^3}{e\Gamma^8 \left(\frac{4\left(\frac{eV}{2} - E_{level}\right)^2}{\Gamma^2} + 1\right)^5} + \frac{15360G_0 \left(\frac{eV}{2} + E_{level}\right)^3}{e\Gamma^8 \left(\frac{4\left(\frac{eV}{2} + E_{level}\right)^2}{\Gamma^2} + 1\right)^5} \\ - \frac{720G_0 \left(\frac{eV}{2} - E_{level}\right)}{e\Gamma^6 \left(\frac{4\left(\frac{eV}{2} - E_{level}\right)^2}{\Gamma^2} + 1\right)^4} - \frac{720G_0 \left(\frac{eV}{2} + E_{level}\right)}{e\Gamma^6 \left(\frac{4\left(\frac{eV}{2} + E_{level}\right)^2}{\Gamma^2} + 1\right)^4} \quad (2.15)$$

2.8.4 Finite Temperature Effects

In deriving the model equations, we neglected the finite temperature effects since the voltages used in the experiments are much larger than the average thermal energy at room temperature. The current at 1 V bias voltage differs less than 1% for the investigated systems when the finite temperature effects are included. Specifically, if we consider a junction with a Lorentzian transmission with $E_{level} = 1.1$ eV and $\Gamma = 0.04$ eV (as determined for molecule **1**), we get a current of 32.56 nA at 300 K compared to a current of 32.27 nA at 0 K.

2.8.5 Impact of Bias Voltage on Level Alignment and Coupling in Au Junctions

To investigate the effect of bias voltage on transmission characteristics, we determine E_{level} and Γ at 0.5 V, 0.75 V and 1.0 V DC for **1** and **2** with Au electrodes. In Figure 2.8, we observe that for both systems, Γ 's are almost identical at all three voltages. This shows that: (a) the molecule is not strongly polarized as this would induce changes in Γ ; (b) molecular vibrations are not activated as this would lead to an increased dG/dV resulting in a change in Γ and (c) local heating, if at all present, does not alter the results. We also

CHAPTER 2. EFFECT OF METALLIC BAND STRUCTURE ON CHARGE TRANSPORT THROUGH SINGLE-MOLECULE JUNCTIONS

note that there is a slight shift ($\sim 0.1\text{V}$) in E_{level} with increasing bias voltage away from the Fermi level. This could stem from a capacitive coupling, i.e. due to the molecule getting charged as the bias is increased, resulting in a small shift of the resonance; a second order Stark effect or small deviations from the single-Lorentzian transmission. Regardless of the underlying reason, this shows that the high bias measurements probe the zero bias transmission characteristics with a slight overestimation in E_{level} . Furthermore, these measurements provide experimental justification for the single-Lorentzian approximation as probing the transmission at different voltages yield almost identical results. We note that the experimental reason for doing all measurements at 1 V is that the nonlinearities in conductance with respect to voltage in Ag junctions are too small to be measured at lower DC bias voltages in **1**; while in molecule **2**, even at 1 V, we cannot carry out these measurements.

CHAPTER 2. EFFECT OF METALLIC BAND STRUCTURE ON CHARGE TRANSPORT THROUGH SINGLE-MOLECULE JUNCTIONS

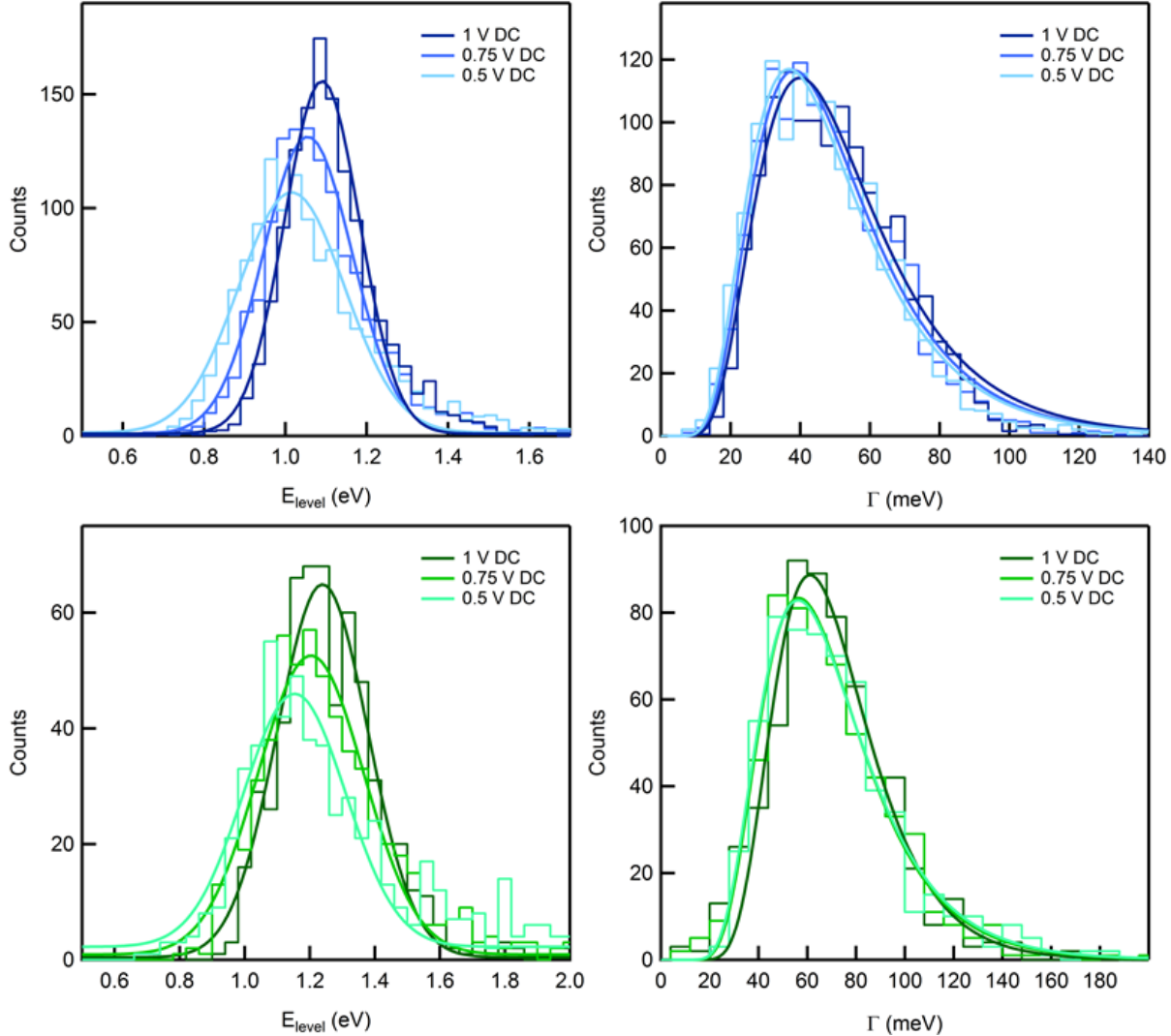


*Figure 2.8: Histograms of E_{level} and Γ for molecule **1** (top) and molecule **2** (bottom) with Au electrodes measured at different bias voltages.*

2.8.6 Comparison Between Experimental and Simulated IV's

To benchmark the experimental technique, we measure IV curves and also carry out the AC measurement for the same set of junctions with **1** and **2** using Au electrodes. This is done by holding a molecular junction, first measuring an IV curve and then applying

CHAPTER 2. EFFECT OF METALLIC BAND STRUCTURE ON CHARGE TRANSPORT THROUGH SINGLE-MOLECULE JUNCTIONS

an AC and DC voltage to determine E_{level} and Γ for the junction. We use the measured E_{level} and Γ to generate simulated IV curves using Eq. 2.9 above for each junction. In Figure 2.9, we compare the measured and simulated two-dimensional IV histograms. An averaged measured IV curve is overlaid on both measured and simulated two-dimensional IV histograms. We see an excellent agreement between the measured and simulated IV's in each system, demonstrating the strength of the new experimental technique we use here.

CHAPTER 2. EFFECT OF METALLIC BAND STRUCTURE ON CHARGE TRANSPORT THROUGH SINGLE-MOLECULE JUNCTIONS

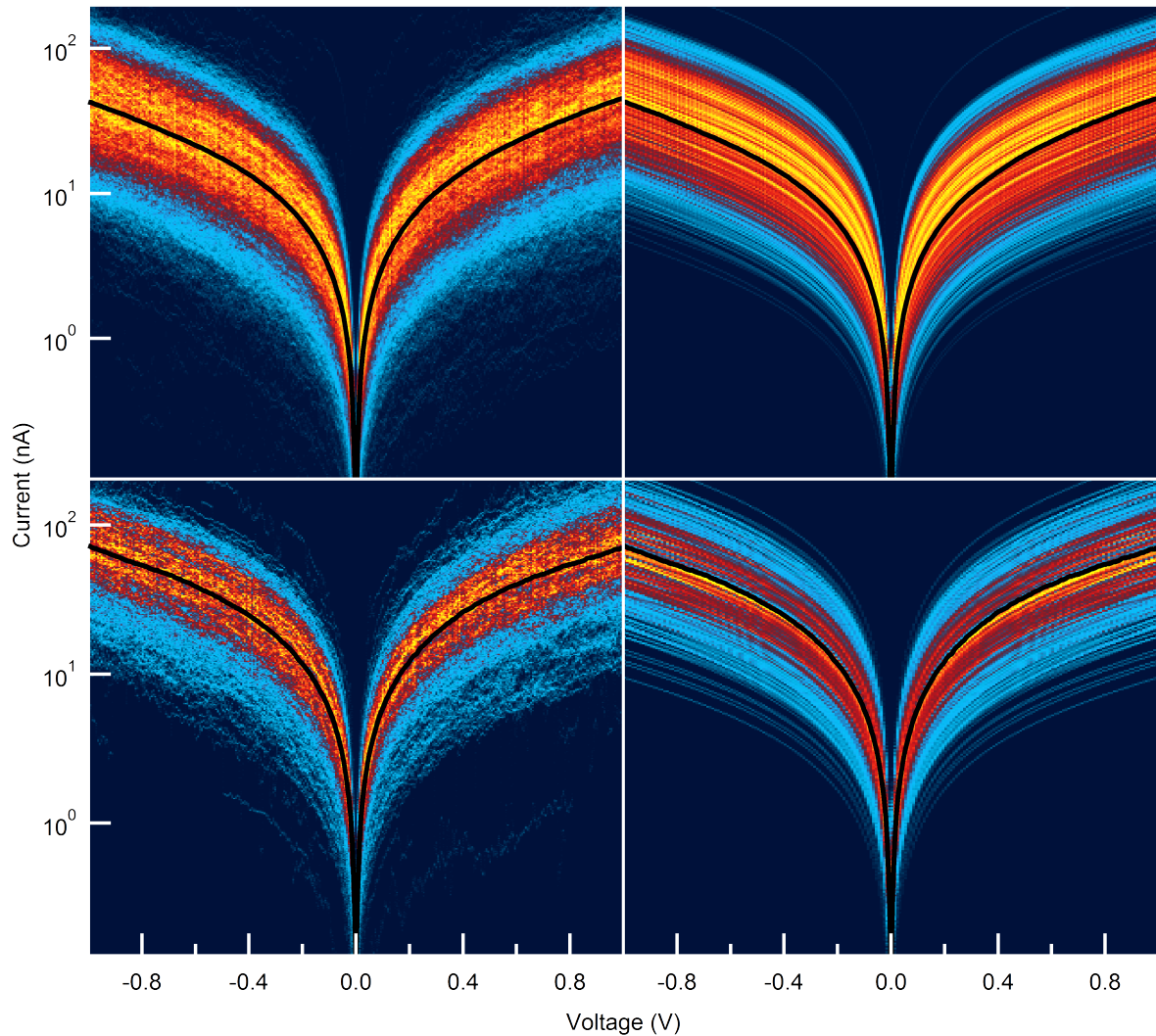


Figure 2.9: Experimental (left) and simulated (right) IV histograms for molecule 1 (top) and molecule 2 (bottom) with Au electrodes. Fits to the experimental IV's are overlaid onto the IV histograms for each molecule.

2.8.7 Impact of Asymmetric Coupling on the Experimental Technique

The experimental technique relies on the assumption that the couplings of a single-molecule junction to the electrodes are identical. Although the studied molecules have symmetric structures, they might still exhibit asymmetric couplings due to difference in binding geometries. Therefore, we need to examine the effect of asymmetric coupling on the experimental technique. For this purpose, we measured IV curves for **1** and **2** with Au electrodes. As shown in Figure 2.9, the IV histograms are very symmetric. However, if we look at individual IV's we see junctions exhibiting some asymmetry which gets averaged out in an IV histogram because the orientation of the molecule relative to the bias polarity is not controlled in our experiments. To overcome this issue, we obtain IV histograms by flipping the polarity of individual IV curves that show higher current at positive voltage. We see that IV histograms obtained by flipping procedure exhibit 30% more current at -1 V compared to 1 V (see Figure 2.10). This implies that the molecular orbital moves with the applied voltage, i.e. the bias voltage drops asymmetrically, resulting in rectification. One way to have asymmetric voltage drop is to have asymmetric couplings however, we point out that voltage induced time-dependent changes in the junction structure would also lead to asymmetric IV curves. In order to have 30% asymmetry in IV, a 6-8% asymmetry in the voltage drop is necessary for the molecular systems under study with the single-Lorentzian transmission with parameters reported in this work. If the entire asymmetry in voltage drop is due to asymmetry in coupling, couplings must differ by 30% according to Zotti, et.al. [83] The implications of these are two-fold: (a) the assumption of a transmission function with single coupling parameter does not hold and (b) the voltage drop is not symmetric. We examine the impact of these two findings separately.

CHAPTER 2. EFFECT OF METALLIC BAND STRUCTURE ON CHARGE TRANSPORT THROUGH SINGLE-MOLECULE JUNCTIONS

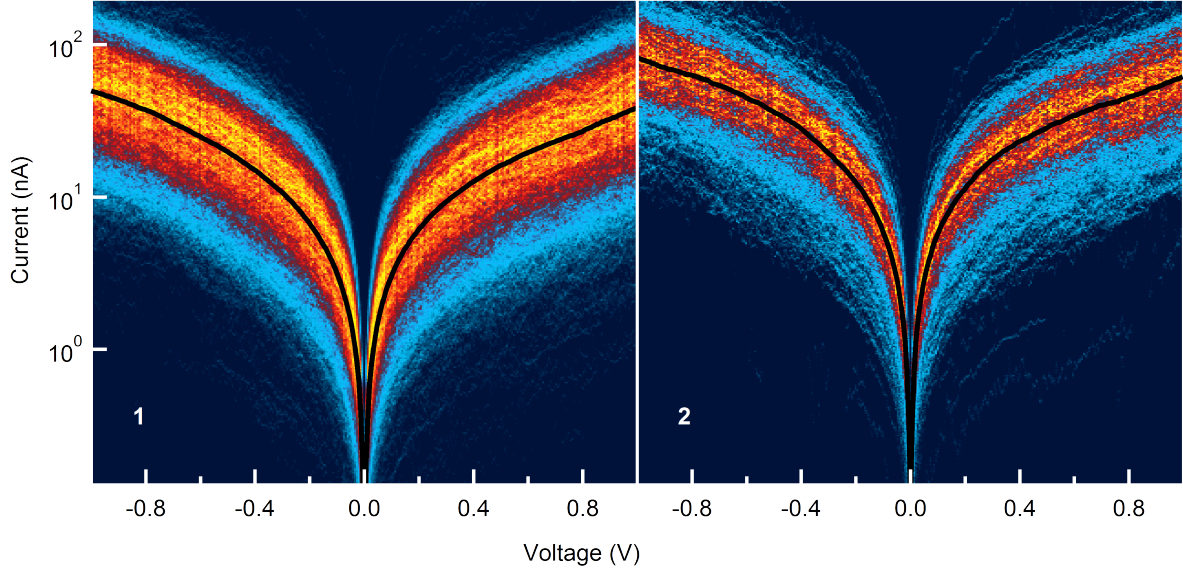


Figure 2.10: IV histograms for molecule 1 (left) and molecule 2 (right) with Au electrodes. Histograms are obtained by flipping the IV curves that show high current at positive polarity compared to negative polarity.

(a) The single-Lorentzian transmission with different couplings is modified to read

$$T(E) = \frac{\Gamma_L \Gamma_R}{(E - E_{level})^2 + (\Gamma_L + \Gamma_R)^2/4} \quad (2.16)$$

where $\Gamma = \Gamma_L + \Gamma_R$ following the standard convention.

In our system, $E - E_{level}$ is significantly larger than $(\Gamma_L + \Gamma_R)/2$ and thus at all biases used in our measurements, we have

$$T(E) = \frac{\Gamma_L \Gamma_R}{(E - E_{level})^2} \quad (2.17)$$

With this approximate transmission, in the presence of symmetric voltage drop, the experimental method measures twice the geometric mean of Γ_L and Γ_R instead of sum of

CHAPTER 2. EFFECT OF METALLIC BAND STRUCTURE ON CHARGE TRANSPORT THROUGH SINGLE-MOLECULE JUNCTIONS

two which leads to minor errors in the measured E_{level} and Γ .

(b) To investigate the impact of asymmetric voltage drop on the experimental method, we perform Monte Carlo simulations. We sample pairs of E_{level} and Γ from Gaussian distributions with mean values and distribution widths similar to the experimentally observed ones. We generate, for each E_{level} and Γ pair, two pairs of G and dG/dV using the single-Lorentzian transmission and assuming voltage drop with an asymmetry of +8% and -8% to account for two possible orientations of the molecule relative to the bias. Next, we apply our analysis method used for the experiments to determine E_{level} and Γ pairs for each true E_{level} and Γ pair using the generated G and dG/dV values. Note that our analysis method explicitly assumes that the voltage drop is symmetric. The results from the simulation are presented in Figure 2.11, where the estimated (red) and true (black) distributions of E_{level} and Γ are shown. We find that there is very little difference between the true distribution of Γ and the one obtained by assuming symmetric voltage drop in the presence of an 8% asymmetry. This indicates that asymmetry in the voltage drop required to get a 30% rectification does not lead to a significant error in Γ . The estimated distribution of E_{level} is however distinguishably different from the true one. Specifically, we find that estimated distribution is bimodal, while the true distribution is unimodal. However, since this is not what we see in the experiment (see Figure 2.3), we conclude that the actual asymmetry in voltage drop must be quite smaller than the one estimated from the asymmetric IV histograms. The observed asymmetry in the IV histograms is thus likely exaggerated by time-dependent changes in junction structure.

CHAPTER 2. EFFECT OF METALLIC BAND STRUCTURE ON CHARGE TRANSPORT THROUGH SINGLE-MOLECULE JUNCTIONS

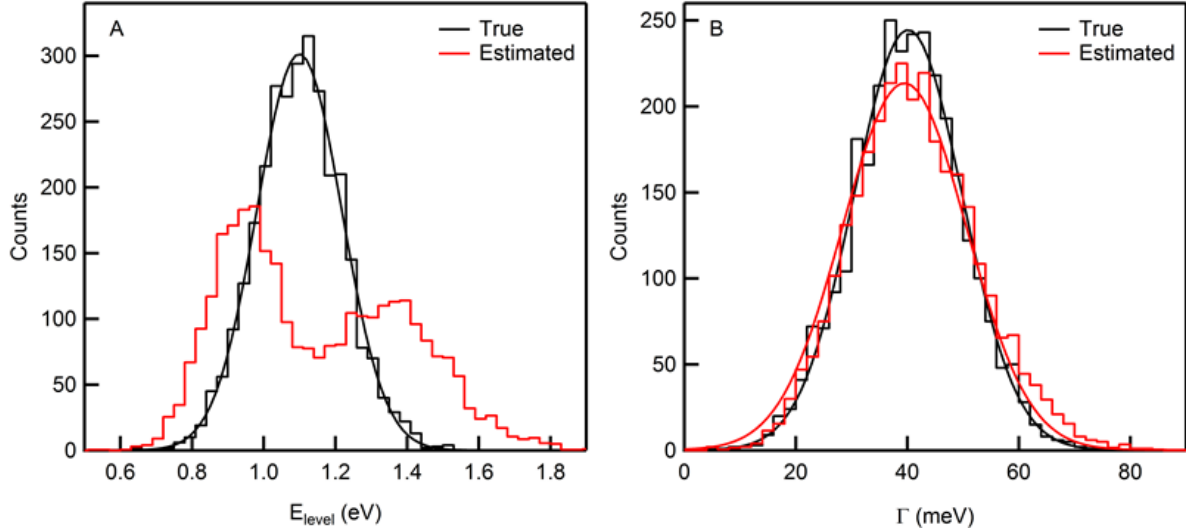


Figure 2.11: Monte Carlo simulations: True and estimated distributions of E_{level} (A) and Γ (B) when the voltage drop is asymmetric by 8% but is assumed to be symmetric.

2.8.8 Relativistic and non-Relativistic DFT Calculations

The DFT calculations are done using scalar relativistic corrections to the kinetic energy by pursuing the scaled zeroth order regular approximation. [104] Details of this implementation can be found in the work of Blum, et.al. [101] As shown in Figure 2.12, we find that without relativistic corrections, Γ is similar for both Ag and Au junctions for molecule 1. Specifically, we find that $\Gamma_{\text{Ag}} = 38$ meV and $\Gamma_{\text{Au}} = 52$ meV. With relativistic corrections, Γ_{Ag} increases by $\sim 10\%$ to 42 meV while Γ_{Au} increases by $\sim 50\%$ to 78 meV. As argued in the main text, this effect is related to the higher admixture of d-states of gold close to the Fermi level.

CHAPTER 2. EFFECT OF METALLIC BAND STRUCTURE ON CHARGE TRANSPORT THROUGH SINGLE-MOLECULE JUNCTIONS

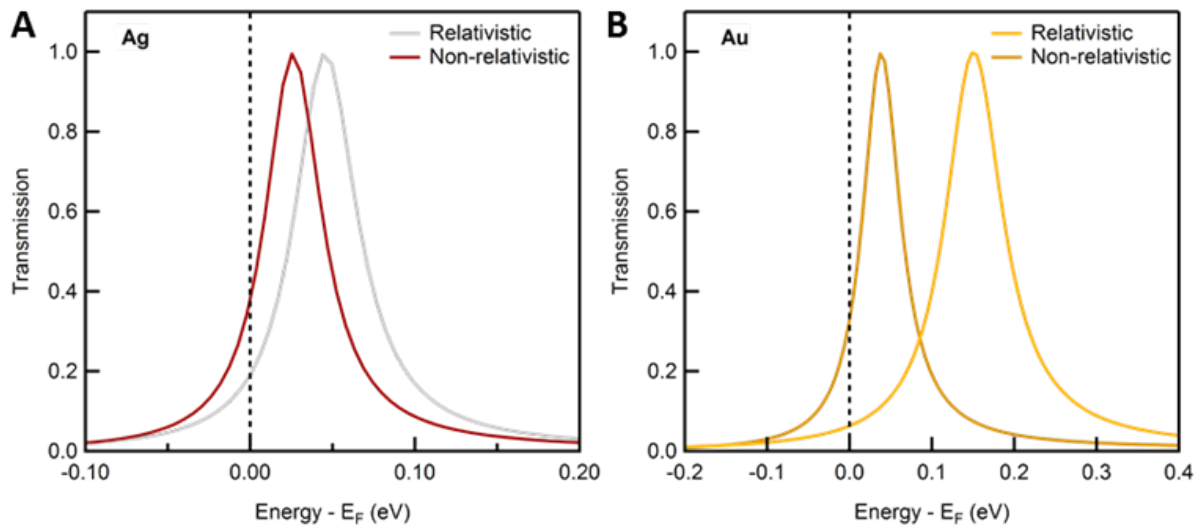


Figure 2.12: Calculated DFT-based transmission curves with and without relativistic corrections for molecular junctions of 1 formed with (A) Ag and (B) Au electrodes.

Chapter 3

Charge Transport at Hybrid Interfaces

3.1 Preface

This chapter is based on the manuscript entitled *Ultrafast Bidirectional Charge Transport and Electron Decoherence At Molecule/Surfaces Interfaces: A Comparison of Gold, Graphene and Graphene Nanoribbon Surfaces* by Olgun Adak, Gregor Kladnik, Gregor Bavdek, Albano Cossaro, Alberto Morgante, Dean Cvetko and Latha Venkataraman (submitted for publication). The work was conducted at the ALOISA Beamline at the Elettra Synchrotron in Trieste, Italy.

3.2 Abstract

We investigate bidirectional femtosecond charge transfer dynamics using the core-hole clock implementation of resonant photoemission spectroscopy from 4,4'-bipyridine molecular layers on three different surfaces: Au(111), epitaxial graphene and graphene nanoribbons. We show that the lowest unoccupied molecular orbital (LUMO) of the molecule drops partially below the Fermi level upon core-hole creation in all systems, opening an ad-

CHAPTER 3. CHARGE TRANSPORT AT HYBRID INTERFACES

ditional decay channel for the core-hole, involving electron donation from substrate to the molecule. Furthermore, using the core-hole clock method, we find that the bidirectional charge transfer time between the substrate and the molecule is fastest on Au(111), with a 2 fs time, then around 4 fs for epitaxial graphene and slowest with graphene nanoribbon surface, taking around 10 fs. Finally, we provide evidence for fast phase decoherence of the core-excited LUMO* electron through an interaction with the substrate providing the first observation of such a fast bidirectional charge transfer across an organic/graphene interface.

3.3 Introduction

Graphene and its derivatives have been subject to extensive research due to their extraordinary electronic, mechanical and optical properties.[105]–[114] Molecular electronics has also attracted attention from the physics and chemistry community for providing a fundamental understanding of charge transfer at the nanometer scale.[70], [71], [115], [116] Recently, efforts for incorporating carbon-based components into organic electronic devices have been fruitful; for example, researchers have demonstrated that hybrid devices can function as solar cells and light emitting diodes. [112], [117]–[120] Clearly, the performance and quality of such devices depends strongly on the electronic properties of their hybrid interfaces. Therefore, a complete understanding of charge transfer dynamics at such interfaces is fundamental for designing functional and efficient carbon-based organic electronic devices.

Here, we use a combination of X-ray-based spectroscopy techniques including X-ray photoemission spectroscopy (XPS), near-edge X-ray absorption fine-structure spectroscopy (NEXAFS) and resonant photoemission spectroscopy (RPES) with the core-hole clock method, as illustrated in see Figure 3.1A, to probe charge transfer dynamics across

CHAPTER 3. CHARGE TRANSPORT AT HYBRID INTERFACES

heterogeneous interfaces. [49], [52], [65], [66], [121]–[124] Core-hole clock spectroscopy has previously been used to measure femtosecond charge-transfer times across different molecule-metal interfaces. [49], [61]–[68], [125] We apply this technique to investigate femtosecond charge transfer dynamics from 4,4'-bipyridine (BP) molecular layers to Au(111), epitaxial graphene and graphene nanoribbon (GNR) surfaces (see Figure 3.1B). We find that charge transfer from BP to the carbon surfaces is slow when compared with the Au(111) surface. We attribute this difference to a reduced electronic interaction between the molecule and the carbon-based surfaces due to a reduced density of electronic states of the surface. We further observe that the creation of a core-hole on BP significantly alters the alignment of the BP molecular levels relative to the substrate Fermi level (E_F), bringing the LUMO in the presence of a core-hole (LUMO*) close to E_F . This leads to electron transfer between the LUMO* and the substrate continuum states within the core-hole lifetime. We can therefore probe the bidirectional charge transfer times and provide evidence for ultrafast phase decoherence of the photo-excited LUMO* electron through an interaction with the substrate. When the LUMO* remains above Fermi, the LUMO* electron can escape to the substrate as long as the LUMO orbital is coupled to the substrate. [62] However, in the systems studied here, the excited core electron remains partially on the LUMO* as a significant portion of the LUMO* drops below the Fermi level. The phase information of the core excited LUMO* electron is lost through the interaction with the substrate and thus the subsequent decay of the LUMO* electron is not degenerate with direct photoemission. The angle-dependent RPES measurements presented here provide, for the first time, direct evidence for this phase decoherence occurring on the femtosecond timescale due to the LUMO* coupling with the substrate states.

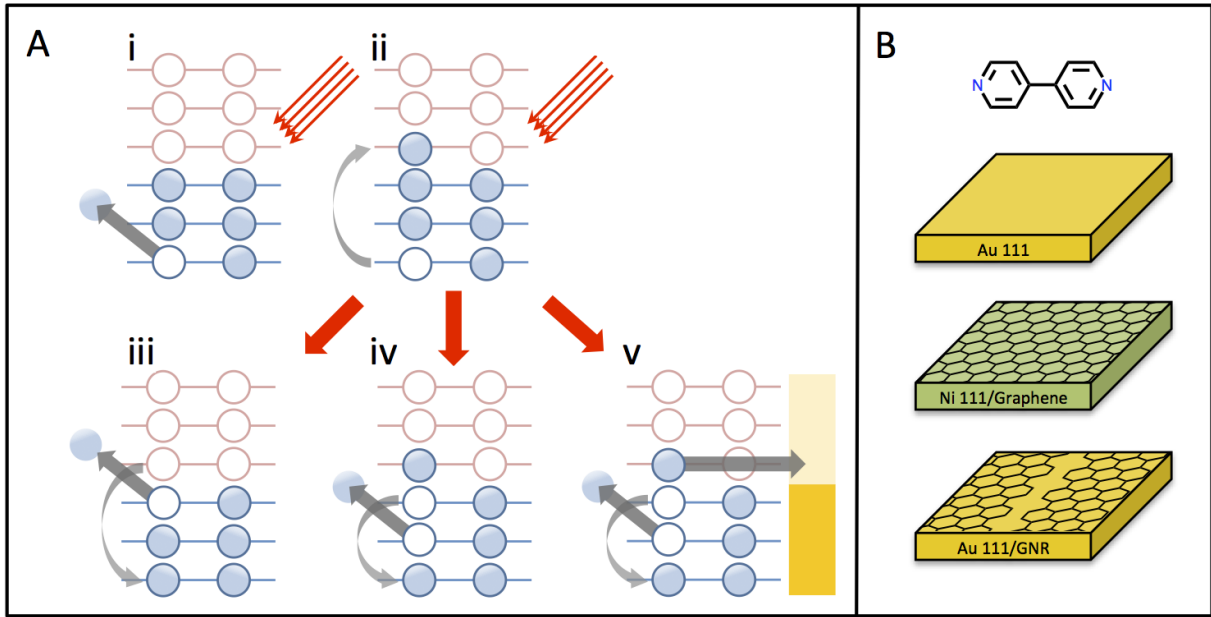


Figure 3.1: (A) Schematic representation of photoemission processes. *i.* Direct photoemission. *ii.* Core-hole/LUMO* electron pair generation. *iii.* Participator decay. *iv.* Spectator decay. *v.* charge transfer from the LUMO* to the substrate and Auger decay. (B) Structure of 4,4'-bipyridine and the three surfaces studied in this work.

3.4 Results and Discussion

We first present XPS spectra for monolayer films of BP on all three surfaces and for a multilayer film on Au(111) in Figure 3.2A, which allow us to compare the nitrogen 1s (N1s) electron binding energy across these systems. The surface preparation details are given the in Section 3.6.1. We observe that in all systems, the N1s electron binding energy is larger than that in the multilayer. We also see that the N1s binding energy varies with the substrate. It is smallest (398 eV) on Au(111) most likely due to the ability of the metal to effectively screen the core-hole. [126] The N1s binding energy is increased to 399 eV on the epitaxial graphene on Ni(111) surface, consistent with a decrease in

CHAPTER 3. CHARGE TRANSPORT AT HYBRID INTERFACES

free electron density of this surface. Finally, we observe that the N1s binding energy is closest to that of the multilayer for the GNR on Au(111) substrate. The first implication of this observation is that the GNR's cover the underlying Au substrate completely as the spectrum is comprised of a narrow single peak. Second, we can conclude that the density of electronic states for this surface is not sufficiently high to screen the core-hole as efficiently as Au, consistent with the fact that GNR presents a significant band gap; [127] the effective image plane is likely closer to the underlying Au surface, resulting in a smaller shift in the N1s binding energy.

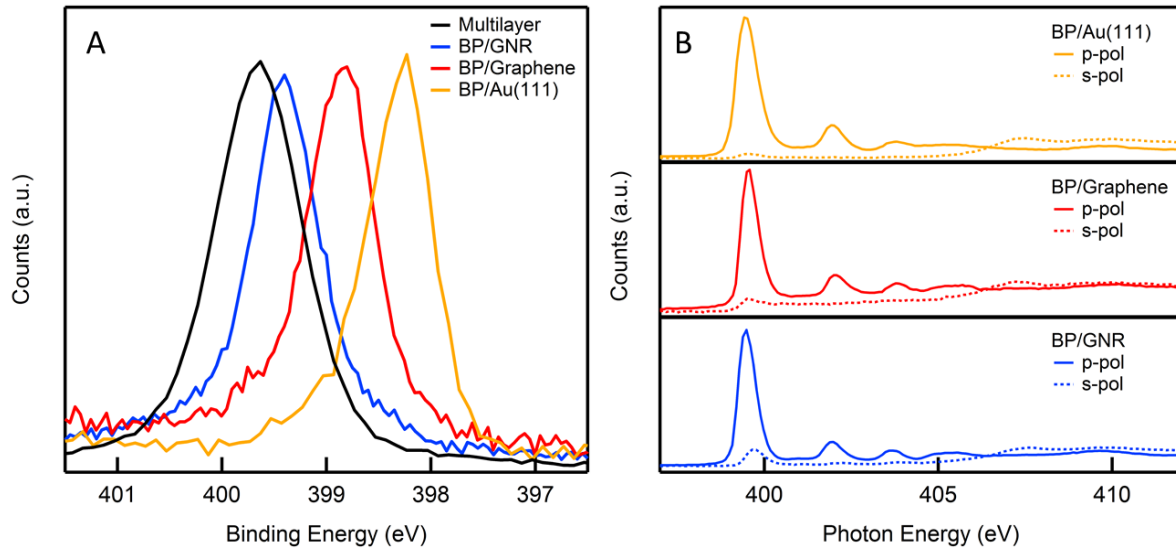


Figure 3.2: (A) N1s binding energies of BP monolayer on Au(111), epitaxial graphene, GNR and a multilayer BP film on Au(111). All measurements are carried out at a photon energy of 500 eV. (B) Nitrogen K-edge NEXAFS spectra of a BP monolayer on Au(111), epitaxial graphene and GNR measured with the incident electric field polarized perpendicular (p-pol) or parallel (s-pol) to the surfaces.

We determine the molecular orientation on these surfaces by exploiting the polarization dependence of the N1s to LUMO transition, which is subject to the dipole selection

CHAPTER 3. CHARGE TRANSPORT AT HYBRID INTERFACES

rules. [51] The LUMO of BP has π character with its nodal plane coinciding with the molecular aromatic ring. [60] The N1s to LUMO transition is therefore forbidden for light polarized in the plane of aromatic rings. We determine an average angle for BP by comparing the N1s to LUMO transition cross-section with incident electric field perpendicular (*p-pol*) and parallel (*s-pol*) to the surface. [51] In Figure 3.2B, we show a NEXAFS spectrum where we observe that the N1s to LUMO transition is strongly suppressed in *s-pol* on all surfaces. We find that the average angle is around 14° on Au(111), 20° on epitaxial graphene and 26° on GNR while the N1s to LUMO transition peak is broadest on Au(111) and narrowest on GNR. These two results together allow us to conclude that the molecule/surface interaction is strongest on Au(111) and weakest on the GNR surface.

We now turn to the measurements of charge transfer dynamics using the RPES technique. In this technique, a core electron is excited to an unoccupied molecular orbital, or even to the free electron continuum, leaving a core-hole on the molecule. This excited state decays via multiple processes, involving emission of photons or electrons. The former, photoluminescence, is not relevant to the RPES technique; while the latter, photoemission, is fundamental to RPES as illustrated in Figure 3.1A. The first process that involves electron emission proceeds with the filling of the core-hole and the subsequent emission of an electron, leaving the LUMO empty; this decay process is called participator decay. The second decay process results in the filling of the core-hole and the subsequent electron emission, leaving the system with two holes and an additional (spectator) electron in the LUMO; this decay process is called spectator decay. When the molecule is electronically coupled to the substrate, the excited electron can escape to the substrate, quenching the participator and spectator decay channels. By comparing the participator decay intensities in the isolated and coupled molecular systems and knowing the core-hole lifetime (5 fs for N1s) [128], we can determine the charge transfer times across the

CHAPTER 3. CHARGE TRANSPORT AT HYBRID INTERFACES

molecule-surface interfaces. [52] However, another core-hole decay scenario arises if the LUMO* drops below the Fermi level upon a core-hole creation. [61] In this case, the LUMO* may get filled via electron transfer from the substrate even if the electron is initially photoexcited to an orbital higher than the LUMO (LUMO+1, etc.). Thus, the characteristic spectral lines due to the decay of the LUMO* electron are observed regardless of the incident light energy; we denote this process as super-participant decay. As detailed in Section 3.6.4, by using the super-participant and participant intensities in the coupled system and the participant intensity in the isolated system, one can obtain the bidirectional charge transfer time and estimate the fraction of the LUMO* that falls below the Fermi level upon the creation of the core-hole.

We measure the RPES spectra, which are comprised of XPS measurements taken at a series of incident photon energies across the nitrogen K absorption edge, of BP multilayer on Au(111) and BP monolayer on the three surfaces considered here. The multilayer film serves as a reference for the uncoupled or the isolated system and is used to obtain the charge transfer times for all monolayer films. Figure 3.3A shows a two-dimensional photon energy versus electron kinetic energy RPES map for a BP monolayer film on Au(111). We note first that the resonance intensity due to an excitation to the LUMO* at a photon energy of 399 eV is visible in the map. More importantly, we see a clear spectroscopic feature near an electron kinetic energy of 394 eV, which corresponds to the decay of the LUMO* electron independent of the photon energy above 405 eV. This is the signature for the super-participant decay process.

CHAPTER 3. CHARGE TRANSPORT AT HYBRID INTERFACES

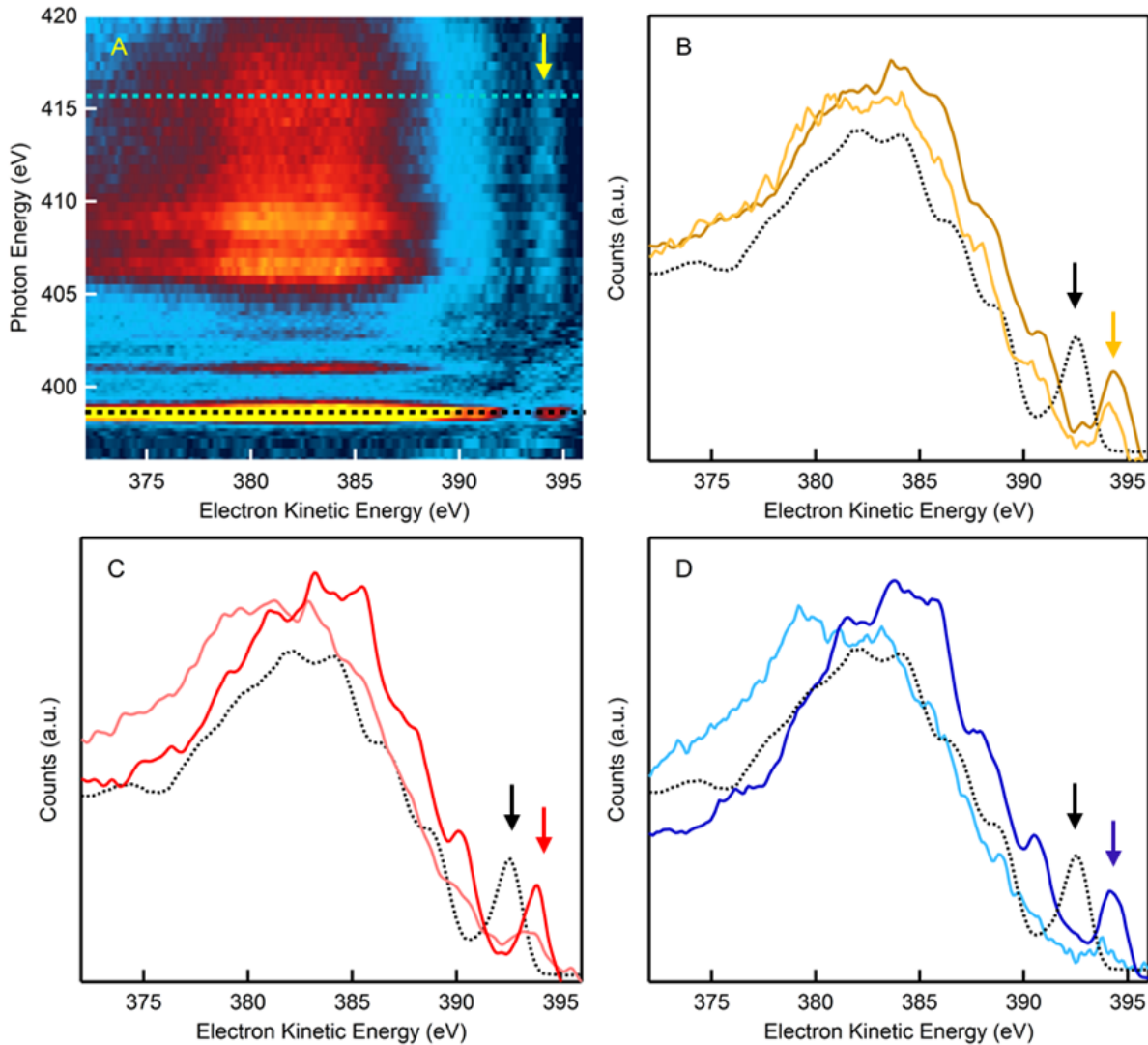


Figure 3.3: (A) Nitrogen K-edge RPES map of BP monolayer on Au(111) showing the LUMO* resonance (black dashed line), a line scan above the ionization edge (blue dashed line) and the super-participant decay seen as a vertical feature starting at the LUMO* energy as indicated by yellow arrow. Nitrogen K-edge RPES line scans at the LUMO* (dark), above the ionization edge (light), and multilayer LUMO* (dashed black) for a BP monolayer on (B) Au, (C) epitaxial graphene and (D) GNR. Arrows indicate the participant and super-participant peaks.

CHAPTER 3. CHARGE TRANSPORT AT HYBRID INTERFACES

In Figure 3.3B-D, we present RPES line scans at LUMO* and above the ionization edge for all three monolayers (at energies indicated by the dashed lines in Figure 3.3A) and compare these to the line scan at the LUMO* of the multilayer system. First, we see that in all systems, the intensity of the participator decay is reduced relative to the multilayer indicating a charge transfer from the LUMO* to the substrate within the core-hole lifetime. Second, we observe that BP monolayer on all surfaces exhibits HOMO-LUMO* super-participator Auger lines once a core-hole is created regardless of the photon energy. This indicates that the LUMO* drops at least partially below the Fermi level once the N1s core-hole is created, leading to a charge transfer from the substrate to the LUMO* and followed by the super-participator and spectator decay processes. [61] Next, we obtain the bidirectional charge transfer times and estimate the fraction of the LUMO* that falls below the Fermi, as described in Section 3.6.4. We obtain the bidirectional charge transfer times as 2 fs for Au(111), 4 fs for epitaxial graphene and 10 fs for GNR, while the fractions of the LUMO* that fall below the Fermi level are around 1/5 for both Au(111) and epitaxial graphene. For the GNR surface, where Fermi is likely to fall within the band gap [127], we do not observe a measurable back-filling of the LUMO*, similar to what has been observed on semiconducting surfaces. [129] We note that the observed charge transfer times are consistent with the trends in the spectator shifts in the Auger spectra on the LUMO* as seen In Figure 3.3B-D. [68]

The strong modification to the level alignment induced by the core-hole not only lets us observe bidirectional charge transport in the RPES measurements, it also opens up the possibility of observing electron decoherence via an interaction with the substrate. The participator decay process is a resonant photoemission process, degenerate with the direct photoemission with an identical final state having a single hole in the valence band. This process is subject to the dipole selection rules. [51] Specifically, the angle between the

CHAPTER 3. CHARGE TRANSPORT AT HYBRID INTERFACES

light polarization and the normal of the HOMO nodal plane dictates the photoemission intensity. However, if the LUMO* electron interacts with the substrate before filling the core-hole, it loses the phase information. Therefore, any subsequent decay would be of an Auger type with almost no angular dependence on the light polarization. [130], [131] The intensity of the emitted electrons will therefore show only a weak or no dependence on the light polarization as long as the charge transfer time is significantly shorter than the core-hole life-time.

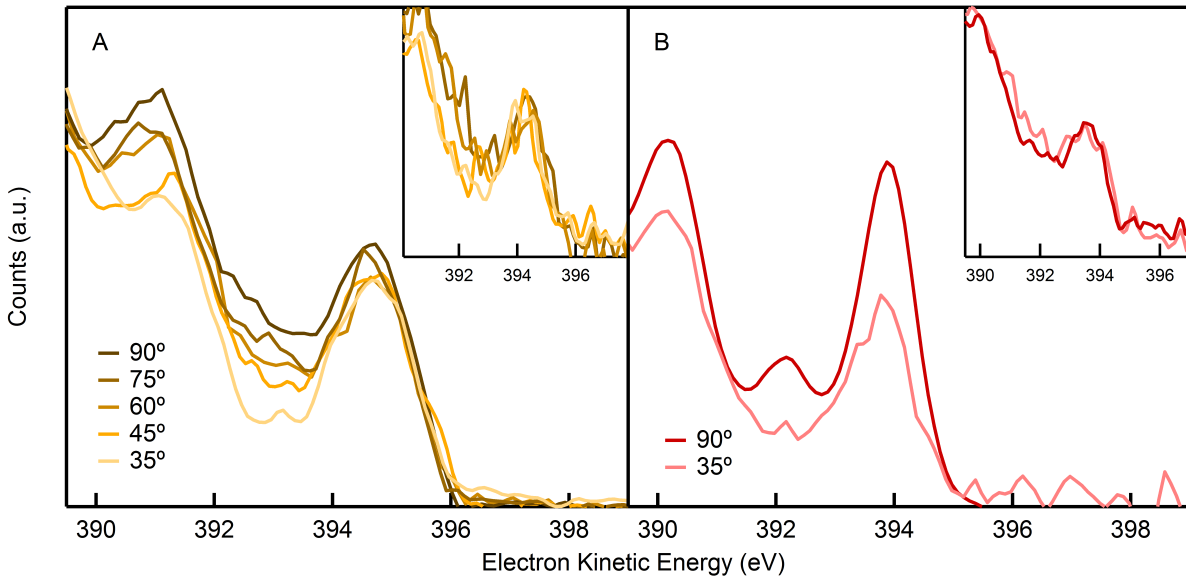


Figure 3.4: Nitrogen K-edge RPES line scans at the LUMO energy showing the participant intensity for (A) BP on Au(111) at polarization angles of 90°, 75°, 60°, 45°, 35° and (B) BP on epitaxial graphene at polarization angles of 90° and 35°. Inset: Nitrogen K-edge RPES line scans taken at 416 eV showing the super-participant peaks.*

To probe the phase decoherence of the LUMO* electron through an interaction with the substrate, we measure the nitrogen K-edge RPES spectra for the BP monolayer on Au(111) at five different polarization angles relative to the surface, ranging from 35° to 90°. In Figure 3.4A, we show the participant intensity at the LUMO* excitation for all

CHAPTER 3. CHARGE TRANSPORT AT HYBRID INTERFACES

polarization angles measured, where we see a weak dependence on the polarization angle. This demonstrates that most of the participator decay occurs after the electron loses its phase information through an interaction with the substrate, consistent with the very fast charge transfer observed in this system. In Figure 3.4B, we show similar measurements at two angles for the BP monolayer film on epitaxial graphene. The intensity of the emitted electron shows a 30% decrease when the angle between the light polarization and the surface goes from 90° to 35°. This points to a significant resonant photoemission component in the total photoemission signal, consistent with the charge transfer time comparable to the core-hole lifetime determined above for this system. As a comparison, we also report the angular dependence of the super-participator decay intensity measured at a photon energy of 416 eV, which is entirely due to electron donation from the substrate to the LUMO* and as such bears no phase information with the core-electron excitation. In both the Au(111) and the graphene system, we see no angular dependence, consistent with an Auger type decay of the core-hole. [132] Therefore, the measurements presented here provide evidence for ultrafast phase decoherence of hot electrons on Au(111) and epitaxial graphene surfaces.

3.5 Conclusion

In conclusion, we have probed the interfacial charge transfer between a BP monolayer on Au(111), epitaxial graphene/Ni(111) and GNR/Au(111) surfaces. We find that the charge transfer is fastest on Au(111) which indicates a strong electronic interaction between BP and the surface. Charge transfer is slower on the epitaxial graphene surface where the BP/graphene interaction is primarily through a van der Waals coupling. Finally, we find an even slower charge transfer on the semiconducting GNR surface which could stem from the presence of a band gap in GNR. [127] Our experiments also show that the GNR layer

on Au serves to hinder charge transfer from the overlying BP molecules to the Au surface. Finally, our measurements provide direct evidence for ultrafast electron decoherence due to organic molecule - substrate coupling as evidenced by the modified angular dependence of the resonant photoemission intensity with the light polarization.

3.6 Supporting Information

3.6.1 Measurement Details and Sample Preparation

The experiments were conducted at the ALOISA beamline of the Elettra Synchrotron in Trieste. The measurement chamber was maintained at an ultrahigh-vacuum at pressures of 10^{-10} - 10^{-11} mbar. [123], [133], [134] The 4,4'-bipyridine (BP) molecules were purchased from Sigma-Aldrich (purity > 99%) and used without further purification. The molecules were placed in a Pyrex cell and connected to the pre-chamber through a leak valve.

The Au(111) surface was prepared by cycles of Ar+ sputtering and annealing at 400 K. X-ray photoemission spectroscopy (XPS) was used to check for any chemical impurities (O, N, and C). The BP cell was heated to several tens of degrees above room temperature and BP was leaked into a pre-chamber to maintain a partial BP pressure of 10^{-7} mbar for 4 - 5 minutes. The sample was cooled to -65° C for the multilayer phase, and it was kept at room temperature for the monolayer phase.

The epitaxial graphene on Ni(111) surface was prepared by repeatedly sputtering (Ar+, 2 keV) and annealing (900 K) the Ni(111) surface. XPS and Helium atom scattering were used to check for the presence of any chemical impurities and to probe the surface order. Epitaxial graphene was prepared via catalytic dissociation of ethylene on Ni(111) surface. An ethylene partial pressure of 10^{-6} mbar was maintained for 60 minutes while keeping the surface at 850 K. [135] The graphene film was probed using XPS and

CHAPTER 3. CHARGE TRANSPORT AT HYBRID INTERFACES

ultraviolet photoemission spectroscopy with He II line at 40.8 eV. Examination of the graphene π -band bottom, close to Γ , was used to identify the graphene layer as epitaxial graphene. The epitaxial graphene/Ni(111) sample was exposed to ambient conditions before being transferred to the ALOISA chamber. The sample was annealed in the ALOISA chamber at 500 K to recover the pristine graphene. XPS, valance band photoemission spectroscopy and near edge X-ray absorption fine structure (NEXAFS) spectroscopy measurements were further performed to characterize the epitaxial graphene/Ni(111) sample. To create the BP self-limiting monolayer film, a partial BP pressure of 10^{-7} mbar was maintained in the pre-chamber for 3 minutes, while the sample was cooled to -50° C.

Graphene nanoribbons (GNR) were formed depositing 10,10'-dibromo-9,9'-biantryl (AOKBIO, 98+% purity) on the cleaned Au(111) sample maintained at 200° C to ensure saturating the Au(111) surface with the GNR precursor. This surface was then annealed to 400° C to create GNR's as described previously.[136] XPS and NEXAFS measurements were performed to characterize the GNR film on the Au(111) surface. To create the BP monolayer film, a partial BP pressure of 10^{-7} mbar was maintained in the chamber for 5 minutes while the sample was cooled to -45° C.

3.6.2 X-Ray Photoemission Spectroscopy and Near Edge X-Ray Absorption Fine Structure Spectroscopy Measurements

X-ray photoemission spectroscopy (XPS) measurements were performed at the ALOISA beamline with the X-ray beam at grazing-incidence (4°) to the sample. Photoelectrons from the sample were collected at the normal to the surface using a hemispherical electron analyzer with an acceptance angle of 2° , and an overall energy resolution of ~ 0.2 eV. The energy scale for XPS spectra was calibrated by aligning the Au $4f_{7/2}$ peak to a binding energy of 84.0 eV for the Au(111) and GNR/Au(111) measurements. For the epitaxial

CHAPTER 3. CHARGE TRANSPORT AT HYBRID INTERFACES

graphene on Ni(111), XPS spectra were aligned to the Fermi level.

Near edge X-ray absorption fine structure (NEXAFS) measurements were performed on the nitrogen K-edge by sweeping the incident photon energy from 396 eV to 420 eV in steps of 0.1 eV. The photon incidence angle was set to 6°. Spectra were acquired using a channeltron detector with a wide acceptance angle in the partial electron yield mode and a high pass filter with cutoff energy set to 370 eV. The photon flux was monitored on the last optical element along the beam path. The sample normal was oriented either parallel (*p-pol*) or perpendicular (*s-pol*) to the light polarization.

3.6.3 RPES Measurement and Data

The RPES spectra at the nitrogen K-edge were obtained by taking XPS scans spanning 0-60 eV binding energy range with the photon energy tuned between 394 eV and 423 eV in steps of 0.2 eV and 0.5 eV for all surfaces studied. The RPES measurements for charge transfer time calculations were performed in magic angle conditions, with the light polarization and the electron analyzer at 54.7° with respect to the surface normal. This yields a RPES signal that is independent of the molecular orientation on the sample (see Section 3.6.4). For the angle-dependent RPES measurements, the angle between the photon polarization and surface normal set to the values stated in the main text while the electron analyzer was always collinear with the photon polarization. These RPES data were then normalized and analyzed following previously published procedures. [62], [63] Briefly, the photon flux on the last optical element along the beam path was measured; and used to normalize and calibrate the RPES scans for any fluctuations in photon intensity and energy. The energy scale for XPS spectrum was calibrated as detailed above. The non-resonant photoemission spectrum was obtained from the XPS scan at 395 eV and subtracted from the entire RPES spectra. The RPES line scans were then further

CHAPTER 3. CHARGE TRANSPORT AT HYBRID INTERFACES

normalized by the overall Auger intensity which scales with the absorption cross-section at a given photon energy.

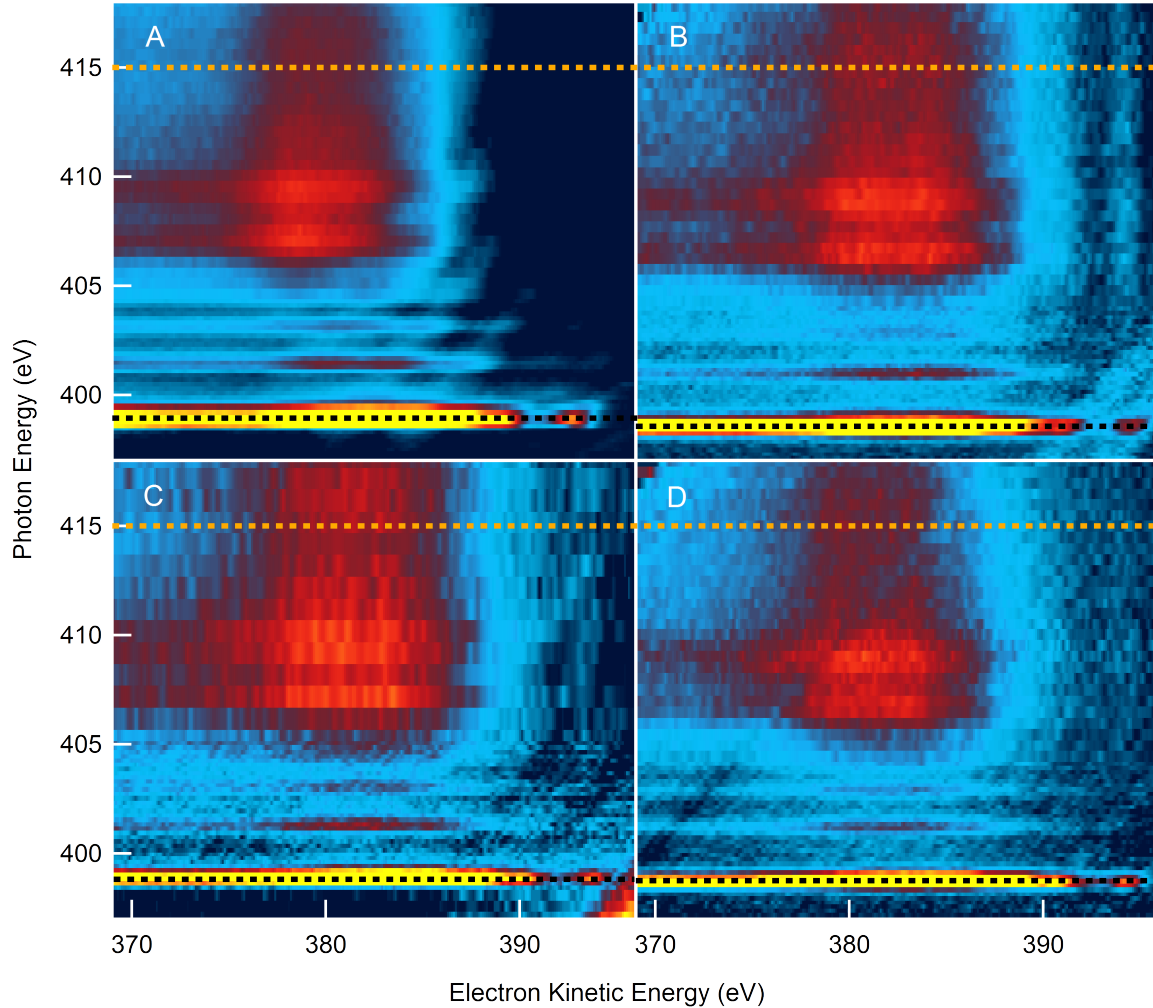


Figure 3.5: Nitrogen K-edge RPES maps of (A) BP multilayer on Au(111) (B) BP monolayer on Au(111), (C) BP monolayer on epitaxial graphene and (D) BP monolayer on GNR. The LUMO resonance scans are taken along the dashed black lines. The dashed orange lines indicate the energy used for the scans above the ionization edge.*

In Figure 3.5, we show nitrogen K-edge RPES maps of a BP multilayer on Au(111) and a BP monolayer on Au(111), epitaxial graphene and GNR. We see the N1s to LUMO

CHAPTER 3. CHARGE TRANSPORT AT HYBRID INTERFACES

transition signature around photon energy of 399 eV. From these maps, we obtain the line scans that are shown in Figure 3.3 of the main text. The core-hole clock method described below is then used to determine the charge transfer time and the fraction of the LUMO* that drops below the Fermi level in the monolayer systems.

3.6.4 RPES Core-Hole Clock Method with Charge Back Donation

In this section, we present the extension of the standard core-hole clock method [52] to obtain the bidirectional charge transfer time and the fraction of the LUMO* that drops below the Fermi level from the RPES measurements.

In the core-hole clock method, a core electron is photoexcited to the LUMO, leaving a core-hole on the molecule; and the energy distribution of the subsequent electron emission is measured. The process relevant to the core-hole clock method is the filling of the core-hole and the subsequent emission of an electron, leaving the LUMO empty; this is denoted as the participator decay. In a coupled system, the participator decay gets quenched if the charge transfer to the substrate occurs within the core-hole life-time. Therefore, by comparing the participator decay intensities in the isolated and the coupled system, the charge transfer time in the coupled system can be determined as has been done before. [52] In the measurements presented here, when a core-hole is present, the LUMO* is partially below the Fermi level and can thus get occupied due to a charge transfer from the substrate.

To determine the bidirectional charge transfer time, one needs to consider two types of decay process that will contribute to the participator decay intensity. First, there is a photoemission type participator decay that occurs from the LUMO* electron excited from the core level. Additionally, there is an Auger type participator decay (from the

CHAPTER 3. CHARGE TRANSPORT AT HYBRID INTERFACES

fraction of the LUMO* that is below Fermi) that can occur after charge transfer from the LUMO* to the substrate. Denoting the participator decay intensity as I_o in the isolated system and as I_c in the coupled system, we can get a relation between I_o and I_c as

$$I_c = I_o \frac{\tau_{ct}}{\tau_{ct} + \tau_{ch}} + I_o x \frac{\tau_{ch}}{\tau_{ct} + \tau_{ch}} \quad (3.1)$$

where τ_{ch} is the core-hole lifetime, τ_{ct} is the charge transfer time, x is the fraction of the LUMO* below the Fermi level. The first term in Eq. 3.1 is the standard expression that has been used before and is attributed to the photoemission type participator decay. [52] The second term is due to the Auger type participator decay that can occur only if the LUMO* is partly below Fermi and charge transfer from the LUMO* to the substrate has occurred. The process giving rise to the second term in Eq. 3.1 is identical to the Auger type participator decay occurring after the charge transfer from the substrate to LUMO* following an excitation of a core electron above the ionization edge. We denote this process as the super-participator decay and its intensity (I_s) is given by

$$I_s = I_o x \frac{\tau_{ch}}{\tau_{bt} + \tau_{ch}} \quad (3.2)$$

Here, τ_{bt} is the bidirectional charge transfer time.

Since the charge transfer time in both directions is equal, Eq. 3.1 and Eq. 3.2 can be solved to find x and τ_{ct} which yields

$$\tau_{ct} = \tau_{ch} \frac{f(1 - \beta)}{1 - f(1 - \beta)} \quad (3.3)$$

$$x = \frac{f\beta}{1 - f(1 - \beta)} \quad (3.4)$$

CHAPTER 3. CHARGE TRANSPORT AT HYBRID INTERFACES

where f is I_c / I_o and β is I_s / I_c .

The equations above are valid when the light polarization is perpendicular to the nodal plane of the nodal plane of the molecular π -system. Therefore, we need to account for the fact that the molecular π -system makes a small angle with the substrate, as determined from NEXAFS measurements presented in the main text. We also need to consider the light polarization when comparing the Auger type super-participant intensities with photoemission type participant intensity since there is a clear angular dependence in the latter.

The photoemission type participant decay intensity is proportional to $(\varepsilon \cdot n)^2$ where ε is the polarization unit vector and n is the vector normal to the nodal plane of the molecular π -system. We calculate the $(\varepsilon \cdot n)^2$ as a function of ε and n assuming that there is no azimuthal dependence on the molecular orientation on the surface. We use

$$\varepsilon = \sin\theta\hat{x} + \cos\theta\hat{z} \quad (3.5)$$

$$n = \sin\alpha\cos(\phi - \pi/2)\hat{x} + \sin\alpha\sin(\phi - \pi/2)\hat{y} + \cos\alpha\hat{z} \quad (3.6)$$

where θ is the polar angle between the surface normal and the polarization unit vector, α is the polar angle between the surface normal and the normal to the molecular π -system, and ϕ is the azimuthal angle of the molecular π -system.

Averaging $(\varepsilon \cdot n)^2$ over ϕ , and using Eq. 3.5 and Eq. 3.6 we get

$$\overline{(\varepsilon \cdot n)^2} = \sin^2\theta\sin^2\alpha/2 + \cos^2\theta\cos^2\alpha \quad (3.7)$$

Since measurements are performed at the magic angle ($\theta = 54.7^\circ$), $\cos^2\theta = \sin^2\theta/2$, and

CHAPTER 3. CHARGE TRANSPORT AT HYBRID INTERFACES

thus the average $(\varepsilon \cdot n)^2$ is independent of α . We obtain

$$I_c^m = I_o^m \frac{\tau_{ct}}{\tau_{ct} + \tau_{ch}} + \frac{I_o^m}{\cos^2 \theta} x \frac{\tau_{ch}}{\tau_{ct} + \tau_{ch}} \quad (3.8)$$

$$I_s^m = \frac{I_o^m}{\cos^2 \theta} x \frac{\tau_{ch}}{\tau_{bt} + \tau_{ch}} \quad (3.9)$$

where I_c^m , I_s^m and I_o^m are the measured intensities at the magic angle. Solving Eq. 3.8 and Eq. 3.9 yields

$$\tau_{ct} = \tau_{ch} \frac{f(1 - \beta)}{1 - f(1 - \beta)} \quad (3.10)$$

$$x = \frac{\cos^2 \theta f \beta}{1 - f(1 - \beta)} \quad (3.11)$$

where f is I_c^m / I_o^m and β is I_s^m / I_c^m .

Chapter 4

Flicker Noise Characteristics of Single-Molecule Junctions

4.1 Preface

This chapter is based on the manuscript entitled *Flicker Noise as a Probe of Electronic Interaction at Metal-Single Molecule Interfaces* by Olgun Adak, Ethan Rosenthal, Jeffery Meisner, Erick F. Andrade, Abhay N. Pasupathy, Colin Nuckolls, Mark S. Hybertsen and Latha Venkataraman published in Nano Letters. [137]. The experimental work was done by Olgun Adak and Ethan Rosenthal. Theoretical work was conducted by Mark S. Hybertsen at Center for Functional Nanomaterials, Brookhaven National Labs, Upton, NY, and Olgun Adak. The chemical synthesis was done by Jeffery Meisner at Chemistry Department of Columbia University, New York, NY.

4.2 Abstract

Charge transport properties of metal-molecule interfaces depend strongly on the character of molecule-electrode interaction. Although through-bond coupled systems have attracted the most attention, through-space coupling is important in molecular systems when, for example, through-bond coupling is suppressed due to quantum interference effects. To date, a probe that clearly distinguishes these two types of coupling has not yet been demonstrated. Here, we investigate the origin of flicker noise in single-molecule junctions and demonstrate how the character of the molecule-electrode coupling influences the flicker noise behavior of single-molecule junctions. Importantly, we find that flicker noise shows a power law dependence on conductance in all junctions studied with an exponent that can distinguish through-space and through-bond coupling. Our results provide a new and powerful tool for probing and understanding coupling at metal/molecule interfaces.

4.3 Introduction

For electronic devices based on organic semiconductors, the interaction of the molecular orbitals with the electronic states of the metal dictates the energy level alignment and the electronic coupling, which determine device performance. [138], [139] The physical interactions at such interfaces can lead to electronic coupling that is characterized as either through-bond or through-space. In the former, the hybridization between the molecular orbitals and the electronic states of the metal occurs through a chemical bond, while in the latter, orbitals responsible for charge transfer do not participate in specific bond formation. [140] The most important consequence of this difference is that conductance in systems with through-space coupling is generally lower than in those with through-bond coupling. [98], [141], [142] As a result, performance of devices relying on through-space

CHAPTER 4. FLICKER NOISE CHARACTERISTICS OF SINGLE-MOLECULE JUNCTIONS

coupling is often limited by the characteristics of the organic/metal interface rather than by the organic constituents. [143]

Here, we investigate the characteristics of flicker noise in a series of nanoscale junctions including gold point-contact and single-molecule junction. [72], [144]–[148] We find that flicker noise measurements can clearly differentiate between through-bond and through-space coupling at the single-molecule level. We first show that at room temperature, flicker noise in single-molecule junctions originates from changes in the molecule-electrode coupling due to electrode atoms switching between metastable configurations. We then demonstrate how scaling of flicker noise with conductance is determined by the relationship between the electronic transport channel and the mechanical bond to the electrodes. We find that in tunnel junctions where two electrodes are mechanically decoupled and electronic transport is via through-space tunneling, flicker noise power exhibits a strong dependence on individual junction conductance: noise power scales as G^2 . This decreases to a $G^{1.7}$ dependence when we probe a molecular system where both sides are mechanically bonded to the respective electrodes, but through-bond electronic coupling is present on only one side. When single-molecule charge transport is mediated fully by through-bond interactions on both sides, the scaling diminishes to $G^{1.1}$. Finally, for nanoscale gold contacts with $G > 4 \times G_0$, the core of the junction is mechanically and electronically well coupled, and as a result insensitive to nearby fluctuations in the junction structure; conductance fluctuates through changes in the number of channels at the periphery resulting in a noise power that scales as $G^{0.5}$. This measurement technique thus enables us to infer the relative contributions of through-space and through-bond coupling at molecule-metal interfaces, providing a new and powerful tool for characterizing these interfaces.

CHAPTER 4. FLICKER NOISE CHARACTERISTICS OF SINGLE-MOLECULE JUNCTIONS

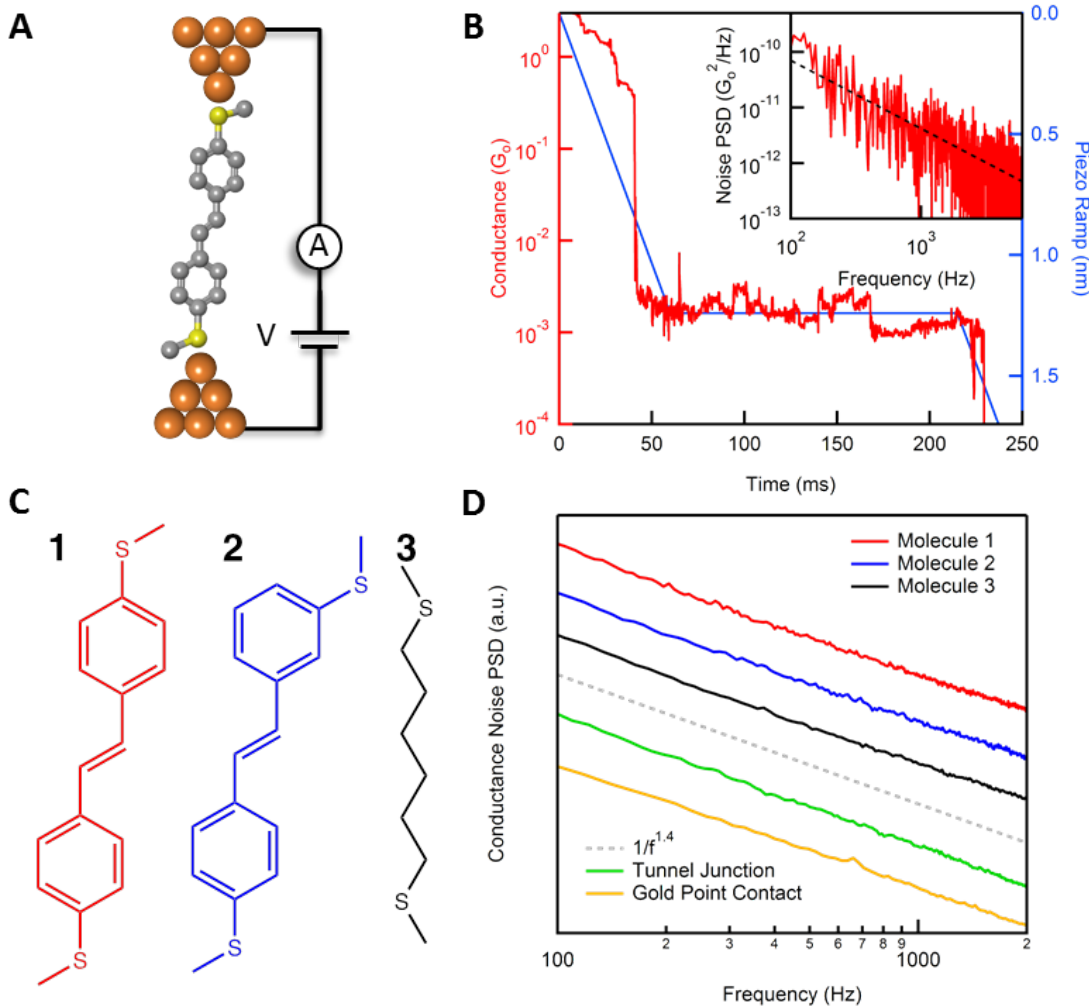


Figure 4.1: (A) Schematic for molecular junction conductance measurements. (B) Representative conductance and displacement traces for a single noise measurement. Inset: The conductance noise power spectral density obtained by taking square of the discrete Fourier transform of the constant displacement section of conductance trace in B. The dashed line indicates a $f^{-1.4}$ dependence. (C) Chemical structures of the molecules under the study. (D) The averaged conductance noise PSD's for all five systems showing flicker noise along with a line indicating the $f^{-1.4}$ dependence. Traces are offset laterally for clarity.

4.4 Experimental Technique

In this work, we use the scanning tunneling microscope-based break-junction technique (STM-BJ) [36], [37] to characterize conductance noise. In this technique, a gold tip is repeatedly moved in and out of contact with a gold substrate while conductance of the junction is recorded (see Figure 4.1A for schematic). In order to measure the conductance noise, the junction elongation procedure is paused for 100 ms at a position where prior measurements indicate that a stable junction is likely to form (see Figure 4.1B). During this time, conductance is recorded at an applied bias of 200 mV using a sampling rate of 100 kS/s. Traces that have a conductance within the two standard deviations of the molecular conductance histogram peak at the beginning and the end of this 'hold' period are selected for analysis. In order to determine the conductance noise power spectral density (PSD) for a junction, the conductance measured during the fixed displacement section of the trace is analyzed. A discrete Fourier transform of the data is obtained and squared to get the PSD. A sample PSD measured for a 4,4'-di-(methylthio)stilbene junction (molecule **1**) is shown in the inset of Figure 4.1B. [142] This type of noise is often called flicker noise or $1/f$ noise and its presence in single-molecule junctions has not yet been explained. [144]–[146] In Figure 4.1D, the conductance PSD, averaged over hundreds of junctions, are shown for tunnel junctions, gold point-contacts and three molecules considered here (see Figure 4.1C for structures). At room temperature, the noise power shows a $f^{-1.4}$ frequency dependence. The frequency dependence of flicker noise power is identical in all five systems indicating that the source of flicker noise is related to the electrodes and not to the system bridging the electrodes. (As detailed in Section 4.7.1, Figure 4.5 and 4.6, the observed flicker noise is not due to electronic or mechanical effects in our set-up.)

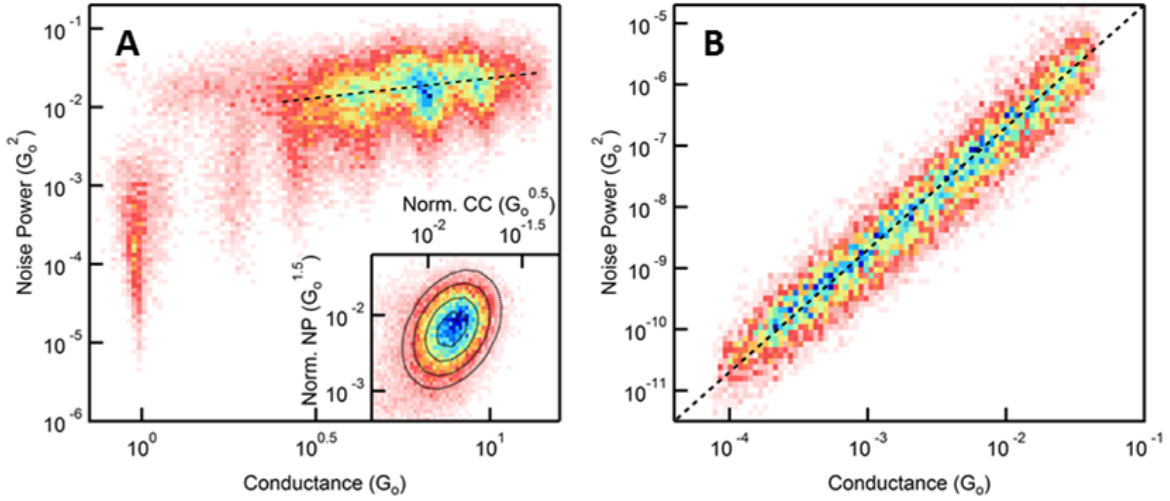


Figure 4.2: (A) Two-dimensional histogram of the flicker noise power against the average conductance in gold point-contacts. Line overlaid shows a square root dependence. Inset: Two-dimensional histogram of the normalized flicker noise power (NP) against the normalized conductance change (CC) induced by a mechanical oscillation. (B) Two-dimensional histogram of the flicker noise power against the average conductance in tunnel junctions.

4.5 Results and Discussion

We hypothesize that flicker noise in all three systems arises from configuration changes in the electrode structure due to electrode atoms proximal to the junction fluctuating between metastable positions. As the measured noise shows a clear $f^{-1.4}$ dependence, we can rule out any suppression of noise due to quantum interference effects and shot noise. [72] Such fluctuations have been shown to cause two-level conductance fluctuations in both tunnel junctions and gold point-contacts at temperatures ranging from 7 K to 100 K. [149]–[151] We therefore argue that room temperature, flicker noise is a consequence of many accessible two-level conductance fluctuations, with average switching rates dis-

CHAPTER 4. FLICKER NOISE CHARACTERISTICS OF SINGLE-MOLECULE JUNCTIONS

tributed over the measurement bandwidth, which result in a noise power spectrum with a f^{-n} frequency dependence. [152]

To verify this hypothesis, we first examine flicker noise in gold point-contacts with conductance ranging from 1 to $10 G_0$ at room temperature. To quantify noise, we numerically integrate the PSD from 100 Hz to 1 kHz for every junction and take this value as the measure of flicker noise a junction experiences. The 1 kHz upper limit in the frequency range is chosen because the thermal noise of the current amplifier becomes comparable to flicker noise at frequencies above this cutoff. The lower limit is chosen considering the mechanical drifts in the experimental setup; such drifts result in an f^{-2} frequency dependence, which become comparable to flicker noise at low frequencies. In Figure 4.2A, we make a two-dimensional histogram of the integrated flicker noise against the average conductance for 50000 gold point-contacts. We find that the integrated flicker noise power dips near the integer multiple of G_0 which is not surprising because junctions with fully open conductance channels have transmissions that are less sensitive to junction structure. [153] The dips occur at conductance values that are slightly lower than the integer multiples of G_0 due to an effective series resistance caused by scattering centers near the contact. [46] We also note that the noise power scales as $G^{0.5}$ for contacts with a conductance greater than $4 G_0$. To probe this further, we compare the relation between flicker noise and the change in conductance when we perturb the junction with an external oscillatory mechanical perturbation (see Figure 4.7). We find that junctions that are less susceptible to conductance changes upon mechanical perturbation experience less flicker noise (see Figure 4.2A inset and Section 4.7.2 for details).

This is consistent with our hypothesis that flicker noise arises due to configurational changes in the electrode structure. In contrast to gold point-contacts, flicker noise in tunnel junctions that form after the rupture of the gold point-contact shows a different

CHAPTER 4. FLICKER NOISE CHARACTERISTICS OF SINGLE-MOLECULE JUNCTIONS

relation to the average conductance. We measure flicker noise for 10000 tunnel junctions with G_{AVG} ranging from $10^{-4} G_0$ to $10^{-1.4} G_0$ and show a two-dimensional histogram of the noise power against G_{AVG} in Figure 4.2B. We observe a clear quadratic dependence of the flicker noise power on the junction conductance; i.e., the noise power scales with G^2 .

To understand the observed scaling of the noise power, we consider the impact of fluctuations in gold atom positions in these junctions. For the case of the tunnel junctions, the junction gap size effectively fluctuates due to the position of atoms on either electrode near the area of closest approach between the tip and the substrate. Since these tunneling gaps are probed right after a rupture event, the current is exponentially sensitive to the overall gap width in general, but also to the position of just a few gold atoms that effectively define it, as would be expected from the atomic resolution in a scanning tunneling microscope in the regime of an atomically sharp tip. The conductance of a tunnel junction can be written as $G = G_c e^{-\beta z} = G_c e^{-\beta z_0} e^{-\beta(z-z_0)}$ where b is the decay constant, z is the effective gap size that fluctuates around a mean value z_0 and G_c is a constant. The scale of fluctuations in z is bounded and independent of the average gap z_0 , and therefore also of $G_{AVG} = G_c e^{-\beta z_0} \langle e^{-\beta(z-z_0)} \rangle$ with $e^{-\beta(z-z_0)}/\langle e^{-\beta(z-z_0)} \rangle$ describing the fluctuations around G_{AVG} . It then follows that the noise amplitude (noise in $G = G_{AVG}(e^{-\beta(z-z_0)}/\langle e^{-\beta(z-z_0)} \rangle)$) scales with G_{AVG} and the noise power scales as G_{AVG}^2 . This result can be easily derived under the assumption of Gaussian fluctuations in z (see Section 4.7.3), although it applies to fluctuations that follow more general distributions. On the other hand, for the gold point-contacts, the conductance scales approximately with the number of atoms in the junction cross-section area. If fluctuations are limited to a single atom, then the noise power is independent of G_{AVG} . However, the entire perimeter is open for fluctuations. Assuming each fluctuating center is inde-

CHAPTER 4. FLICKER NOISE CHARACTERISTICS OF SINGLE-MOLECULE JUNCTIONS

pendent, the number of possible centers will scale with the square root of the number of atoms in the contact and the noise power scales as $G^{0.5}$ as observed for contacts with a conductance greater than $4 G_0$ (see Section 4.7.4).

To further check the validity of our model, we measure the temperature dependence of flicker noise in tunnel junctions and gold point-contacts under ultrahigh vacuum conditions. Since the switching of atoms between metastable positions is a thermally activated process, at sufficiently low temperatures, single two-level conductance fluctuations should be discernible. We show, in Figure 4.3A, sample conductance versus time traces measured for stable tunnel junctions at temperatures ranging from 5.5 to 300 K. Flicker noise is clearly visible at room temperature but decreases substantially upon cooling. At 40 K, single two-level conductance fluctuations are visible; at 5.5 K, no noise is seen. To quantify this result in a statistically significant way, we collect conductance-time traces for over 10000 different tunnel junctions at each temperature. We obtain the noise power density at 100 Hz, instead of numerically integrating up to 1 kHz because the electronic and the mechanical noise features appear in the spectrum at low temperatures due to the suppressed flicker noise. We normalize this by G_{AVG}^2 to remove the conductance dependence and plot the result averaged over 10000 traces against temperature in Figure 4.3B. We see that the flicker noise power decreases rapidly with decreasing temperature attaining the experimental noise floor below 40 K. We take the average of the values obtained below 40 K as representative of the experimental noise floor and subtract this from measurements at higher temperatures and higher voltages. An exponential decrease in noise down to 40 K with increasing inverse temperature ($1/T$) is visible in Figure 4.3B. Such a decrease is typical for a thermally activated two-level systems. [154] Furthermore, we observed a strong bias voltage dependence of flicker noise in tunnel junctions at 5.5 K but not at 300 K (see Figure 4.3B). [155] As detailed in Section 4.7.5, the observed voltage dependence

CHAPTER 4. FLICKER NOISE CHARACTERISTICS OF SINGLE-MOLECULE JUNCTIONS

can be fit with a model where bias voltage electrostatically lowers the potential barrier for the two-level fluctuations (see Figure 4.8A). [156] Taken together, these experimental results show clearly that fluctuations in the position of atoms on the electrodes lead to flicker noise. More importantly, the activation energies for these fluctuations have a broad energy distribution as they are observed within the experimental bandwidth over a wide temperature range.

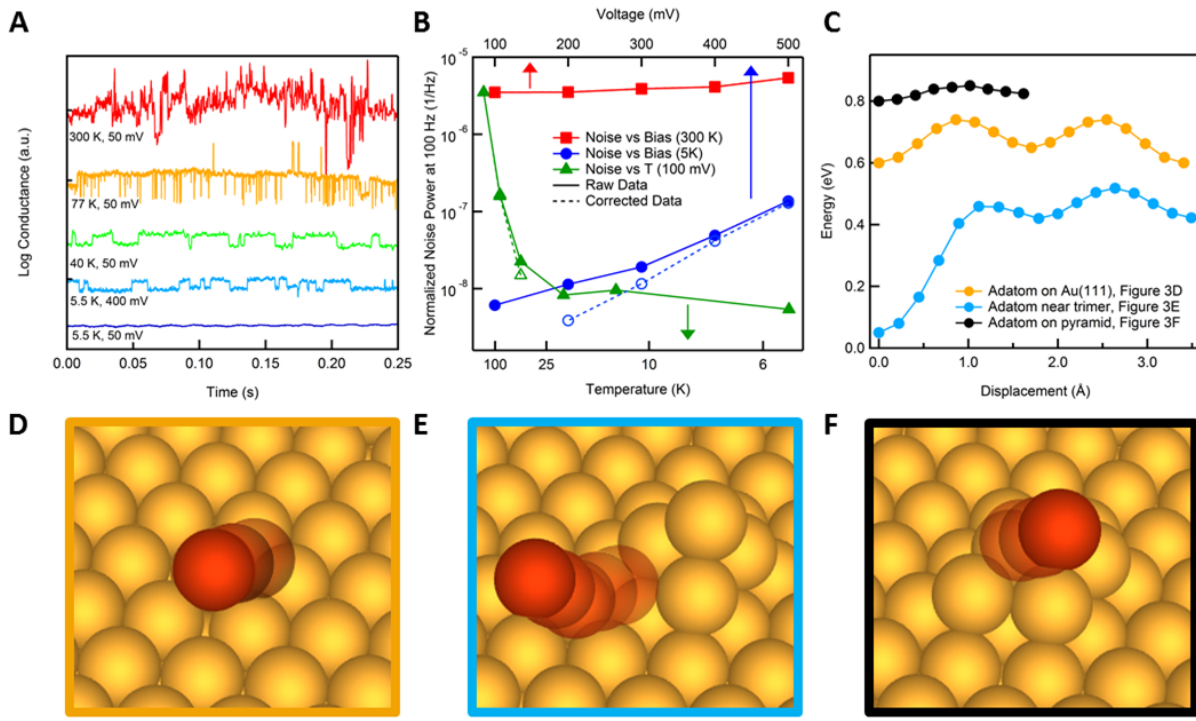


Figure 4.3: (A) Representative tunnel junction conductance traces (from top to bottom) at 300 K (50 mV), 77 K (50 mV), 40 K (50 mV), 5.5 K (400 mV) and 5.5 K (50 mV). (B) Green: The normalized noise power density plotted against the temperature (lower axis) at 100 mV bias. The normalized noise power density at 100 Hz versus the bias voltage (top axis) at 300 K (red) and at 5.5 K for junctions with a conductance of $10^{-3} G_0$ (blue). Filled shapes represent the measured values, empty shapes with dashed connecting lines represent the values after background subtraction. Note that for the data taken at

CHAPTER 4. FLICKER NOISE CHARACTERISTICS OF SINGLE-MOLECULE JUNCTIONS

300 K, background subtraction does not change the values significantly. (C) Potential energy profiles calculated using a density functional theory approach for a series of three illustrative structures and gold atom movements: (D) Adatom diffusion pathway on the close packed (111) surface from fcc to hcp to neighboring fcc hollow sites (yellow data in C); (E) Dissociation of a five atom asperity into a four atom pyramid and an adatom, first to an hcp site and then to a neighboring fcc site (blue data in C); (F) Switching of an apical adatom in a five atom asperity between a local fcc and hcp sites (black data in C). Curves are offset for clarity; only relative energies within each curve are meaningful.

To get more insight into the kinetic processes that can result in such fluctuations in the junction, we use density functional theory (DFT)-based calculations, as implemented in the VASP package [100], [157]–[159], to simulate the potential surface for atomic-scale fluctuations in gold asperities (as detailed in Section 4.7.6). We first consider the diffusion of an adatom on a close-packed (111) surface. The fcc hollow site is most stable for the adatom. Diffusion from one fcc hollow site to another goes through a metastable hcp hollow site. As shown in Figure 4.3C, we find a primary barrier of 0.14 eV (fcc to hcp) and a secondary barrier of 0.09 eV (hcp to fcc) for this diffusion path that is illustrated in Figure 4.3D. This shows that in the simplest geometry considered, there are two accessible states that have different lifetimes. Since we expect the experimental tip and substrate structures to be more complex with additional roughness, we also explored the affinity of the adatom to other local clusters. For example, Figure 4.3E shows that an adatom is bound to a site adjacent to a four-atom pyramid. Once bound, fluctuations away from this state are controlled by a relatively large barrier (0.4 eV) while the barrier for return is rather small (0.04 eV). Furthermore, the calculations show that the specific size of these barriers depends on the cluster geometry and the neighboring structures. This

CHAPTER 4. FLICKER NOISE CHARACTERISTICS OF SINGLE-MOLECULE JUNCTIONS

example suggests a physical mechanism for the fluctuations in Figure 4.3A that appear as spikes (yellow trace measured at 77 K), having asymmetric lifetimes for the two states involved. Finally, with the idea that rather sharp asperities can survive longer at the lower temperatures probed here, we show an example of an adatom fluctuating at the tip of such an asperity (Figure 4.3F), where the forward barrier is about 0.05 eV and the reverse barrier is less than 0.03 eV. The reduced energy scale follows from the lower overall coordination of the atoms involved.

Unlike tunnel junctions, gold point-contacts do not exhibit any two-level conductance fluctuations at 77 K under 100 mV bias voltage implying that atomic fluctuations that alter junction structure have substantially increased activation energies. Increasing the bias voltage, however, does result in two-level conductance fluctuations in gold point-contacts at 77 K (see Section 4.7.5, Figure 4.8). We do not attempt to distinguish between local heating and electrostatic effects of the bias voltage that leads to an increase in flicker noise for these point-contacts. However, we note that the room temperature flicker noise at 50 mV in atomic contacts is greater than the noise at 77 K at a 400 mV bias voltage (see Figure 4.8), while the local electronic temperature in 3 to 5 G_0 gold point-contacts has been shown to increase by 300 K under 300 mV bias voltage at room temperature. [160] This means that bias induced local hot electron population can be achieved at the apex without elevating the lattice temperature significantly, possibly because the electron-electron scattering length is smaller than electron-phonon scattering length in gold. [29]

We now turn to single-molecule junctions and examine the flicker noise characteristics of three molecular systems, 4,4'-di-(methylthio) stilbene (molecule **1**), 3,4'-di-(methylthio) stilbene (molecule **2**) and 2,9-dithiadecane (molecule **3**) at room temperature. Molecules **1** and **2** are synthesized as described previously [142] and **3** is obtained from Alfa-Aesar and used without further purification. Molecule **1** forms stable Au-single-molecule-Au

CHAPTER 4. FLICKER NOISE CHARACTERISTICS OF SINGLE-MOLECULE JUNCTIONS

junctions through Au-S donor-acceptor bonds with a conductance around $1.3 \times 10^{-3}G_0$ as shown in Figure 4.4A in agreement with previous measurements. [142] Molecule **2** also forms single-molecule junctions that are mechanically anchored through two Au-S donor-acceptor bonds. However, at the meta-linker, through-bond conduction is suppressed due to destructive interference effects since the orbital that dominates transport in these systems, the highest occupied molecular orbital (HOMO), does not have any weight on the meta-linker. [88], [161] As a result, charge transfer is mediated by through-space interaction on the meta-side, and through-bond at the other which reduces the conductance to $1.6 \times 10^{-4}G_0$. [142] Molecule **3** is an alkane terminated with methylsulfide linkers that conducts by through-bond tunneling via its σ -system. Its conductance is peaked around $3.1 \times 10^{-4}G_0$, significantly smaller than that of **1** where the π -system mediates the charge transport.

To examine the noise in these systems, we measure the conductance of more than 10000 stable junctions for each molecular system at a 200 mV bias voltage. For the noise analysis, we follow the same procedure illustrated in Figure 4.1B, at room temperature and calculate the total noise power between 100 Hz and 1 kHz for each junction by numerically integrating the PSD. In Figure 4.4B-D, we show a two-dimensional histogram of the integrated flicker noise power normalized by G_{AVG} against G_{AVG} for **1**, **2**, and **3**. We see that the normalized flicker noise power in **1** and **3** is insensitive to junction conductance, while that of **2** correlates strongly with junction conductance. Quantitatively, the noise power in **1** and **3** scales with $G^{1.1}$ and $G^{1.0}$ respectively. In **2**, the noise power scales with $G^{1.7}$, which is interestingly close to the results of the tunnel junctions (see Figure 4.9 and see Section 4.7.7 for analysis details). As shown in Figure 4.10 for two additional molecules, we find that through-bond coupled molecular junctions show a noise power scaling close to $G^{1.2}$, while for junctions with one through-bond and one through-space

CHAPTER 4. FLICKER NOISE CHARACTERISTICS OF SINGLE-MOLECULE JUNCTIONS

coupling, it scales with $G^{1.7}$.

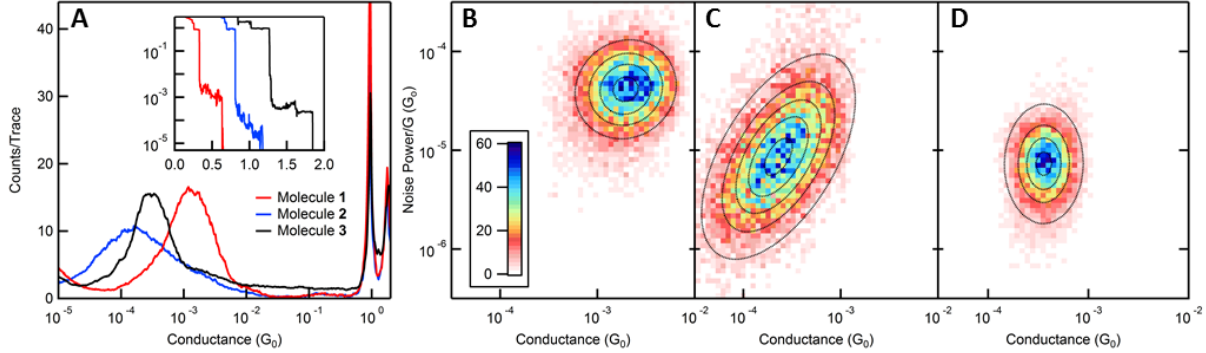


*Figure 4.4: (A) Conductance histograms of molecule **1**, molecule **2** and molecule **3**. Inset: sample traces. (B-D) Two-dimensional histogram of the normalized flicker noise power against the average conductance for molecule **1** (B), molecule **2** (C), molecule **3** (D). Dotted contours represent fits to the bivariate normal distribution.*

In order to understand these results, we consider the simplest model for transport through a single-molecule junction [80] where conductance is determined by the energy level alignment of the conducting molecular orbital with the electrode Fermi energy ($E_{Frontier}$) and its electronic coupling to the electrodes (Γ). While both play a role, Γ is strongly influenced by the electrode structure, the binding geometry and the conformational changes in molecular structure. [94], [162]–[165] In particular, Γ changes appreciably for different tip structures on the electrodes, [94] so fluctuations in the Au atoms between metastable positions in the electrode result in changes in the junction conductance. For a through-bond coupled molecule, we can assume that fluctuations in Γ are independent of Γ as there is a mechanical constraint that maintains the electrode-molecule separation. For a through-space coupled molecule, fluctuations in Γ are proportional to Γ , because Γ decreases exponentially with the distance between the molecule and the electrode site (see Section 4.7.8). With these assumptions, it can be analytically shown that the flicker

CHAPTER 4. FLICKER NOISE CHARACTERISTICS OF SINGLE-MOLECULE JUNCTIONS

noise power in a molecular junction with through-bond coupling at both ends scales with the average conductance of the molecular junction, explaining the behavior of **1** and **3**. In contrast, for a molecular junction with through-space coupling at both ends, the flicker noise power scales with the square of the average conductance (see Section 4.7.8 for analytic derivation). This is what we obtain experimentally for the tunnel junctions, a through-space coupled system. Molecule **2** is a hybrid system with both through-bond and through-space coupling. For such a system, it is not possible to obtain an analytical expression for the relation between noise and conductance. Through a Monte-Carlo simulation, we find that the noise scaling in this hybrid system is determined by the linker that controls the junction-to-junction variations in conductance (see Figure 4.11). Specifically, if through-space coupling has a larger variation, the noise scaling is closer to that of a tunnel junction, while if the through-bond coupling has a larger variation, the noise scaling is closer to that of a through-bond coupled junction. Interestingly, if through-space and through-bond couplings have the same distribution width, the scaling exponent turns out to be 1.5 regardless of the mean through-space and through-bond coupling. The example of **2**, with a scaling exponent 1.7, must have a distribution of through-space coupling that is wider than that of through-bond coupling. This is intuitive as through-space coupled molecular junctions exhibit a broader distribution of conductance compared with the through-bond coupled junction as can be seen in Figure 4.4A.

In general, we note that there can be other aspects of the junction structure that fluctuate and contribute to noise, possibly leading to changes in both Γ and $E_{Frontier}$, including rotational degrees of freedom of the molecule or linker reattachment and changes to the local electrostatic potential that affect $E_{Frontier}$. For molecules **1** and **2**, the twisting of molecular backbone is hindered by the presence of C=C double bond in stilbene backbone so that internal rotations do not contribute to noise. [166] Although rotations

CHAPTER 4. FLICKER NOISE CHARACTERISTICS OF SINGLE-MOLECULE JUNCTIONS

about the Au-S-C torsion angle are possible, the activation energy is very small [167] and thus the conductance changes due to these rotations could only be seen at frequencies higher than our instrument bandwidth. Indeed, measurements of a control molecule that does not accommodate changes to the Au-S-C torsion angle show that noise power scales as $G^{1.2}$ (see Figure 4.10), consistent with the results of molecule **1**. Breaking and reattachment of the Au-S donor-acceptor bond, with an energy around 0.6 eV, could contribute to the measured noise. [154], [167] However, as detailed in Section 4.7.9, we do not find any evidence of reattachment within the 100 ms time-scale of the measurement. Finally, we note that linkers can switch between metastable binding sites on the electrode. [164] Since this can be modeled as a change in Γ for the junction, it does not yield a separate source of noise for the molecular junctions.

4.6 Conclusion

In conclusion, we show that flicker noise observed at room temperature in molecular junctions, gold point-contacts and tunnel junction is due to many two-level positional switching of electrode atoms. We demonstrate how the character of the electronic coupling in single-molecule junctions determines the flicker noise-conductance relation. Specifically, we show that through-bond coupling leads to a linear noise-conductance relation, while through-space coupling results in a quadratic one. This gives us ability to distinguish between through-space and through-bond coupling at metal-organic interfaces without referring to electronic structures.

4.7 Supporting Information

4.7.1 Set-up and Measurement Details

The Experimental Set-up

The block diagram of the room temperature experimental set-up is shown in Figure 4.5A. A voltage is applied to the junction using a digital to analog converter (NI PXI-4461), while the current through the junction is converted to voltage using a transimpedance amplifier (Keithley 428-PROG and Femto DLPCA-200). The voltage output of the transimpedance amplifier and the voltage across the junction are recorded at 100 kS/s using A/D inputs on the NI PXI-4461. A resistor (R_s) is placed in series with the junction to prevent an overload in the transimpedance amplifier when the junction resistance is low. Neither the transimpedance amplifier nor the data acquisition card have a 1/f noise comparable to what we measure for the junctions. Mechanical perturbations to our set-up are damped above 5 Hz by a two-stage vibration isolation system. The resonance frequency of our piezoelectric transducer is around 10 kHz.

CHAPTER 4. FLICKER NOISE CHARACTERISTICS OF SINGLE-MOLECULE JUNCTIONS

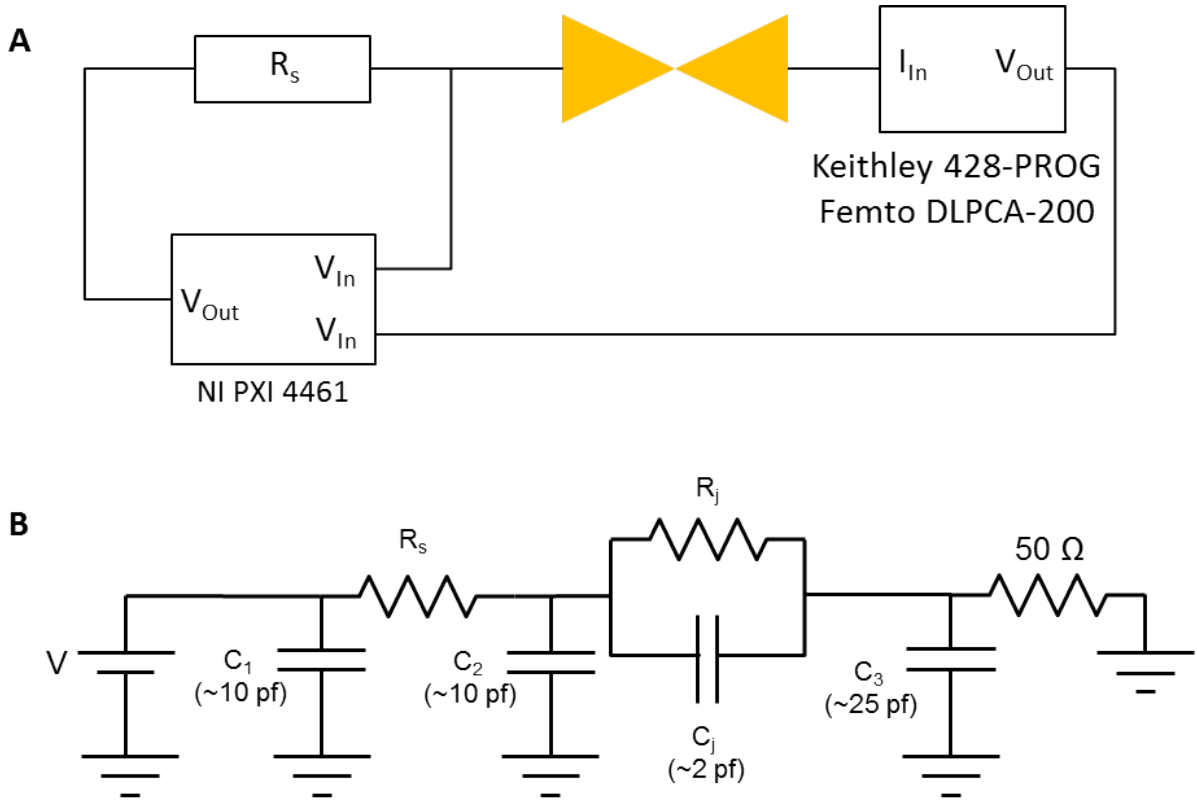


Figure 4.5: (A) Block diagram of STM-BJ circuitry used for both room temperature and low-temperature measurements. (B) Details of the circuit showing all resistances and capacitances.

Figure 4.5B shows the circuit diagram: C_1 , C_2 , C_3 are the cable capacitances, C_j denotes the junction capacitance. The transimpedance amplifier has a 50Ω input impedance. Since any current that passes through C_1 does not go through the junction, C_1 does not affect the measured current. Although C_2 has an impedance comparable to the junction impedance at 1 kHz, it does not affect the conductance measurement since the junction conductance is obtained by dividing the measured current through the junction by the measured voltage across the junction. C_3 is in parallel with the transimpedance amplifier. At 1 kHz, the impedance of C_3 is $6.4 \times 10^6 \Omega$ which is not comparable to 50Ω input impedance of the amplifier thus C_3 does not affect the measurement. The effect

CHAPTER 4. FLICKER NOISE CHARACTERISTICS OF SINGLE-MOLECULE JUNCTIONS

of C_j on conductance measurement depends on R_s . In the absence of the series resistor, C_j does not affect the DC conductance measurement. However, when the series resistor is present, the voltage across the junction changes with the junction resistance, which involves charging or discharging of C_j . From the RC time constant for this capacitor (with $R_s = 100 \text{ k}\Omega$) we see that frequency beyond which these capacitive effects matter is 1 MHz, well above the range used here, thus the junction capacitance not does limit the measurements presented here. For experimental verification, we obtain the transfer function within the measurement bandwidth by measuring the current through the circuit while applying a white voltage noise when the gold tip is in contact with the substrate. The transfer function within 100 Hz to 1 kHz bandwidth is flat and equal to 1 as shown in Figure 4.6A.

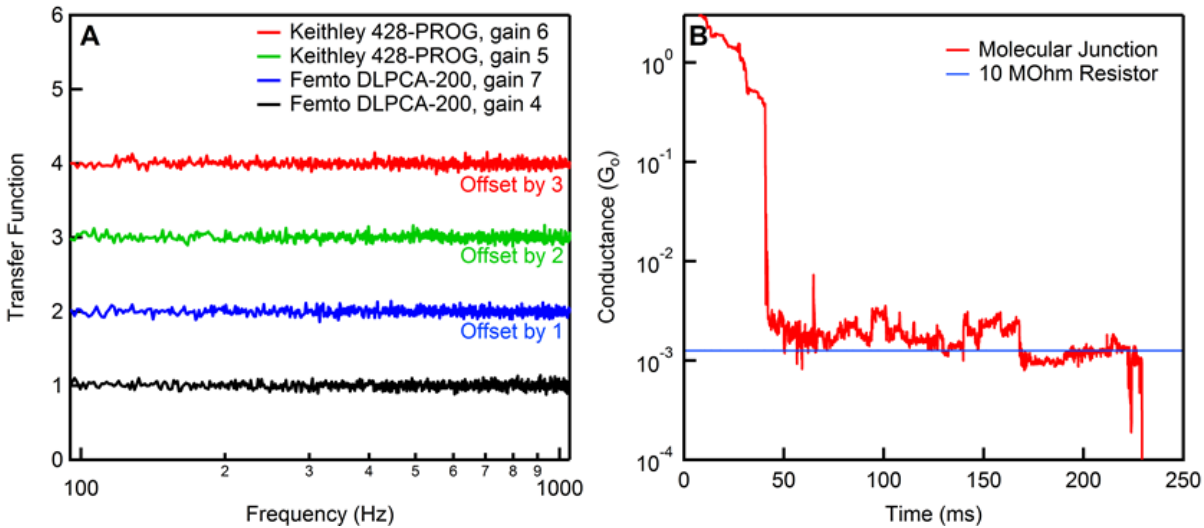


Figure 4.6: (A) The transfer functions of the experimental set-up within the experimental bandwidth. The traces are offset vertically for clarity. (B) Comparison of conductance of 10 M Ω resistor and a molecular junction measured with the experimental set-up showing that the instrument noise is negligible.

Analysis of Additional Noise Sources

CHAPTER 4. FLICKER NOISE CHARACTERISTICS OF SINGLE-MOLECULE JUNCTIONS

The additional noise sources can be divided into two categories: instrumental and physical noise. The former contains noise from the current to voltage (IV) converter, the voltage probe and the voltage source. The latter contains shot noise and thermal noise.

Room Temperature Measurements:

The total measured instrumental conductance noise within the measurement bandwidth (100-1000 Hz) is $3.4 \times 10^{-13} G_0^2$ for tunnel junction and molecular junction measurements at room temperature. This is measured using a NI-PXI 4461 voltage probe, a Keithley 428-PROG gain 10^6 IV converter under a bias voltage of 200 mV applied using the NI-PXI 4461 card. The instrumental conductance noise for the gold point-contact at room temperature is $4.4 \times 10^{-11} G_0^2$. This is measured using a NI-PXI 4461 voltage probe, a Femto DLPCA-200 gain 10^5 IV converter under a bias voltage of 50 mV applied using the NI-PXI 4461 card. These values are at least two orders of magnitude smaller than the flicker noise measured for the corresponding junctions (see Figure 4.2, Figure 4.9 and 4.10) thus instrumental noise is clearly not significant. The manufacturer reported noise in the voltage source is less than $8.5 \times 10^{-15} V^2/Hz$ and not measurable with the voltage probe. The corresponding conductance noise in each system is orders of magnitudes less than the instrumental noise originating from the IV converters and the voltage probe, and is therefore insignificant. In Figure 4.6B, we compare the conductance of a $10 M\Omega$ resistor and a molecular junction measured with the same set-up where it is clear that the instrument noise is negligible.

The thermal current noise of a junction is given by $4kbT/R A^2/Hz$. The corresponding conductance noise is $4.8 \times 10^{-12}/G G_0$ for molecular junctions and tunnel junctions measured under a 200 mV DC bias, and $7.7 \times 10^{-11}/G G_0$ for gold point-contacts measured under a 50 mV DC bias, where G is in the units of G_0 . These numbers are orders of magnitudes smaller than the instrumental noise for the corresponding junctions and can

CHAPTER 4. FLICKER NOISE CHARACTERISTICS OF SINGLE-MOLECULE JUNCTIONS

safely be neglected. Shot noise in gold point-contacts is even smaller than thermal noise at room temperature, and requires lock-in type measurements and RF amplifiers. [148], [160] To date, shot noise in molecular junctions and tunnel junctions at room temperature has not been measured. Therefore, our flicker noise measurements at room temperature are clearly orders of magnitude above any instrumental noise and much larger than other noise of physical origin.

Low Temperature Measurements:

The measured instrumental conductance noise density at 100 Hz is $2.8 \times 10^{-17} G_0/\text{Hz}$ for tunnel junction low temperature measurements. This is measured using a NI-PXI 4461 voltage probe, a Femto DLPCA-200 gain 10^7 IV converter under a bias voltage of 100 mV applied using the NI-PXI 4461 card. The measured instrumental conductance noise density at 100 Hz is $5.2 \times 10^{-12} G_0^2/\text{Hz}$ for gold point-contact measurements at 77 K. This is measured using a NI-PXI 4461 voltage probe, a Femto DLPCA-200 gain 10^4 IV converter under a bias voltage of 50 mV applied using the NI-PXI 4461 card. These values are obtained by measuring the conductance noise after the corresponding junction ruptures. This noise is primarily due to the thermal noise in the IV converters. In the analysis of tunnel junctions, the noise power density is normalized by the square of conductance to remove conductance dependence. The contribution to measured normalized noise from the instrumental noise floor is $2.8 \times 10^{-10} \text{ Hz}^{-1}$ for junctions with a conductance of $10^{-3.5} G_0$ and $2.8 \times 10^{-14} \text{ Hz}^{-1}$ for junctions with a conductance of $10^{-1.5} G_0$. These values are much smaller than the normalized conductance noise measured in our experiments as shown in Figure 4.3B and Figure 4.8. The thermal noise in all systems is smaller than the room temperature thermal noise, while shot noise is temperature independent. Thus, the thermal noise and shot noise are orders of magnitudes smaller than the instrumental noise. The primary source of signal observed at low temperatures in the absence of

CHAPTER 4. FLICKER NOISE CHARACTERISTICS OF SINGLE-MOLECULE JUNCTIONS

two-level fluctuations is due to the drifts in the piezoelectric transducer rather than the instrumental noise or noises of physical origin. We note that the drift induced noise is insignificant compared to the noise measured at room temperature.

4.7.2 Gold Point-Contacts with Mechanical Perturbation

To probe the relation between flicker noise and the mechanical stability of a gold point-contact, an AC oscillation at 10 kHz with amplitude around 0.1 nm is applied to the tip during the noise measurement. The conductance change due to the mechanical perturbation is determined from the AC component of the conductance at 10 kHz.

In Figure 4.7A, we show the conductance change due to AC oscillation of the tip at 10 kHz against the average conductance for 50000 gold point-contacts as a two-dimensional histogram. We see dips at conductance values slightly lower than the integer multiples of G_0 similar to what was seen in Figure 4.2A of the manuscript. The 10 kHz conductance change scales with $G^{0.6}$ above $4 G_0$, again similar to what is seen in Figure 4.2A ($G^{0.5}$) indicating that the atoms on the periphery of the junction are primarily responsible for the change in conductance upon mechanical perturbation.

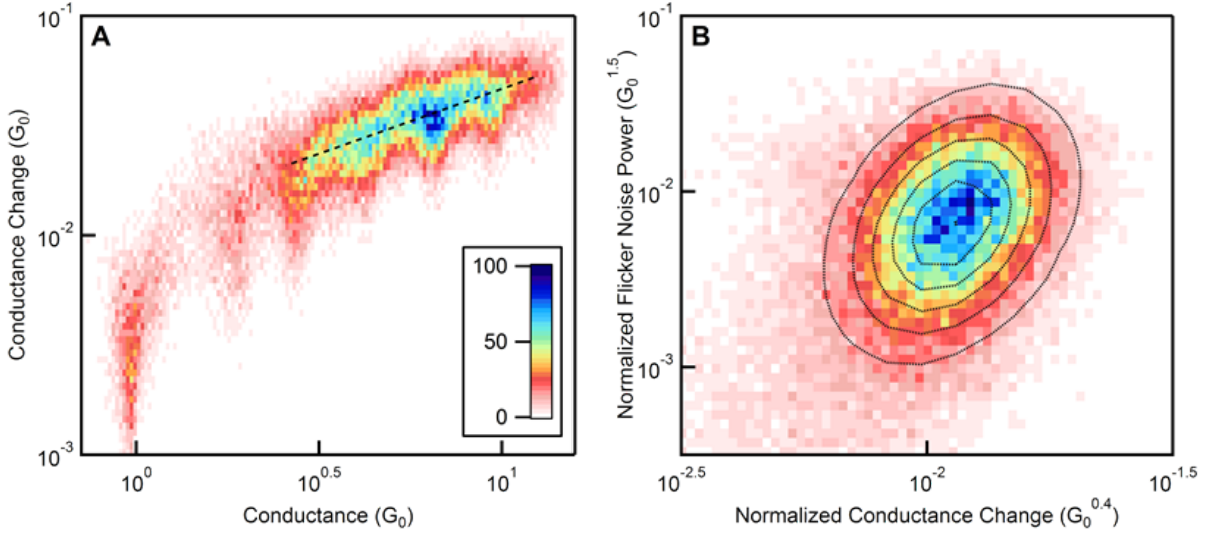


Figure 4.7: (A) Two-dimensional histogram of the conductance change due to the mechanical perturbation against the average conductance in gold point-contacts. (B) Two-dimensional histogram of the normalized conductance change due to the mechanical perturbation against the normalized flicker noise power in gold point-contacts.

We show, in Figure 4.7B the correlation between the flicker noise power normalized by $G^{0.5}$ (from data shown in Figure 4.3A) and the conductance change due to the mechanical perturbation normalized by $G^{0.6}$ (from Figure 4.7A). The clear correlation seen here demonstrates that junctions that are more susceptible conductance change upon mechanical perturbation experience more flicker noise.

4.7.3 Scaling of Flicker Noise in Tunnel Junctions

For $G(z) = G_c e^{-\beta z}$ and a Gaussian distribution of z , $p(z) = \frac{1}{\sqrt{2\pi\sigma^2}} e^{\frac{(z-z_o)^2}{2\sigma^2}}$, the average conductance is

$$\langle G \rangle = \int_{-\infty}^{\infty} dz G_c e^{-\beta z} \frac{1}{\sqrt{2\pi\sigma^2}} e^{\frac{(z-z_o)^2}{2\sigma^2}} \quad (4.1)$$

CHAPTER 4. FLICKER NOISE CHARACTERISTICS OF SINGLE-MOLECULE JUNCTIONS

Upon integration, this yields

$$\langle G \rangle = G_c e^{-\beta z + \beta^2 \sigma^2} \quad (4.2)$$

Likewise, for the average of the square of fluctuations,

$$\langle \Delta G^2 \rangle = \int_{-\infty}^{\infty} dz G_c^2 e^{-2\beta z} \frac{1}{\sqrt{2\pi\sigma^2}} e^{\frac{(z-z_0)^2}{2\sigma^2}} - \langle G \rangle^2 \quad (4.3)$$

which yields

$$\langle \Delta G^2 \rangle = \langle G \rangle^2 [e^{2\beta^2 \sigma^2} - 1] \quad (4.4)$$

which clearly shows the noise power is proportional to $\langle G \rangle^2$

4.7.4 Scaling of Flicker Noise in Gold Point-Contacts

The conductance of a gold point-contact is approximately one unit of G_0 per atom in the contact cross-section area. Fluctuations due to Au atom motion take place at the edge of the contact area, so the number of possible sites subject to fluctuations should scale with the circumference of the junction, assuming these sites are accessible to diffusing atoms. While junctions that approach a single atom scale may be physically less accessible due to mechanical elongation and deformation, junctions above a certain conductance or area should have an accessible circumference. We assume that flicker noise is the net effect of independent events where each available site around the circumference can host a fluctuating, two-level system. Then the flicker noise power, which scales as the number of two-level systems, is proportional to the square root of the conductance.

4.7.5 Voltage Dependence of Flicker Noise

There are two possible mechanisms for noise increase with the bias voltage; a local heating of the junction due to loss of electron energy by scattering that excites vibrations or a lowering of potential barrier for atomic motion on the electrodes. [149]–[151] In order to distinguish between the two different mechanisms, we measure the conductance noise in tunnel junctions at voltages ranging from 100 mV to 500 mV with conductance ranging from $10^{-1.4} G_0$ to $10^{-4} G_0$. In Figure 4.8A, red and blue circles show the voltage dependence of conductance noise power density at 100 Hz at 5.5 K with conductance $10^{-2 \pm 0.5} G_0$ and $10^{-3 \pm 0.5} G_0$ respectively. Dots represent the measured values, empty circles represent the values after background subtraction. As stated in the manuscript, for all low-temperature data, we choose to take the noise density at 100 Hz instead of integrating from 100 Hz to 1 kHz to minimize impact from external noise in the set-up. If the increase in the noise is due to a local heating of the electrodes, the average local temperature of junctions can be determined from the temperature dependence of the low-bias flicker noise measurements (e.g., the green trace in Figure 4.3B). Under a 0.5 V bias, junctions with conductance $10^{-2 \pm 0.5} G_0$ and $10^{-3 \pm 0.5} G_0$ have a noise power density of $3.7 \times 10^{-7} \text{ Hz}^{-1}$ and $1.4 \times 10^{-7} \text{ Hz}^{-1}$ respectively, according to the exponential dependence of noise on temperature in Figure 4.3B, which would imply a very modest difference in temperature (~ 25 K). However, these junctions differ in conductance by an order of magnitude, and in general, one would expect that local heating, which scales approximately as GV^2 , would be significantly larger for junctions with higher conductance. Therefore, local heating cannot explain the voltage-induced noise measured here. We also see that the noise increases exponentially with the applied voltage. This indicates that the voltage effectively decreases the barrier for atomic motion on the electrode surfaces, yielding a modified two-level system as detailed by Muller, et.al. [156]

CHAPTER 4. FLICKER NOISE CHARACTERISTICS OF SINGLE-MOLECULE JUNCTIONS

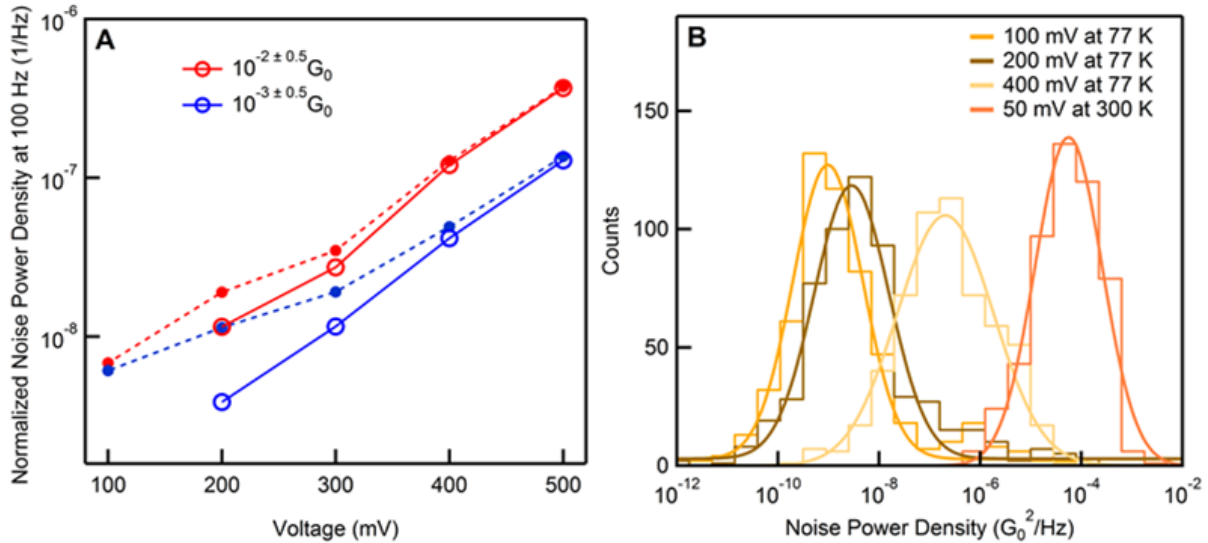


Figure 4.8: (A) The noise power density at 100 Hz normalized by the square of the average junction conductance plotted against the bias voltage in tunnel junctions with the average conductance around $10^{-2 \pm 0.5} G_0$ (red) and $10^{-3 \pm 0.5} G_0$ (blue). Dots represent the measured values, empty circles represent the values after background subtraction. (B) Histograms for the conductance noise power density at 100 Hz in gold point-contacts with a conductance ranging between $3 G_0$ and $6 G_0$.

In gold point-contacts, at 77 K, we do not see switching events under 50 mV bias voltage. However, as we increase the bias, conductance fluctuations are observed as shown in Figure 4.8B as the noise density is increasing above the experimental noise floor obtained at 50 mV bias voltage.

4.7.6 DFT Calculation Details

For the DFT studies, model structures were developed based on a 3 monolayer (ML) slab of gold atoms modeling a close-packed (111) surface, with different adatom superstructures added on one side and a minimum of 10 Å of vacuum separation. The back

CHAPTER 4. FLICKER NOISE CHARACTERISTICS OF SINGLE-MOLECULE JUNCTIONS

two ML were held fixed at distances according to the cubic lattice parameter of $a=4.175$ Å, determined from the optimized bulk lattice parameter computed under the present computational conditions (PAW method with the PBE function, 400 eV energy cutoff to determine the planewave basis set size and a uniform, G-centered mesh of k-points with 15 points in each direction to sample the Brillouin zone). Surface supercells with area 3×3 , 4×4 and 5×5 relative to the basic hexagonal unit cell were considered, giving different degrees of separation between periodic replicas of the adatom superstructures. Surface Brillouin sampling was roughly commensurate with 15 k-points in each direction in the bulk. Potential surfaces displayed in Figure 4.3 were mapped between metastable basins. Initial coordinates were obtained by linear interpolations, followed by relaxation with the x-y coordinates of the adatom under study held fixed. Dipole corrections were included for test structures, but found to have no appreciable impact on the energy differences reported here (1 meV scale). All of the results reported in Figure 4.3C were obtained with 4×4 supercells. The basic energies characterizing adatom diffusion (hcp to fcc hollow energy difference [32, 49, 55 meV] and bridge site barrier from the fcc hollow [129, 140, 143 meV]) depend only weakly on super cell size (3×3 , 4×4 and 5×5 , respectively). However, the potential pathway for separation of an atom away from a larger superstructure, such as dissociation of the 5 atom structure in Figure 4.3E into a 4 atom pyramid and a separated adatom, show larger variations with supercell size. In particular, with an increase to a 5x5 cell, the relative energy of the structure with the separated adatom increased from 370 to 460 meV in the first hcp metastable site and from 370 to 450 meV in the next fcc metastable site. Periodic replicas are close enough to influence the energetics, largely due to strain effects. Direct estimates of electrostatic dipole effects were much smaller. Overall, since our purpose is to illustrate scenarios and the real surfaces under study are likely rough, such variations largely serve to underscore the diversity of energy barriers

CHAPTER 4. FLICKER NOISE CHARACTERISTICS OF SINGLE-MOLECULE JUNCTIONS

that govern Au atomic rearrangements under realistic conditions.

4.7.7 Scaling of Flicker Noise in Molecular Junctions

In the top panel of Figure 4.9, we show two-dimensional histograms of flicker noise power against conductance. A power-law dependence between these observables is seen in these figures with noise power being proportional to G^n where n is the scaling exponent.

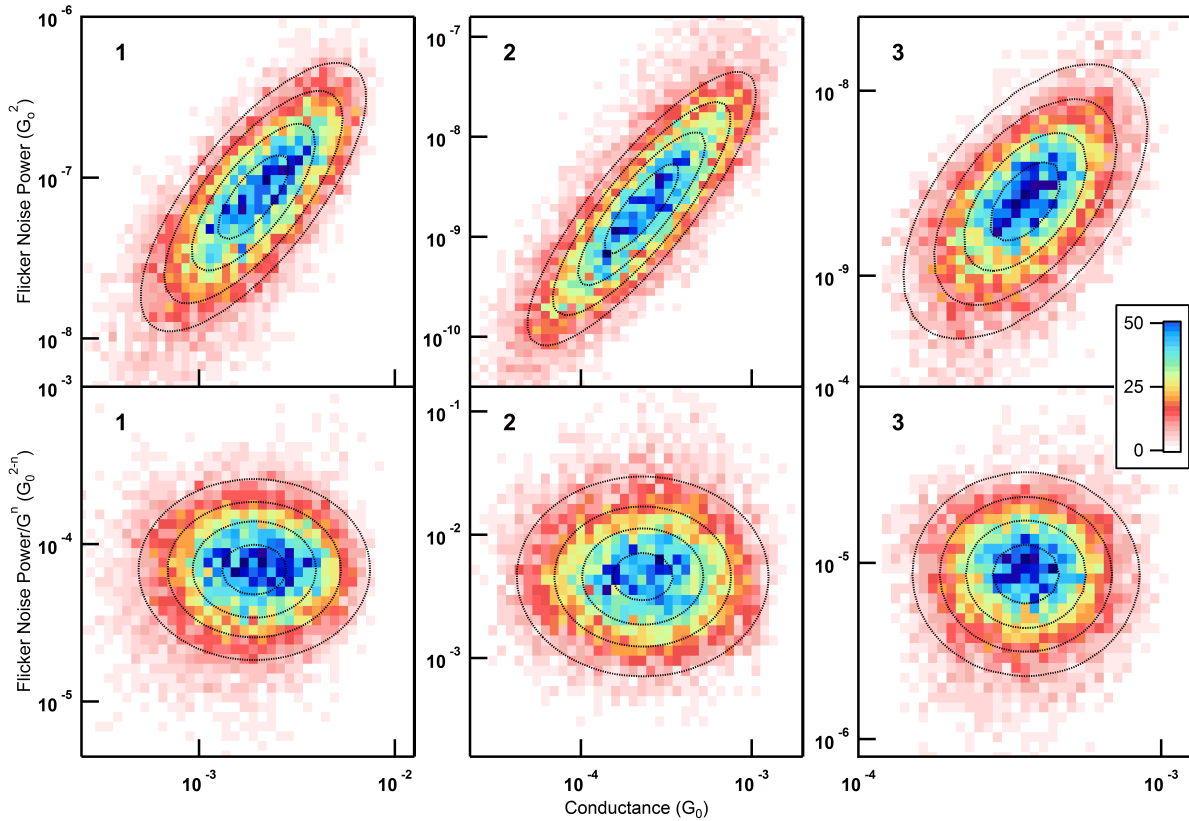


Figure 4.9: (Top) Two-dimensional histograms of the flicker noise power against the average conductance for molecules **1**, **2**, and **3** respectively. (Bottom) Two-dimensional histograms of the flicker noise power normalized by $G^{1.1}$, $G^{1.7}$ and $G^{1.0}$ against the average conductance for molecules **1**, **2**, and **3** respectively.

CHAPTER 4. FLICKER NOISE CHARACTERISTICS OF SINGLE-MOLECULE JUNCTIONS

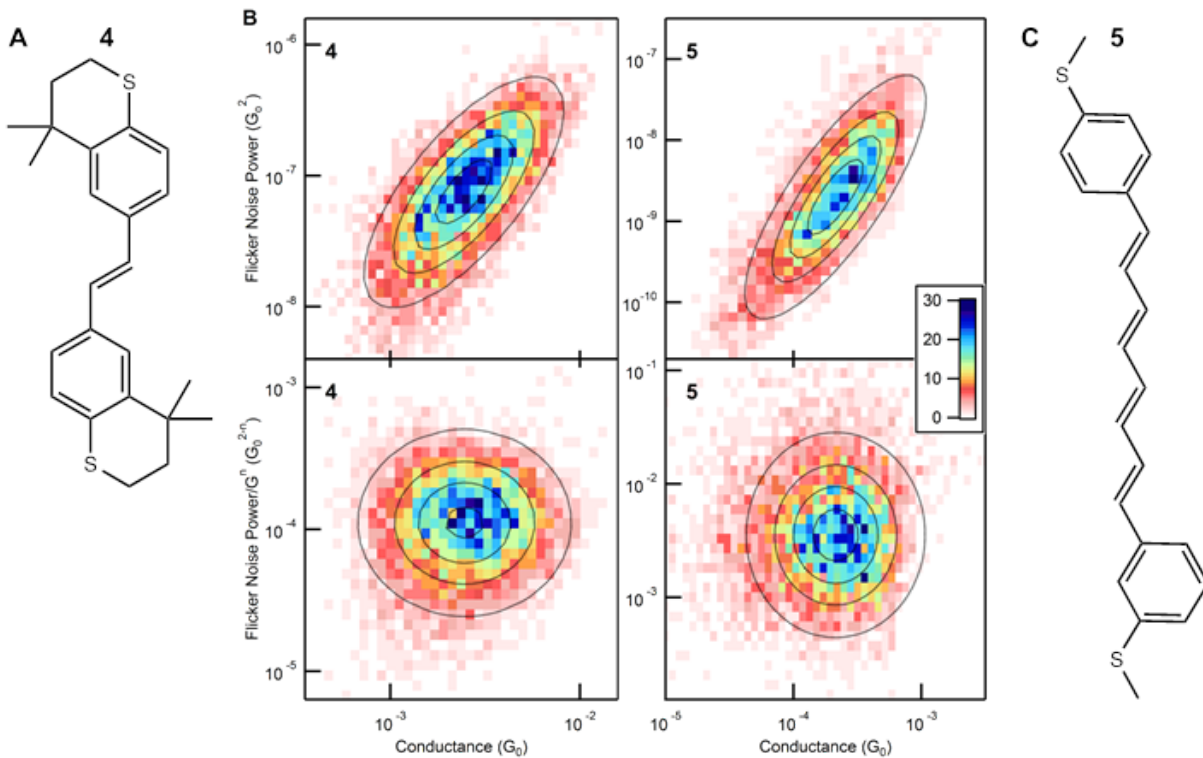


Figure 4.10: (A) Chemical structure of 4. (B) (Top) Two-dimensional histograms of the flicker noise power against the average conductance for molecules 4 and 5 respectively. (Bottom) Two-dimensional histograms of the flicker noise power normalized by $G^{1.2}$ and $G^{1.7}$ against the average conductance for molecules 4 and 5 respectively. (C) Chemical structure of 5.

In order to determine the scaling exponent, we normalize the flicker noise power by G^n using values for n ranging from 0.5 to 2.5 in steps of 0.01. For each n , we obtain the correlation between the normalized flicker noise power and the average conductance by fitting to the bivariate normal distribution. The value of n that leads to zero correlation between the normalized flicker noise power and the average conductance is taken as the scaling exponent. Results from this analysis for molecules 1, 2 and 3 are shown in Figure 4.9. In addition, we show data for a control through-bond coupled molecule, 1,2-

CHAPTER 4. FLICKER NOISE CHARACTERISTICS OF SINGLE-MOLECULE JUNCTIONS

bis(4,4-dimethylthiochroman-6-yl)ethylene (**4**), and a second hybrid molecule with one through-bond and one through-space coupling (**5**) in Figure 4.10. The synthesis of these compounds are described in Batra et al [168] and Meisner et al. [142] Molecule **4** has a scaling exponent of 1.2 while molecule **5** has a scaling exponent of 1.7.

4.7.8 Model for Scaling of Flicker Noise Power in Molecular Junctions

In the simplest physical picture, the transmission function ($T(E)$) that describes the probability of charge transfer across a molecular junction can be modeled by a Lorentzian function [80] and we have

$$T(E) = \frac{\Gamma_1\Gamma_2}{(E - E_{Frontier})^2 + (\Gamma_1 + \Gamma_2)^2/4} \quad (4.5)$$

where, $E_{Frontier}$ denotes the position of the frontier molecular orbital level relative to the Fermi level (E_F). For low bias measurements, $G = G_0 T(E_F)$. Then, in the limit that Γ is much smaller than $E_{Frontier}$, the conductance can be approximated as

$$G = G_0 \frac{\Gamma_1\Gamma_2}{(E - E_{Frontier})^2} \quad (4.6)$$

Now, while the fluctuations on the two sides of the junction are independent, assume that the average electronic coupling (Γ_{AVG}) and the range of the fluctuations ($\Delta\Gamma$) are the same. Then the fluctuations in conductance can be written as

$$\Delta G = 2G_{AVG} \frac{\Delta\Gamma}{\Gamma_{AVG}} \quad (4.7)$$

CHAPTER 4. FLICKER NOISE CHARACTERISTICS OF SINGLE-MOLECULE JUNCTIONS

where $G_{AVG} = G_0 \frac{\Gamma_{AVG}^2}{(E - E_{Frontier})^2}$

In a through-space coupled system, the molecular orbital coupling strength (Γ) decreases exponentially with the distance, because Γ is proportional to the overlap between the exponentially decaying tails of the electrode and molecular wavefunctions. The effect of the motion of the electrode atoms (the two-level fluctuations) on Γ comes from the modification of the distance between coupling sites, z , as

$$\Gamma = Ae^{-\beta z} \quad (4.8)$$

where β is the decay constant and A is a prefactor. This can be written as

$$\Gamma = Ae^{-\beta z_o} e^{-\beta(z-z_o)} \quad (4.9)$$

where z_o is the average distance between through-space coupled sites. Similar to the derivation presented in the manuscript for tunnel junction, we get

$$\Gamma = \Gamma_{AVG} \frac{e^{-\beta(z-z_o)}}{\langle e^{-\beta(z-z_o)} \rangle} \quad (4.10)$$

where $\Gamma_{AVG} = Ae^{-\beta z_o} \langle e^{-\beta(z-z_o)} \rangle$

Therefore, the fluctuations in Γ are proportional to Γ_{AVG} . Assuming both electrodes are coupled through-space to the molecule, we have $\Delta\Gamma/\Gamma_{AVG}$ as a constant and according to Eq. 4.7, we find that $\Delta G \propto G_{AVG}$. Therefore, the flicker noise power scales with G_{AVG}^2 in a system with only through-space electronic coupling at the electrodes. This is in parallel with the vacuum tunneling case already considered.

When the electronic coupling is through-bond, the mechanical bond (Au-S donor-acceptor in the cases under study here) puts constraints on the bond length and other

CHAPTER 4. FLICKER NOISE CHARACTERISTICS OF SINGLE-MOLECULE JUNCTIONS

geometrical factors, such as bond and backbone orientation that influence the electronic coupling. The adjacent electrode structure including the Au atomic organization around the point of contact Au atom, also affects the electronic coupling. [94] If we consider the ensemble of junctions, all of these factors change with each junction in the ensemble resulting in a distribution of electronic coupling and conductance. However, in a given junction, we hypothesize that the primary source of fluctuations is confined to the Au atomic organization. Therefore, we expect the range of the dynamical fluctuations ($\Delta\Gamma$) to be independent of the average value for a given junction (Γ_{AVG}), as born out by explicit simulations. [94] In this case, following the derivation above, we get

$$\Delta\Gamma = G_0^{0.5} G_{AVG}^{0.5} \Delta\Gamma / E_{Frontier} \quad (4.11)$$

Since $E_{Frontier}$ depends only weakly on Γ , [94] the flicker noise magnitude scales with $G_{AVG}^{0.5}$, hence the flicker noise power scales with G_{AVG} in such a system.

To understand the behavior of a hybrid system, we consider a single molecular level connected to the electrodes by a through bond coupling ($\Gamma_1 = \Gamma_{bond}$) on one side and a through-space ($\Gamma_2 = \Gamma_{space}$) coupling on the other. In order to sample the conductance fluctuations, we use Eq. 4.5 together with a Monte-Carlo simulation in which, for each junction in the ensemble, we pick a value for Γ_{bond} and Γ_{space} assuming lognormal distributions, with the form

$$f(\Gamma) = \frac{1}{\Gamma\sigma\sqrt{2\pi}} e^{\frac{-\log(\Gamma/\Gamma_0)^2}{2\sigma^2}} \quad (4.12)$$

parameterized by a median value Γ_0 and a standard deviation σ . Here, Γ_0 has units of energy while σ is unitless. This choice is motivated by the experimental observation that logarithmically binned conductance histograms show normal peak distributions. With the

CHAPTER 4. FLICKER NOISE CHARACTERISTICS OF SINGLE-MOLECULE JUNCTIONS

approximation of a fixed value of $E_{Frontier}$, this regenerates the conductance distribution. For the simulation discussed below, we consider two such lognormal distributions defined in Eq. 4.12 above, one for each side of the junction with a median value $\Gamma_{0,space}$ and $\Gamma_{0,bond}$ and a corresponding standard deviation σ_{space} and σ_{bond} .

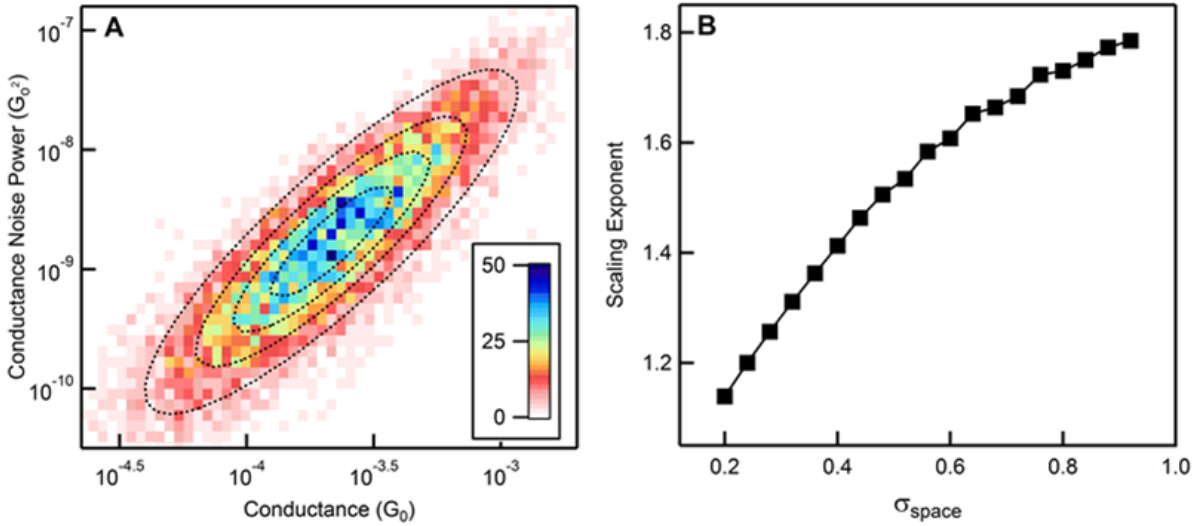


Figure 4.11: (A) Two-dimensional histogram of the conductance noise power against the average conductance from the Monte Carlo simulation. The parameters used for this simulation are: $\Gamma_{0,bond} = 90$ meV, $\Gamma_{0,space} = 9$ meV, $\sigma_{bond} = 0.47$, $\sigma_{space} = 0.74$, $\sigma_{noise} = 14$ meV. (B) The scaling exponent versus the standard deviation of the through-space coupling strength.

To simulate the conductance fluctuations, we assume that Γ_{bond} varies in time through a white Gaussian noise with zero mean and standard deviation σ_{noise} . This models a fluctuation in Γ_{bond} that is independent of Γ_{bond} . We then assume that Γ_{space} varies in time through a noise that is the product of $\Gamma_{space}/\overline{\Gamma_{bond}}$ and a white Gaussian noise with zero mean and standard deviation σ_{noise} . Γ_{bond} , Γ_{space} and σ_{noise} has units of energy. This allows us to have a Γ_{space} with fluctuations proportional to Γ_{space} , as detailed above.

CHAPTER 4. FLICKER NOISE CHARACTERISTICS OF SINGLE-MOLECULE JUNCTIONS

The factor of $\overline{\Gamma_{bond}}$ is introduced to ensure that when $\Gamma_{space} = \overline{\Gamma_{bond}}$, fluctuations in Γ_{space} are on the same scale with Γ_{bond} since noise source is the same in both cases. Next, conductance traces are calculated by assuming single-Lorentzian transmission with conducting molecular orbital located 2 eV away from the Fermi level, though choice of this value is not important since it is just a multiplicative factor relating coupling to conductance. The average conductance and the conductance noise power (the variance of the conductance) are obtained for each trace. This procedure is repeated 10000 times to create a two-dimensional histograms of the conductance noise power versus the average conductance as shown in Figure 4.11A. For this simulation, we tune the parameters $\Gamma_{0,bond}$, $\Gamma_{0,space}$, σ_{bond} , σ_{space} and σ_{noise} to model the results of molecule **2** shown in Figure 4.9.

Next, we vary the model parameters to understand how they affect the noise scaling exponent. We find that $\Gamma_{0,bond}$, $\Gamma_{0,space}$ and σ_{noise} do not affect the scaling exponent. However the ratio between σ_{bond} and σ_{space} does control it. To demonstrate this, we fix σ_{bond} at 0.47 and vary σ_{space} from 0.2 to 0.9. We find that the scaling exponent ranges from 1.1 to 1.8 over this range as shown in Figure 4.11B. For $\sigma_{bond} = \sigma_{space}$, we get an exponent of 1.5. We conclude that the hybrid systems we have studied experimentally have a Γ_{space} that varies more from junction to junction than Γ_{bond} , consistent with the fact that the width of the conductance histogram for **2** is larger than that of **1**.

4.7.9 Rotations and Rupture of the Au-S Linker Bond

Rotations about the Au-linker bond: In order to examine the effect of linker rotations on flicker noise in molecular systems, we compare results from measurements of **1** and **4**. Junctions formed with **4** have the orientation of the Au-S bond rigidly locked relative to the terminal benzene rings, while in **1**, this Au-S bond can rotate freely (see Figure 4.10A for chemical structure). [167] In Figure 4.12A, we compare the flicker noise power of **1** and

CHAPTER 4. FLICKER NOISE CHARACTERISTICS OF SINGLE-MOLECULE JUNCTIONS

4, and see that these are very similar. Furthermore, as we have shown, in Figure 4.10B, flicker noise scales with $G^{1.2}$, which is very similar to the behavior of the other through-bond systems investigated here. We conclude that the rotations about the Au-S bond in **1** do not contribute to flicker noise measured here.

Rupture and reattachment of the Au-linker bond: Prior DFT calculations indicate that the Au-S bond has a binding energy of about 0.6 eV. [167], [169] At room temperature, within the 100 ms experimental timescale, events that involve the linker-Au bond rupture are observable. We find that 10% of molecular junctions do rupture during 100 ms measurement time. These are however not included in our noise analysis, thus the relevant Au-linker bond rupture events that can contribute to the measured noise involve junctions where the bond ruptures and reforms within the 100 ms measurement time. To see how frequently such events are measured, we compare conductance data during the 100 ms section for **1**, **2** and **3** junctions with that of the instrument noise determined after a junction is broken. In Figure 4.12B, we show histograms of these conductance data and see that there is no overlap in the conductance histograms from traces that are selected for noise measurements and the experimental noise floor. This indicates that a rupture followed by a reattachment process does not happen within 100 ms timescale. We therefore conclude that the measured noise does not result from events involving the Au-S bond rupturing and reforming.

CHAPTER 4. FLICKER NOISE CHARACTERISTICS OF SINGLE-MOLECULE JUNCTIONS

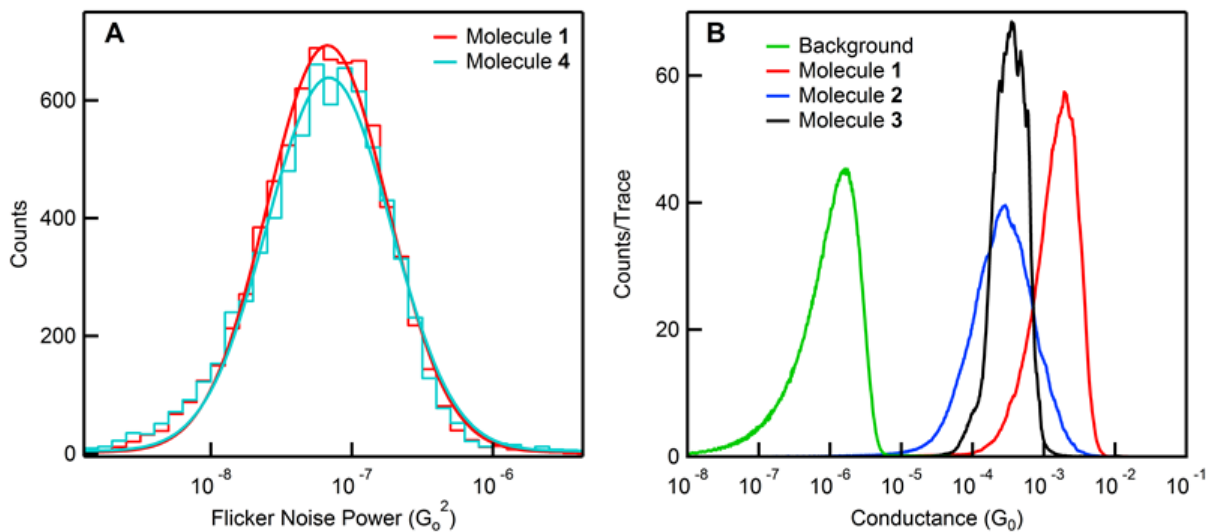


Figure 4.12: (A) Histograms of the flicker noise power for molecule 1 and 4. (B) Conductance histograms compiled from the constant displacement sections of the traces that show molecular junctions at the beginning and at the end of the constant displacement section for three molecular systems (red, blue, black) and the conductance histogram of the experimental background (green), which does not overlap the other histograms.

Chapter 5

Evidence for Optically Induced Charge Transfer Through Single-Molecule Junctions

5.1 Preface

This chapter is based on the manuscript entitled *Evidence for Optically Induced Charge Transfer Through Single-Molecule Junctions* by Olgun Adak, Diego Scarabelli and Latha Venkataraman.

5.2 Abstract

We investigate light induced charge transport through single-molecule junctions, tunnel junctions and gold point-contacts. We demonstrate that lock-in photocurrent measurements in these nano-junctions give rise to spurious photocurrents resulting from laser induced thermal expansion. We develop an experimental technique that distinguishes

CHAPTER 5. EVIDENCE FOR OPTICALLY INDUCED CHARGE TRANSFER THROUGH SINGLE-MOLECULE JUNCTIONS

between the thermal expansion induced photocurrents and the optical currents that arise from photon absorption and emission of electrons during charge transport. By using this technique, we provide evidence for photon absorption during charge transport through 4,4'-bipyridine single-molecule junctions and further demonstrate that the electric field enhancement factor in this system is around 20 which is good agreement with the tip enhanced Raman spectroscopy and field emission measurements.

5.3 Introduction

The ability to control charge transport across single-molecule devices using light would provide a fundamental break-through in our ability to achieve device functionality at the nanometer scale. [71] Theoretical studies have long predicted that conductance of a molecule could be enhanced upon light illumination in the optical or the near-infrared range of the spectrum. [34], [170], [171] The photon flux necessary to observe these predicted effects is often much larger than what can be achieved experimentally. However, with the advances in the field of photonics, electromagnetic fields can be concentrated into small nano-cavities by exploiting the plasmonic properties of the noble metals making it potentially feasible to observe photo-induced charge transport through single-molecule junctions. [172]–[177] The first steps towards achieving the optical control of charge transport through single-molecule junctions were the observation of photocurrents in tunnel junctions and metallic point-contacts. [178]–[184] More recently, light induced charge transport through single-molecule junctions has been realized by creating enhanced local electric fields by exploiting the plasmonic properties of the electrodes. [185], [186] However, the thermal effects of the incident electromagnetic radiation have often not been accounted for in these experiments, leaving some doubts on the validity of the conclusions presented. [185], [186]

CHAPTER 5. EVIDENCE FOR OPTICALLY INDUCED CHARGE TRANSFER THROUGH SINGLE-MOLECULE JUNCTIONS

Here, we investigate the photocurrent characteristics of single-molecule junctions, tunnel junctions and gold point-contacts with the aim of gaining a deeper insight into the mechanisms that give rise to light induced charge transport. We find that a large component of the observed photocurrents in all systems results primarily from thermal expansion induced by the light absorption in the electrodes. We further develop a technique that differentiates between the optical currents and the thermally induced photocurrents due to laser heating. Using this technique, we show that the light induced AC voltage in single-molecule junctions is small, and consistent with a plasmonic electric field enhancement factor around 20.

Electron transport through molecular junctions, tunnel junctions and gold point-contacts can be understood by a transmission model in which an electron propagating towards the junction has an energy dependent transmission probability. [5], [6], [187] In this model, the effect of the light illumination on the junction conductance is two-fold: When light is incident onto a single-molecule junction, a tunnel junction or a gold point-contact, it induces optical transitions in the electrodes. This leads to the smearing of the electron Fermi distribution due to electronic heating as well the creation of a hot electron population above the Fermi level. [27] When the electronic energy distribution is altered, the junction conductance is modified if the electron transmission probability depends on energy. Additionally, depending on the details of the electrode structure, light may launch surface electron density waves which propagate on the metal surface. [177], [188] These electron density waves or surface plasmons can concentrate light into sub-nanometer volumes and enhance the local electromagnetic fields near the junction. [172]–[177] Unlike the hot electron generation due to light absorption in the leads, in this case, an electric field oscillating at the light frequency builds across the junction. Electrons transmitted across the junction may couple to this field, undergoing an optical transition, which in

*CHAPTER 5. EVIDENCE FOR OPTICALLY INDUCED CHARGE TRANSFER
THROUGH SINGLE-MOLECULE JUNCTIONS*

turn modifies the electron transmission probability. [170], [171]

In the standard electron transport model, in the presence of an electromagnetic field when an electron can absorb or emit photons during charge transport, the current through the junction is given by [171]

$$I(V) = \frac{G_0}{e} \sum_{n=-\infty}^{\infty} \int_{-\infty}^{\infty} J_n^2 \left(\frac{eV_{opt}}{\hbar\omega} \right) T(E + n\hbar\omega) [f_L(E + eV/2) - f_R(E - eV/2)] dE \quad (5.1)$$

where V_{opt} is the AC voltage generated across the junction by the light, ω is the light frequency, J_n denotes the n^{th} order the Bessel function of the first kind which gives the transition amplitude for emitting and absorbing n photons, V is the applied bias voltage, f_L and f_R are the Fermi distributions of the left and right electrodes, $T(E)$ is the transmission function and G_0 is the conductance quantum. We note the effect of hot electron generation in the electrodes can simply be taken into account by replacing the equilibrium Fermi distributions with steady state non-equilibrium ones. However, due to an efficient electron-electron and electron-phonon coupling in metals, the effect of changes to the equilibrium Fermi distribution at the micro-second time scales, relevant to experiments, can be neglected as detailed in Section 5.6.1. [27]–[32]

When $eV_{opt} \ll \hbar\omega$, the multiple photon absorption and emission processes ($|n| > 1$) can be neglected. Approximating to a second order in $eV_{opt}/\hbar\omega$, Eq. 5.1 can be written as

$$I(V) = I_D[T(E)] + \frac{1}{4} \left(\frac{eV_{opt}}{\hbar\omega} \right)^2 (I_D[T(E + \hbar\omega)] + I_D[T(E - \hbar\omega)] - 2I_D[T(E)]) \quad (5.2)$$

where I_D denotes the DC current without light.

The second term on the right hand side of Eq. 5.2 is the optical current which can be thought of as the dark DC current determined by shifting $T(E)$ by $\pm\hbar\omega$. We note that

*CHAPTER 5. EVIDENCE FOR OPTICALLY INDUCED CHARGE TRANSFER
THROUGH SINGLE-MOLECULE JUNCTIONS*

a form similar to Eq. 5.2 is used in literature where the applied DC voltage is shifted by $\hbar\omega$, instead of considering a shifted transmission function; however, such an expression must carefully consider the effect of the optical voltage on both electrodes, not just one, as discussed in detail in the work of Platero et.al. [171] For a molecular junction, $T(E)$ can often be described using a Lorentzian form with only two parameters: the alignment of the dominant molecular orbital relative to the electrode Fermi level (E_{level}) and the broadening of this orbital due to hybridization with the electrodes (Γ). [79], [80]

$$T(E) = \frac{(\Gamma/2)^2}{(E - E_{level})^2 + (\Gamma/2)^2} \quad (5.3)$$

Referring to Eq. 5.2 and Eq. 5.3 above, we see that the photocurrent is maximal when the photon energy is in resonance with a transmission peak, i.e. when $\hbar\omega = E_{level}$. With this introduction to the mechanism of photo-induced charge transport in nanoscale junctions, we turn to our experimental methods and results.

We use a scanning tunneling microscope-based break-junction set-up with optical imaging capability to form gold point-contacts, tunnel junctions and single-molecule junctions (see Figure 5.1A for schematic representation of the studied systems, and see Section 5.6.2 and Figure 5.5 for the experimental details). [36], [37] The photocurrent measurements are performed using a lock-in type measurement technique in which the light intensity is being modulated by driving the laser diode with an AC current in addition to a DC current. At the same time, the current through the junction is measured and recorded over a bandwidth of 0-50 kHz. In order to obtain the photocurrent, the current at the light modulation frequency is extracted from the frequency domain representation of the junction current obtained by using the Fourier transform (see Figure 5.1B).

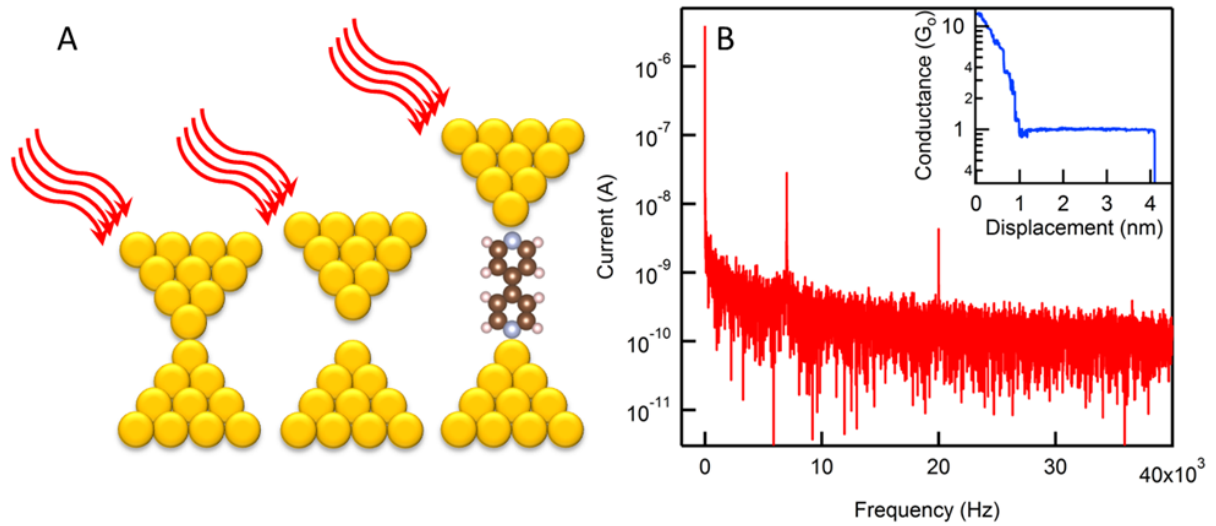


Figure 5.1: (A) Schematic representation of the systems studied. (B) The frequency domain representation of the current through a gold point-contact under 658 nm light with a peak intensity of 300 kW/cm^2 modulated at 20 kHz and a tip displacement modulation of 0.1 \AA at 7 kHz. Inset: The conductance trace for the gold point-contact.

5.4 Results and Discussion

We first perform photocurrent measurements in tunnel junctions with conductance ranging from 10^{-5} to $10^{-1} G_0$ and gold point-contacts with conductance ranging from 1 to $25 G_0$ under 658 nm light with a peak intensity of 300 kW/cm^2 modulated at 20 kHz. In Figure 5.2, we show the two-dimensional histograms of the photocurrent against the junction conductance for over 30000 different tunnel junctions and 60000 different gold point-contacts. We observe that the photocurrent scales linearly with the junction conductance in tunnel junctions. In gold point-contacts, there is a sub-linear relation and a sharp decrease in the photocurrent at the integer multiples of G_0 . We argue that the observed behavior is consistent with a light induced thermal expansion effect rather than

*CHAPTER 5. EVIDENCE FOR OPTICALLY INDUCED CHARGE TRANSFER
THROUGH SINGLE-MOLECULE JUNCTIONS*

an optical rectification or hot electron transport. [189], [190] As the electrodes absorb light, their temperature increases slightly. Since the light intensity is being modulated, the electrode temperature is also modulated at the same frequency. This, in turn, modulates the separation between the electrodes, altering the conductance and the current measured across the gold point-contacts or the tunnel junctions at the light modulation frequency. To demonstrate that the primary effect of modulating the light intensity in these experiments is a thermal expansion induced current, we imitate the thermal expansion by incorporating a small oscillatory mechanical motion (0.1 \AA amplitude) into one of the electrodes at a frequency different than the light modulation frequency (at 7 kHz in this case, as shown in Figure 5.1B). We measure, simultaneously, the current at 20 kHz (due to the light) and the current at 7kHz (due to the mechanical perturbation) which we denote 'mechanical current' for all junctions.

CHAPTER 5. EVIDENCE FOR OPTICALLY INDUCED CHARGE TRANSFER
THROUGH SINGLE-MOLECULE JUNCTIONS

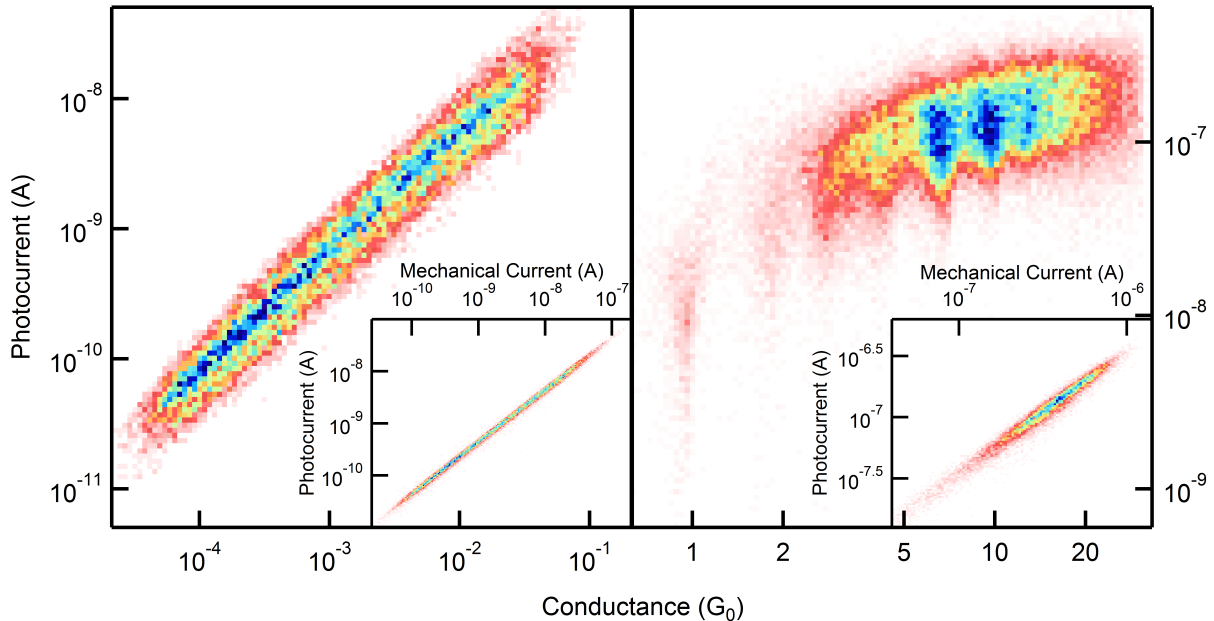


Figure 5.2: Two-dimensional histograms of the photocurrent (under 658 nm light with 300 kW/cm^2 peak intensity modulated at 20 kHz) against the junction conductance in (A) tunnel junctions and (B) gold point-contacts. Inset: Two-dimensional histograms of the photocurrent (under 658 nm light with 300 kW/cm^2 peak intensity modulated at 20 kHz) against the mechanical current (with a tip displacement modulation of 0.1 \AA at 7 kHz).

In Figure 5.2A and B insets, we show the two-dimensional histogram of the photocurrent against the mechanical current for over 30000 tunnel junctions and 60000 gold point contacts. The photocurrent correlates strongly with the mechanical current in both systems. This demonstrates that the observed photocurrents in tunnel junctions and gold point-contacts are in large part due to the thermal expansion of the electrodes. Any additional optically induced current should thus be distinguished from the thermal expansion effect of the light. We note that the correlations are not perfect because the mechanical modulation does not capture exactly the changes in the electrode separation caused by thermal expansion. We further do not find any qualitative difference when these exper-

CHAPTER 5. EVIDENCE FOR OPTICALLY INDUCED CHARGE TRANSFER THROUGH SINGLE-MOLECULE JUNCTIONS

iments are repeated using 405 nm and 908 nm light (see Section 5.6.3 and Figure 5.6). Importantly, in order to obtain the same photocurrent, the laser power at 405 nm has to be decreased by a factor of 15; while it has to be increased by a factor of about 3 with 980 nm light. These findings are consistent with the fact that gold absorption is much higher at 405 nm due to available inter-band transitions when compared with 658 nm and 980 nm. [191]

Having established that the photocurrents through tunnel junctions and gold point-contacts are primarily due to laser induced heating, we investigate light induced electron transport in molecular junctions where the transmission functions have sharp resonances due to discrete molecular orbital energy levels that are coupled to the electrodes. We focus on junctions formed with 4,4'-bipyridine (BP) as the charge transport in this system is dominated by the LUMO located approximately 1.1 eV away from Fermi level which is accessible in the near-infrared range of the electromagnetic spectrum, and the transmission functions are well-approximated by a single Lorentzian. [69]

We first perform photocurrent and mechanical current measurements on BP with a 0.5 V DC bias voltage under 980 nm light with 150 kW/cm^2 peak intensity. In Figure 5.3, we show the two-dimensional histogram of the photocurrent against the mechanical current for 6000 BP junctions. We observe that the effect of light is imitated by a mechanical modulation of the electrode separation similar to the case of tunnel junctions and gold point-contacts. We further note that the photocurrent and the mechanical current vary by an order of magnitude.

*CHAPTER 5. EVIDENCE FOR OPTICALLY INDUCED CHARGE TRANSFER
THROUGH SINGLE-MOLECULE JUNCTIONS*

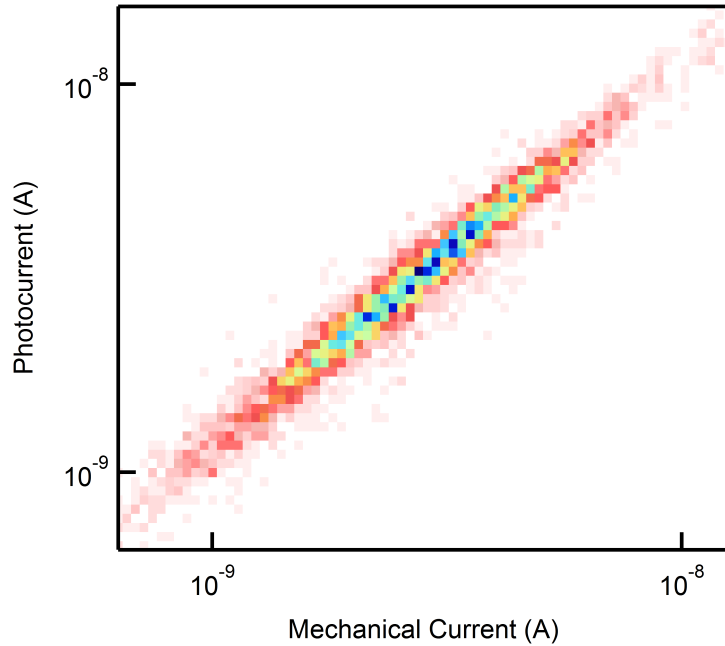


Figure 5.3: A two-dimensional histogram of the photocurrent against the mechanical current under 980 nm light with 150 kW/cm^2 peak intensity modulated at 15 kHz and with a tip displacement modulation of 1 Å at 10 kHz for BP single-molecule junctions.

According to Eq. 5.2, the optical current due to photon absorption and emission of electrons during charge transport has a quadratic dependence on the photovoltage which is proportional to the electric field between the electrodes and the electrode separation. In the STM geometry, the local electric field inside the cavity formed between the tip and the substrate is determined by the radius of curvature of the STM tip and the distance between the electrodes. [192] When the distance between the electrodes is much smaller than the radius of curvature of the STM tip, the local electric field depends weakly on the electrode separation. [192] Since the electrode separation of single-molecule junctions formed by BP is less than 10 Å [76] and STM tips used in this work are obtained by cutting a gold wire which should result in radius of curvatures much larger than a nanometer, we expect that the electric field between the electrodes does not increase appreciably

*CHAPTER 5. EVIDENCE FOR OPTICALLY INDUCED CHARGE TRANSFER
THROUGH SINGLE-MOLECULE JUNCTIONS*

upon decreasing the electrode separation. Therefore, one way to determine whether the photocurrent contains an optical current component is to see if the photocurrent gets smaller when the electrodes are pushed closer for a single-molecule junction which should decrease the photovoltage across the junction. The major challenge with this approach is that the molecular orbital coupling, thus the junction conductance, is highly sensitive to electrode separation; this strongly affects the thermal expansion current. As a result, one cannot directly compare the photocurrents before and after pushing the electrodes to see if there is an optical component. To overcome this, we define a ratio, R , as:

$$R = \frac{I_P}{I_M} = \frac{I_T + I_O}{I_M} = \alpha + \frac{I_O}{I_M} \quad (5.4)$$

Here, I_P is the current at the light modulation frequency, which is a sum of a thermal expansion current I_T and an optical current I_O . I_M is the mechanical current and α is the ratio between I_T and I_M .

According to Eq. 5.4, R should be smaller for junctions with a smaller electrode separation, first due to a smaller photovoltage, and second due to a larger I_M resulting from a larger molecular orbital coupling, as α does not depend on the junction conductance (see Section 5.6.4, Section 5.6.5, Figure 5.7, Figure 5.8 and Figure 5.9). Therefore, comparing R in junctions with two different electrode separations, one can obtain evidence for a non-zero I_O .

We employ this method to probe the optical currents in BP single-molecule junctions under 980 nm light with 150 kW/cm^2 peak intensity. We first measure I_P and I_M for a single-molecule junction, then decrease the electrode separation about 4 Å, reducing the average electrode separation by about half [76], and then measure I_P and I_M again. We obtain two R values for each junction, R_B (before pushing the electrodes) and R_A (after pushing the electrodes). To see if R_A is systematically smaller than R_B , as one would

CHAPTER 5. EVIDENCE FOR OPTICALLY INDUCED CHARGE TRANSFER THROUGH SINGLE-MOLECULE JUNCTIONS

expect if I_O is finite, we make a histogram of R_A/R_B . We further repeat this measurement with 658 nm light where we do not expect to see a significant optical current, as no molecular orbital for a BP junction is in resonance with 658 nm light.

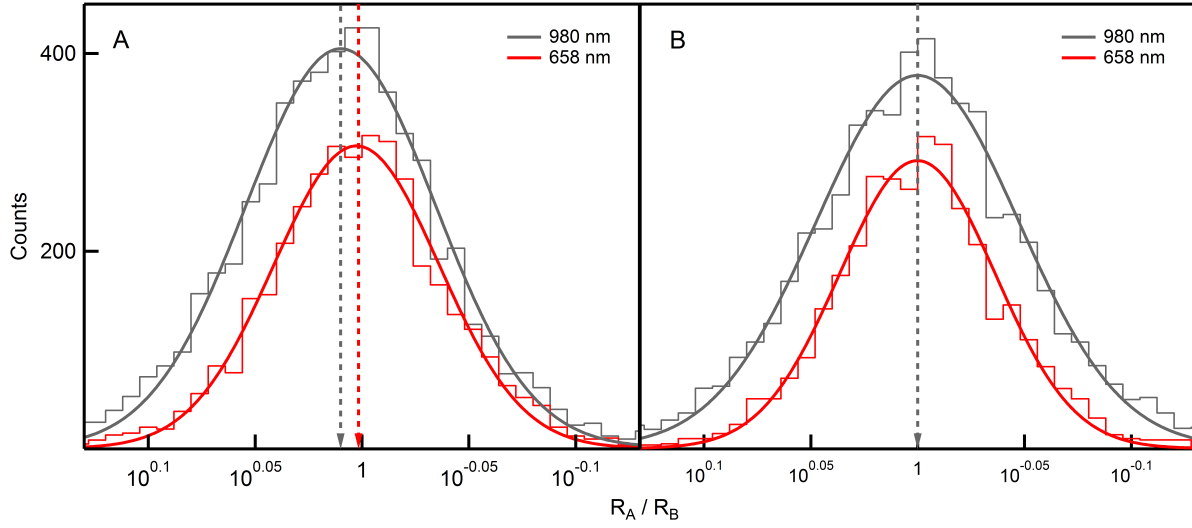


Figure 5.4: (A) Histograms of R_A/R_B under (red) 658 nm light with 90 kW/cm^2 peak intensity modulated at 15 kHz and (gray) 980 nm light with 150 kW/cm^2 peak intensity modulated at 15 kHz for BP single-molecule junctions with a tip displacement modulation of 1 Å at 10 kHz. (B) The simulated histogram with a V_{opt} of 14 mV, a 4 Å decrease in the electrode separation and assuming an initial electrode separation of 8 Å under (red) 658 nm light and (gray) 980 nm light.

In Figure 5.4A, we show the histogram of R_A/R_B obtained with a 0.5 V DC bias voltage under 980 nm (1.27 eV) light for 6000 BP single-molecule junctions and under 658 nm (1.88 eV) light for 3800 BP single-molecule junctions. We see that I_P/I_M exhibits a systematic decrease as the electrodes are pushed together with 980 nm light, while remains the same with 658 nm light. The fact that the histogram is centered at 1 with 658 nm indicates that on average, no optical current is present at this wavelength which is

CHAPTER 5. EVIDENCE FOR OPTICALLY INDUCED CHARGE TRANSFER THROUGH SINGLE-MOLECULE JUNCTIONS

consistent with the fact that there is no molecular resonance in the transmission function of BP around 1.88 eV. [69] However, the systematic decrease in I_P/I_M when the electrodes are pushed together with 980 nm light points to an optical current that is sensitive to the electrode separation. We further note that, on average, the optical current that leads to the observed shift in the histogram with 980 nm light corresponds to only 1% of the measured photocurrent and 0.2% of the total DC current.

We then estimate the photovoltage that would lead to the observed offset in the histogram in Figure 5.4A. According to Eq. 5.2, in order to calculate the optical current for a given V_{opt} , one needs to know the transmission function. However, the transmission function of BP is well-approximated by a single Lorentzian function (Eq. 5.3) where E_{level} and Γ can be determined experimentally using an AC spectroscopy technique which involves measuring the differential conductance and the non-linearity in conductance for a single-molecule junction; and fitting both to a single Lorentzian function. [69]

Therefore, when we perform photocurrent measurements, we simultaneously determine E_{level} and Γ for each single-molecule junction. We calculate the optical current using Eq. 5.2 for a given V_{opt} for each junction before and after pushing the electrodes. We subtract the calculated optical current from the measured photocurrent and remake the histogram presented in Figure 5.4A. We first note that E_{level} is distributed around 1 eV before and after pushing the electrodes closer, while the average Γ increases from 45 meV to 90 meV after pushing the electrodes closer (see Figure 5.8). In Figure 5.4B, we present the simulated histograms with a 14 mV V_{opt} assuming an initial electrode separation of 8 Å; this is the average value for the initial electrode separation of BP single-molecule junctions which ranges between 5 Å and 10 Å. [76] We can see that the optical currents arising from a 14 mV V_{opt} are enough to induce the observed change in I_P/I_M with 980 nm; while if we perform the same simulation for the 658 nm measurement, no shift is induced

*CHAPTER 5. EVIDENCE FOR OPTICALLY INDUCED CHARGE TRANSFER
THROUGH SINGLE-MOLECULE JUNCTIONS*

in the histogram. This V_{opt} value corresponds to an average electric field enhancement factor of 23 with an initial electrode separation of 8 Å and an incident electric field of 7.5×10^5 V/m which corresponds to a $150\text{ }kW/cm^2$ light intensity. This electric field enhancement factor is in very good agreement with values obtained from tip enhanced Raman spectroscopy [193] and field emission measurements. [194]–[196]

5.5 Conclusion

In conclusion, we investigated the possibility of controlling charge transport through single-molecule junctions using light. To this end, we first studied the mechanism for photocurrent generation in single-molecule junctions, tunnel junctions and gold point-contacts. We find that laser induced thermal expansion that results from a modulation of the light intensity, necessary for lock-in type measurements, is responsible for a large fraction of the photocurrents measured. Next, we developed a method that distinguishes between the thermal expansion induced photocurrents and the optical currents. By using this method, we provided evidence for optical currents in single-molecule junctions formed by BP. The photovoltage responsible for the observed optical currents is estimated to be 14 mV. This corresponds to a plasmonic electric field enhancement factor around 20 which is in very good agreement with values obtained from tip enhanced Raman spectroscopy and field emission measurements.

5.6 Supporting Information

5.6.1 Hot Electron Transport

The effect of light absorption in the electrodes is the smearing of the equilibrium electron Fermi distribution and the creation of a hot electron population above the Fermi level. [27] We do not expect any differential electronic heating across the junction as the gold absorbance and the local electromagnetic field strength determine the electronic heating, therefore we do not expect any thermoelectric current in the studied systems.

A hot electron population near the photon energy relative to the Fermi level leads to photocurrents due to an enhanced transmission probability. One important property of the relaxation mechanism for the electrons in Au is that the relaxation rate for the electrons increases quadratically with the increasing energy relative to the Fermi level. [27], [30] As a consequence, at the steady state (> 1 ps), hot electrons exist close to the Fermi level [27] as high energy electrons rapidly thermalize with the electron bath. Thus, we do not expect a significant hot electron current due to transmission near the resonance.

Here we point that an electron that absorbs a photon during the transport or before the transport in the electrodes has the same tunneling probability. The difference between these two processes is that; in the former, the relaxation of the hot electron occurs only after the transmission and any electric field enhancement in the junction leads to a larger photon absorption probability. Hence, we expect the former process to be the dominant one in our systems.

5.6.2 Experimental Set-up

A block diagram of the home-build scanning tunneling microscope-based break-junction set-up with optical imaging capability is shown in Figure 5.5. A voltage is applied to the

*CHAPTER 5. EVIDENCE FOR OPTICALLY INDUCED CHARGE TRANSFER
THROUGH SINGLE-MOLECULE JUNCTIONS*

junction using a digital to analog converter (NI PXI-4461), while the current through the junction is converted to voltage using a transimpedance amplifier (Femto DLPCA-200). The voltage output of the transimpedance amplifier and the voltage across the junction are recorded at a sampling rate of 100 kS/s using A/D inputs on the NI PXI-4461. The piezoactuator used for controlling the electrode separation is driven with the second analog voltage output of NI PXI-4461.

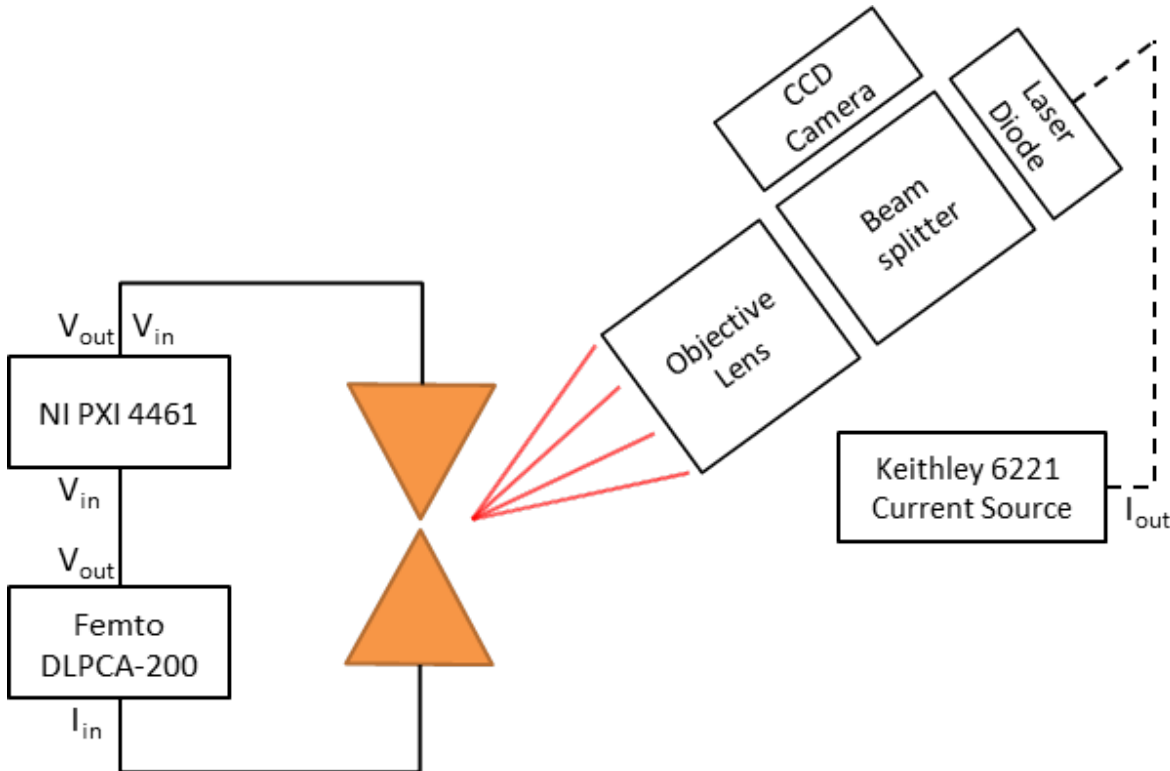


Figure 5.5: Block diagram of measurement set-up.

The optical microscope consists of an infinity corrected objective lens (Mitutoyo NIR $\times 50$ with a numerical aperture of 0.42), a beam splitter, a CCD camera, a laser diode and a laser diode driver (Keithley 6221). The objective lens makes an angle of 40° with the normal of the substrate surface. The CCD camera is used to align the laser spot on the junction. Light is polarized vertically in all experiments. The laser diode is placed inside

*CHAPTER 5. EVIDENCE FOR OPTICALLY INDUCED CHARGE TRANSFER
THROUGH SINGLE-MOLECULE JUNCTIONS*

a Faraday cage in order to avoid any electronic coupling to the circuit, while the entire setup is placed inside another Faraday cage to shield from any environmental noise.

5.6.3 Wavelength Dependence of Photocurrent in Gold Point-Contacts and Tunnel Junctions

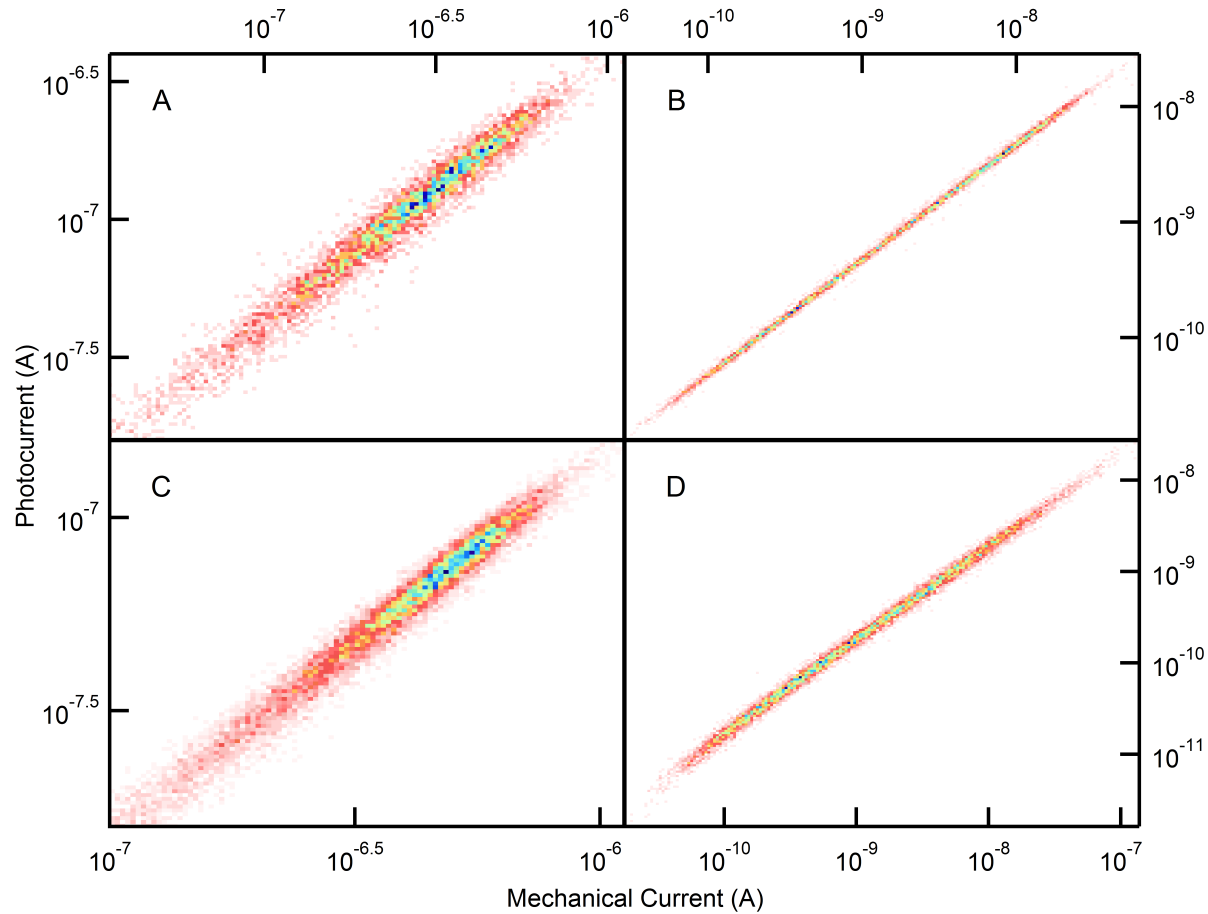


Figure 5.6: Two-dimensional histograms of the photocurrent against the mechanical current in gold point-contacts (A) and tunnel junctions (B) under 405 nm light with 20 kW/cm² peak intensity; and in gold point-contacts (C) and tunnel junctions (D) under 980 nm light with 250 kW/cm² peak intensity.

CHAPTER 5. EVIDENCE FOR OPTICALLY INDUCED CHARGE TRANSFER THROUGH SINGLE-MOLECULE JUNCTIONS

We repeat the photocurrent measurements in gold point-contacts and tunnel junctions under 405 nm light with 20 kW/cm^2 peak intensity and 980 nm light with 250 kW/cm^2 peak intensity, respectively. Similar to 658 nm, the mechanical modulation imitates the light effect at these wavelengths (see Figure 5.6).

5.6.4 Dependence of the Ratio between Photocurrent and Mechanical Current on Junction Conductance

In Figure 5.7, we show a two-dimensional histogram of the ratio between the photocurrent (I_P) and the mechanical current (I_M) against the junction conductance for 6000 BP single-molecule junctions for the data set presented in the manuscript. We see that this ratio is not correlated with the junction conductance, which lets us probe the optical currents in the measured photocurrent by pushing the electrodes closer.

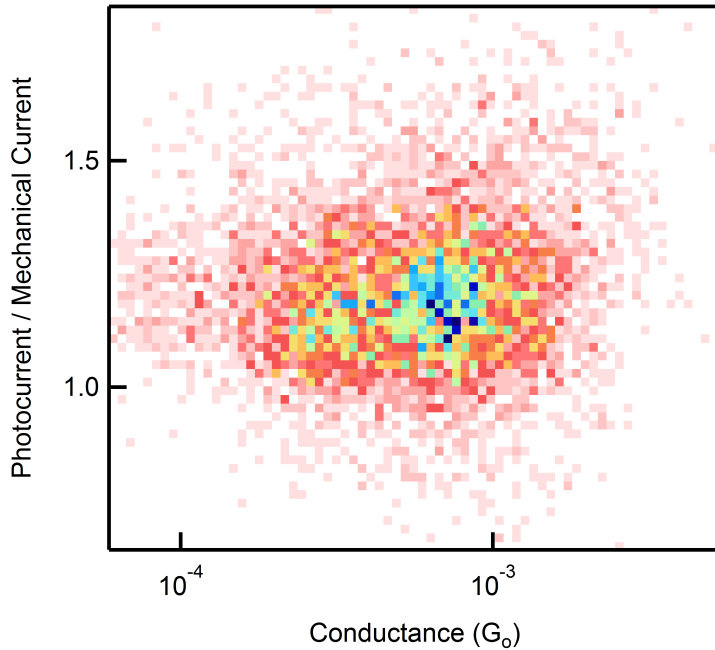


Figure 5.7: A two-dimensional histogram of junction conductance against I_P/I_M under 980 nm light for BP single-molecule junctions

5.6.5 Effect of Reduction in Coupling on Optical Current

The ratio (R) between the photocurrent (I_P) and the mechanical current (I_M) can be written as $(I_T + I_O)/I_M$, where I_T is the thermal expansion current and I_O is the optical current. I_T and I_M are linear with the DC current to the first order as they primarily appear at the light intensity modulation frequency and the tip displacement modulation frequency, respectively. Thus,

$$R = \frac{\alpha_T I_{DC} + I_O}{\alpha_M I_{DC}} \quad (5.5)$$

where α_T and α_M are the proportionality constants for the thermal expansion current and the mechanical current respectively and I_{DC} is the DC current through the junction.

CHAPTER 5. EVIDENCE FOR OPTICALLY INDUCED CHARGE TRANSFER THROUGH SINGLE-MOLECULE JUNCTIONS

Eq. 5.5 can be written as

$$R = \beta + \frac{I_O}{\alpha_M I_{DC}} \quad (5.6)$$

where β is α_T / α_M .

The most important effect of a reduction in the electrode separation is a reduction in V_{opt} and I_O . However, the second important effect is an increase in the molecular orbital coupling (Γ) which increases both I_O and I_{DC} through an increased Γ (see Figure 5.8).

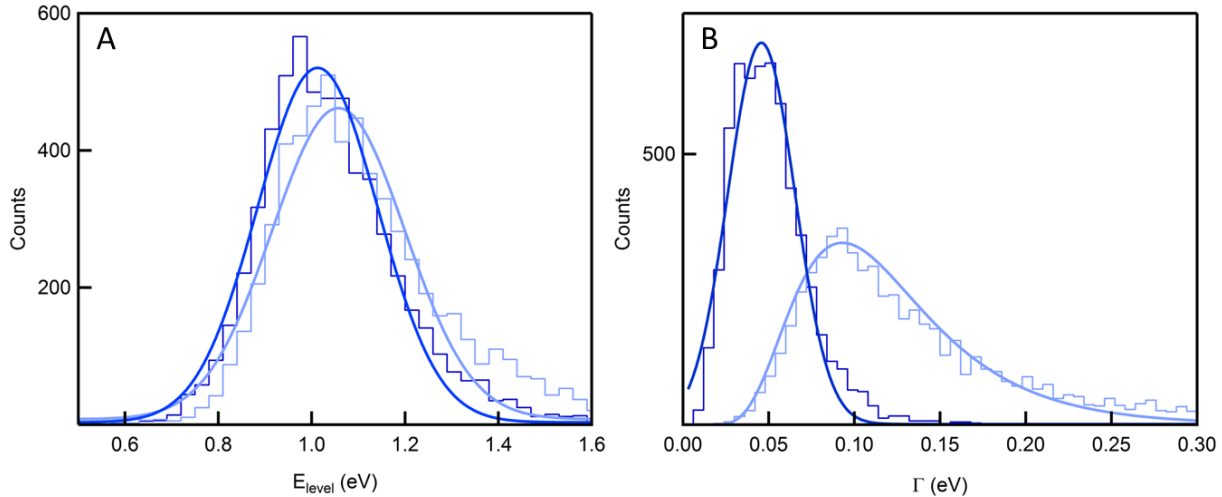


Figure 5.8: The estimated E_{level} and Γ before (dark blue) and after (light blue) pushing the electrodes by 4 Å in BP single-molecule junctions under 980 nm light for the data set presented in the manuscript.

To see how I_O/I_{DC} changes upon increasing Γ , we take a representative BP junction with a single Lorentzian transmission function and calculate I_O/I_{DC} as a function of Γ under a 0.5 V DC bias voltage with a photon energy of 1.27 eV, a V_{opt} of 14 mV and an E_{level} of 1.0 eV. We keep E_{level} the same as it increases negligibly upon pushing (~ 40 mV on average). As shown in Figure 5.9, I_O/I_{DC} decreases monotonically as Γ increases

*CHAPTER 5. EVIDENCE FOR OPTICALLY INDUCED CHARGE TRANSFER
THROUGH SINGLE-MOLECULE JUNCTIONS*

from 10 meV to 250 meV. Therefore, decreasing the electrode separation decreases I_P/I_M through a decrease in V_{opt} and an increase in Γ .

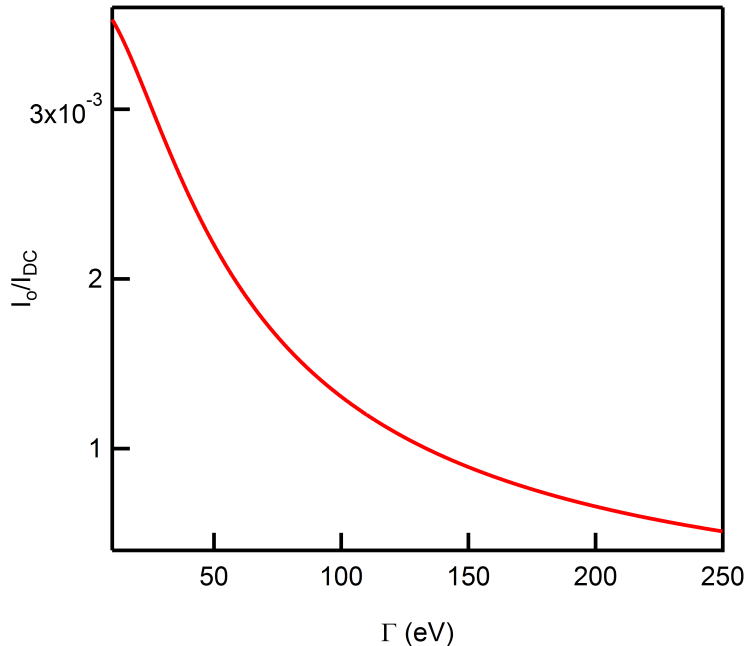


Figure 5.9: I_O/I_{DC} as a function of Γ for a representative BP junction with a 0.5 V DC bias voltage, a photon energy of 1.27 eV, a photovoltage of 14 mV and an E_{level} of 1.0 eV

Chapter 6

Conclusion and Outlook

6.1 Conclusion

In this thesis, we studied the effects of the electronic and the mechanical properties of electrodes on charge transport across hybrid interfaces containing organic constituents, and investigated the optical control of charge transport dynamics of a single-molecule junction using electromagnetic radiation. While studying these problems, we noticed that commonly used experimental techniques in the field were inadequate for investigating the rich physics present in these nanoscale systems. Therefore, a substantial portion of the effort was devoted to developing robust experimental techniques, capable of inferring unobservable physical parameters or phenomena in nanoscale junctions.

We first studied charge transport through pyridine-based single-molecule junctions formed with Ag and Au electrodes. We presented a new experimental technique that determines the level alignment and the molecular orbital coupling strength in single-molecule junctions. Unlike measurements of conductance and thermopower that allow one to obtain these transport parameters, our method can be employed not only in an STM-BJ set-up, but also in a mechanically controlled break-junction or an electromigrated break-

CHAPTER 6. CONCLUSION AND OUTLOOK

junction set-up. Using this technique, we showed that pyridine-linked molecules couple poorly to Ag electrodes when compared to Au electrodes. Using density functional theory calculations, we found that this is due to an enhanced density of d-states near the Fermi level as a consequence of relativistic effects.

We then investigated the interfacial charge transport from 4,4'-bipyridine to metallic (Au), semimetallic (expitaxial graphene), and semiconductor (graphene nanoribbon) surfaces using X-ray photoemission-based spectroscopy techniques. We found that the charge transfer time increases with the decreasing metallic character in these systems. We attributed this trend to a reduction in the electronic coupling between the molecule and the surface due to a reduction in the density of electronic states as the metallic character of the substrate decreases. Furthermore, we provided evidence for ultrafast electron phase decoherence via an interaction with the substrate in these systems.

We further demonstrated that flicker noise in single-molecule junctions is a result of the switching of gold atoms between metastable sites in the electrodes. This switching is due to the thermal energy, which continuously changes the electronic coupling of the molecule to the electrodes. We further showed that flicker noise can be used to distinguish between through-space and through-bond charge transfer at metal-organic interfaces. Moreover, this work shows that flicker noise in single-molecule junctions can be suppressed by decreasing the junction temperature.

Finally, we investigated the possibility of controlling the charge transport through single-molecule junctions using electromagnetic radiation. To this end, we performed photocurrent measurements on single-molecule junctions, tunnel junctions and gold point-contacts. We first demonstrated that in lock-in type measurements, photocurrents arise from laser induced thermal expansion of the electrodes. By using a new experimental technique that differentiates between the thermal expansion currents and the optical cur-

CHAPTER 6. CONCLUSION AND OUTLOOK

rents; we further showed that electron-photon interaction during charge transport gives rise to optical currents in single-molecule junctions. This is achieved by creating enhanced local electric fields near the junction by exploiting the plasmonic properties of the gold electrodes. The plasmonic electric field enhancement factor in our experiments is estimated to be around 20; this is good agreement with the values inferred from tip enhanced Raman spectroscopy measurements and field emission measurements.

6.2 Outlook

In this thesis, we gained a substantial understanding of the interplay between the transport characteristics and the electrode properties of organic devices. However, there are still many fundamental questions that need to be answered in order to have a complete picture of quantum transport at nanoscale. For example, we do not know the exact role of local physical phenomena such as screening, bond formation, charge donation and the Stark effect in determining the level alignment at interfaces. We know that the interaction between these phenomena and level alignment is very subtle and understanding the interplay between these and other effects would be very valuable for researchers aiming to achieve functional organic electronic devices.

Recently, researchers demonstrated that single-molecule junctions can be formed with carbon-based electrodes. [41] The noise characteristics of these systems are totally unknown and we suspect that single-molecules junctions formed with carbon-based electrodes would exhibit better noise characteristics; this would make them better candidates for commercial device components. Therefore extending the study of noise in single-molecule junctions to carbon-based electrodes would be interesting

Finally, we provided evidence for optical currents through single-molecule junctions due to electron-photon interaction. The observed currents are very small for using these

CHAPTER 6. CONCLUSION AND OUTLOOK

kind of devices in practical optical applications. However, we expect that using semiconductor electrodes, large hot electron currents could be driven through single-molecule junctions due to slow exciton recombination in semiconductors; this would open up the possibility of using organic materials as electrodes for harvesting hot electrons in solar cells.

6.3 Complete List of Work

1. O. Adak, D. Scarabelli, and L. Venkataraman, “Evidence for optically induced charge transfer through single-molecule junctions.,” In preparation
2. O. Adak, G. Kladnik, G. Bavdek, *et al.*, “Ultrafast bidirectional charge transport and electron decoherence at molecule/surfaces interfaces: A comparison of gold, graphene and graphene nanoribbon surfaces,” Submitted
3. O. Adak, R. Korytar, A. Y. Joe, *et al.*, “Impact of electrode density of states on transport through pyridine-linked single molecule junctions,” *Nano Letters*, vol. 15, no. 6, pp. 3716–3722, 2015
4. B. Capozzi, J. Xia, O. Adak, *et al.*, “Single-molecule diodes with high rectification ratios through environmental control,” *Nat Nano*, vol. 10, no. 6, pp. 522–527, 2015
5. O. Adak, E. Rosenthal, J. Meisner, *et al.*, “Flicker noise as a probe of electronic interaction at metal-single molecule interfaces,” *Nano Letters*, vol. 15, no. 6, pp. 4143–4149, 2015
6. A. Batra, D. Cvetko, G. Kladnik, *et al.*, “Probing the mechanism for graphene nanoribbon formation on gold surfaces through x-ray spectroscopy,” *Chemical Science*, vol. 5, p. 4419, 2014

CHAPTER 6. CONCLUSION AND OUTLOOK

7. Z.-F. Liu, S. Wei, H. Yoon, *et al.*, “Control of single-molecule junction conductance of porphyrins via a transition-metal center,” *Nano Letters*, vol. 14, no. 9, pp. 5365–5370, 2014

Bibliography

- [1] C. Joachim, J. K. Gimzewski, and A. Aviram, “Electronics using hybrid-molecular and mono-molecular devices,” *Nature*, vol. 408, no. 6812, pp. 541–548, 2000 (page 1).
- [2] A. Aviram and M. A. Ratner, “Molecular rectifiers,” *Chemical Physics Letters*, vol. 29, no. 2, pp. 277–283, 1974 (page 1).
- [3] A. H. Flood, J. F. Stoddart, D. W. Steuernnan, and J. R. Heath, “Whence molecular electronics?” *Science*, vol. 306, no. 5704, pp. 2055–2056, 2004 (page 1).
- [4] R. L. Carroll and C. B. Gorman, “The genesis of molecular electronics,” *Angewandte Chemie International Edition*, vol. 41, no. 23, pp. 4378–4400, 2002 (page 1).
- [5] A. Nitzan and M. A. Ratner, “Electron transport in molecular wire junctions,” *Science*, vol. 300, no. 5624, pp. 1384–1389, 2003 (pages 2, 17, 104).
- [6] M. Büttiker, Y. Imry, R. Landauer, and S. Pinhas, “Generalized many-channel conductance formula with application to small rings,” *Physical Review B*, vol. 31, no. 10, pp. 6207–6215, 1985 (pages 2, 3, 104).
- [7] S. M. Lindsay and M. A. Ratner, “Molecular transport junctions: Clearing mists,” *Advanced Materials*, vol. 19, no. 1, pp. 23–31, 2007 (page 2).
- [8] J. Reichert, R. Ochs, D. Beckmann, H. B. Weber, M. Mayor, and H. von Lohneysen, “Driving current through single organic molecules,” *Physical Review Letters*, vol. 88, no. 17, p. 176 804, 2002 (pages 2, 17).

BIBLIOGRAPHY

- [9] R. Huber, M. T. Gonzalez, S. Wu, M. Langer, S. Grunder, V. Horhoiu, M. Mayor, M. R. Bryce, C. S. Wang, R. Jitchati, C. Schonenberger, and M. Calame, “Electrical conductance of conjugated oligomers at the single molecule level,” *Journal of the American Chemical Society*, vol. 130, no. 3, pp. 1080–1084, 2008 (pages 2, 17, 20).
- [10] M. S. Hybertsen, L. Venkataraman, J. E. Klare, A. C. Whalley, M. L. Steigerwald, and C. Nuckolls, “Amine-linked single-molecule circuits: Systematic trends across molecular families,” *Journal of Physics: Condensed Matter*, vol. 20, no. 37, p. 374115, 2008 (pages 2, 17).
- [11] A. Mishchenko, L. A. Zotti, D. Vonlanthen, M. Burkle, F. Pauly, J. C. Cuevas, M. Mayor, and T. Wandlowski, “Single-molecule junctions based on nitrile-terminated biphenyls: A promising new anchoring group,” *Journal of the American Chemical Society*, vol. 133, no. 2, pp. 184–187, 2011 (pages 2, 17).
- [12] Y. Kim, T. J. Hellmuth, D. Sysoiev, F. Pauly, T. Pietsch, J. Wolf, A. Erbe, T. Huhn, U. Groth, U. E. Steiner, and E. Scheer, “Charge transport characteristics of diarylethene photoswitching single-molecule junctions,” *Nano Letters*, vol. 12, no. 7, pp. 3736–3742, 2012 (pages 2, 17).
- [13] J. Rauba, M. Strange, and K. Thygesen, “Quantum conductance of 4,4-bipyridine molecular junctions: Role of electrode work function and local d band,” *Physical Review B*, vol. 78, no. 16, p. 165116, 2008 (pages 2, 17, 26).
- [14] M. Kiguchi, S. Miura, T. Takahashi, K. Hara, M. Sawamura, and K. Murakoshi, “Conductance of single 1,4-benzenediamine molecule bridging between au and pt electrodes,” *Journal of Physical Chemistry C*, vol. 112, no. 35, pp. 13349–13352, 2008 (pages 2, 17).
- [15] C. H. Ko, M. J. Huang, M. D. Fu, and C. H. Chen, “Superior contact for single-molecule conductance: Electronic coupling of thiolate and isothiocyanate on pt, pd, and au,” *Journal of the American Chemical Society*, vol. 132, no. 2, pp. 756–764, 2010 (pages 2, 17).
- [16] B. Kim, S. H. Choi, X. Y. Zhu, and C. D. Frisbie, “Molecular tunnel junctions based on pi-conjugated oligoacene thiols and dithiols between ag, au, and pt contacts:

BIBLIOGRAPHY

- Effect of surface linking group and metal work function,” *Journal of the American Chemical Society*, vol. 133, no. 49, pp. 19 864–19 877, 2011 (pages 2, 17, 28).
- [17] T. Kim, H. Vazquez, M. S. Hybertsen, and L. Venkataraman, “Conductance of molecular junctions formed with silver electrodes,” *Nano Letters*, vol. 13, no. 7, pp. 3358–3364, 2013 (pages 2, 17, 28, 33).
 - [18] H. Ishii, K. Sugiyama, E. Ito, and K. Seki, “Energy level alignment and interfacial electronic structures at organic metal and organic organic interfaces,” *Advanced Materials*, vol. 11, no. 8, pp. 605–625, 1999 (pages 2, 17).
 - [19] G. Heimel, L. Romaner, J. L. Bredas, and E. Zojer, “Interface energetics and level alignment at covalent metal-molecule junctions: Pi-conjugated thiols on gold,” *Physical Review Letters*, vol. 96, no. 19, p. 196 806, 2006 (pages 2, 17).
 - [20] K. S. Thygesen and A. Rubio, “Renormalization of molecular quasiparticle levels at metal-molecule interfaces: Trends across binding regimes,” *Physical Review Letters*, vol. 102, no. 4, p. 046 802, 2009 (pages 2, 17).
 - [21] M. L. Perrin, C. J. O. Verzijl, C. A. Martin, A. J. Shaikh, R. Eelkema, J. H. Van Esch, J. M. Van Ruitenbeek, J. M. Thijssen, H. S. J. Van Der Zant, and D. D., “Large tunable image-charge effects in single-molecule junctions,” *Nature Nanotechnology*, vol. 8, no. 4, pp. 282–287, 2013 (pages 2, 17).
 - [22] P. Darancet, J. R. Widawsky, H. J. Choi, L. Venkataraman, and J. B. Neaton, “Quantitative current-voltage characteristics in molecular junctions from first principles,” *Nano Letters*, vol. 12, no. 12, pp. 6250–6254, 2012 (pages 2, 23).
 - [23] J. Park, A. N. Pasupathy, J. I. Goldsmith, C. Chang, Y. Yaish, J. R. Petta, M. Rinkoski, J. P. Sethna, H. D. Abruna, P. L. McEuen, and D. C. Ralph, “Coulomb blockade and the kondo effect in single-atom transistors,” *Nature*, vol. 417, no. 6890, pp. 722–725, 2002 (page 2).
 - [24] L. H. Yu and D. Natelson, “The kondo effect in c-60 single-molecule transistors,” *Nano Letters*, vol. 4, no. 1, pp. 79–83, 2004 (page 2).

BIBLIOGRAPHY

- [25] S. Datta, *Electronic Transport in Mesoscopic Systems*. Cambridge University Press, 1995 (page 3).
- [26] R. Landauer, “Electrical resistance of disordered one-dimensional lattices,” *Philosophical Magazine*, vol. 21, no. 172, pp. 863–867, 1970 (page 3).
- [27] C.-K. Sun, F. Vallée, L. H. Acioli, E. P. Ippen, and J. G. Fujimoto, “Femtosecond-tunable measurement of electron thermalization in gold,” *Physical Review B*, vol. 50, no. 20, pp. 15 337–15 348, 1994 (pages 4, 104, 105, 116).
- [28] P. B. Allen, “Theory of thermal relaxation of electrons in metals,” *Physical Review Letters*, vol. 59, no. 13, pp. 1460–1463, 1987 (pages 4, 105).
- [29] H. Kanter, “Slow-electron mean free paths in aluminum, silver, and gold,” *Physical Review B*, vol. 1, no. 2, pp. 522–536, 1970 (pages 4, 77, 105).
- [30] N. Del Fatti, C. Voisin, M. Achermann, S. Tzortzakis, D. Christofilos, and F. Vallée, “Nonequilibrium electron dynamics in noble metals,” *Phys. Rev. B*, vol. 61, pp. 16 956–16 966, 2000 (pages 4, 105, 116).
- [31] G. Della Valle, M. Conforti, S. Longhi, G. Cerullo, and D. Brida, “Real-time optical mapping of the dynamics of nonthermal electrons in thin gold films,” *Physical Review B*, vol. 86, no. 15, p. 155 139, 2012 (pages 4, 105).
- [32] L. D. Pietanza, G. Colonna, S. Longo, and M. Capitelli, “Non-equilibrium electron and phonon dynamics in metals under femtosecond laser pulses,” *The European Physical Journal D*, vol. 45, no. 2, pp. 369–389, 2007 (pages 4, 105).
- [33] P. K. Tien and J. P. Gordon, “Multiphoton process observed in the interaction of microwave fields with the tunneling between superconductor films,” *Physical Review*, vol. 129, no. 2, pp. 647–651, 1963 (page 4).
- [34] S. Kohler, S. Camalet, M. Strass, J. Lehmann, G.-L. Ingold, and P. Hänggi, “Charge transport through a molecule driven by a high-frequency field,” *Chemical Physics*, vol. 296, no. 2-3, pp. 243–249, 2004 (pages 4, 103).

BIBLIOGRAPHY

- [35] G. Q. Li, M. Schreiber, and U. Kleinekathofer, “Coherent laser control of the current through molecular junctions,” *EPL (Europhysics Letters)*, vol. 79, no. 2, p. 27006, 2007 (page 4).
- [36] B. Q. Xu and N. J. Tao, “Measurement of single-molecule resistance by repeated formation of molecular junctions,” *Science*, vol. 301, no. 5637, pp. 1221–1223, 2003 (pages 6, 7, 20, 70, 106).
- [37] L. Venkataraman, J. E. Klare, C. Nuckolls, M. S. Hybertsen, and M. L. Steigerwald, “Dependence of single-molecule junction conductance on molecular conformation,” *Nature*, vol. 442, no. 7105, pp. 904–907, 2006 (pages 6, 7, 70, 106).
- [38] P. Reddy, S. Y. Jang, R. A. Segalman, and A. Majumdar, “Thermoelectricity in molecular junctions,” *Science*, vol. 315, no. 5818, pp. 1568–1571, 2007 (page 6).
- [39] I. Diez-Perez, J. Hihath, Y. Lee, L. Yu, L. Adamska, M. A. Kozhushner, I. Oleynik, and N. Tao, “Rectification and stability of a single molecular diode with controlled orientation,” *Nature chemistry*, vol. 1, no. 8, pp. 635–41, 2009 (page 6).
- [40] J. G. Kushmerick, J. Lazorcik, C. H. Patterson, R. Shashidhar, D. S. Seferos, and G. C. Bazan, “Vibronic contributions to charge transport across molecular junctions,” *Nano Letters*, vol. 4, no. 4, pp. 639–642, 2004 (pages 6, 23).
- [41] T. Kim, Z. F. Liu, C. Lee, J. B. Neaton, and L. Venkataraman, “Charge transport and rectification in molecular junctions formed with carbon-based electrodes,” *Proc Natl Acad Sci U S A*, vol. 111, no. 30, pp. 10 928–32, 2014 (pages 6, 125).
- [42] M. T. Gonzalez, S. M. Wu, R. Huber, S. J. van der Molen, C. Schonenberger, and M. Calame, “Electrical conductance of molecular junctions by a robust statistical analysis,” *Nano Letters*, vol. 6, no. 10, pp. 2238–2242, 2006 (page 6).
- [43] J. R. Widawsky, W. Chen, H. Vazquez, T. Kim, R. Breslow, M. S. Hybertsen, and L. Venkataraman, “Length-dependent thermopower of highly conducting au-c bonded single molecule junctions,” *Nano Letters*, vol. 13, no. 6, pp. 2889–2894, 2013 (page 6).

BIBLIOGRAPHY

- [44] Z. Liu, S. Y. Ding, Z. B. Chen, X. Wang, J. H. Tian, J. R. Anema, X. S. Zhou, D. Y. Wu, B. W. Mao, X. Xu, B. Ren, and Z. Q. Tian, “Revealing the molecular structure of single-molecule junctions in different conductance states by fishing-mode tip-enhanced raman spectroscopy,” *Nature communications*, vol. 2, p. 305, 2011 (page 6).
- [45] R. Yamada, M. Noguchi, and H. Tada, “Magnetoresistance of single molecular junctions measured by a mechanically controllable break junction method,” *Applied Physics Letters*, vol. 98, no. 5, p. 053 110, 2011 (page 6).
- [46] N. Agrait, A. L. Yeyati, and J. M. van Ruitenbeek, “Quantum properties of atomic-sized conductors,” *Physics Reports*, vol. 377, no. 2-3, pp. 81–279, 2003 (pages 7, 17, 72).
- [47] Z. Gai, Y. He, H. Yu, and W. S. Yang, “Observation of conductance quantization of ballistic metallic point contacts at room temperature,” *Physical Review B*, vol. 53, no. 3, pp. 1042–1045, 1996 (page 7).
- [48] A. I. Yanson, G. R. Bollinger, H. E. van den Brom, N. Agrait, and J. M. van Ruitenbeek, “Formation and manipulation of a metallic wire of single gold atoms,” *Nature*, vol. 395, no. 6704, pp. 783–785, 1998 (page 7).
- [49] O. Karis, A. Nilsson, M. Weinelt, T. Wiell, C. Puglia, N. Wassdahl, N. Mårtensson, M. Samant, and J. Stöhr, “One-step and two-step description of deexcitation processes in weakly interacting systems,” *Physical Review Letters*, vol. 76, no. 8, pp. 1380–1383, 1996 (pages 8, 49).
- [50] M. P. Seah, “The quantitative analysis of surfaces by xps: A review,” *Surface and Interface Analysis*, vol. 2, no. 6, pp. 222–239, 1980 (page 8).
- [51] J. Stöhr, *NEXAFS Spectroscopy*. Heidelberg, 1992 (pages 8–10, 52, 55).
- [52] P. A. Brühwiler, O. Karis, and N. Mårtensson, “Charge-transfer dynamics studied using resonant core spectroscopies,” *Reviews of Modern Physics*, vol. 74, no. 3, pp. 703–740, 2002 (pages 8, 12, 49, 53, 62, 63).

BIBLIOGRAPHY

- [53] H. Luth, *Surfaces and Interfaces of Solid Materials*. Springer, 1995 (page 8).
- [54] J. Watts and J. Wolstenholme, *Surface Analysis by XPS and AES*. John Wiley & Sons Ltd, 2003 (page 8).
- [55] M. P. Seah, “A review of the analysis of surfaces and thin films by aes and xps,” *Vacuum*, vol. 34, no. 3-4, pp. 463–478, 1984 (page 8).
- [56] B. Johansson and N. Martensson, “Core-level binding-energy shifts for the metallic elements,” *Phys. Rev. B*, vol. 21, pp. 4427–4457, 1980 (page 8).
- [57] P. A. Brühwiler, A. J. Maxwell, C. Puglia, A. Nilsson, S. Andersson, and N. Mårtensson, “ π^* and σ^* excitons in c 1s absorption of graphite,” *Phys. Rev. Lett.*, vol. 74, pp. 614–617, 4 Jan. 1995 (page 9).
- [58] G. Hahner, “Near edge x-ray absorption fine structure spectroscopy as a tool to probe electronic and structural properties of thin organic films and liquids,” *Chemical Society Reviews*, vol. 35, no. 12, pp. 1244–1255, 2006 (page 9).
- [59] J. Stöhr and D. A. Outka, “Determination of molecular orientations on surfaces from the angular dependence of near-edge x-ray-absorption fine-structure spectra,” *Physical Review B*, vol. 36, no. 15, pp. 7891–7905, 1987 (page 10).
- [60] X. J. Wu, Q. X. Li, J. Huang, and J. L. Yang, “Nonequilibrium electronic transport of 4,4'-bipyridine molecular junction,” *Journal of Chemical Physics*, vol. 123, no. 18, p. 184712, 2005 (pages 10, 52).
- [61] A. J. Britton, A. Rienzo, J. N. O’Shea, and K. Schulte, “Charge transfer between the au(111) surface and adsorbed c60: Resonant photoemission and new core-hole decay channels,” *The Journal of Chemical Physics*, vol. 133, no. 9, p. 094705, 2010 (pages 11, 49, 53, 55).
- [62] A. Batra, G. Kladnik, H. Vazquez, J. S. Meisner, L. Floreano, C. Nuckolls, D. Cvetko, A. Morgante, and L. Venkataraman, “Quantifying through-space charge transfer dynamics in pi-coupled molecular systems,” *Nature Communications*, vol. 3, p. 1086, 2012 (pages 11, 49, 60).

BIBLIOGRAPHY

- [63] G. Kladnik, D. Cvetko, A. Batra, M. Dell'Angela, A. Cossaro, M. Kamenetska, L. Venkataraman, and A. Morgante, “Ultrafast charge transfer through noncovalent au-n interactions in molecular systems,” *Journal of Physical Chemistry C*, vol. 117, no. 32, pp. 16 477–16 482, 2013 (pages 11, 49, 60).
- [64] H. Hamoudi, S. Neppl, P. Kao, B. Schüpbach, P. Feulner, A. Terfort, D. Allara, and M. Zharnikov, “Orbital-dependent charge transfer dynamics in conjugated self-assembled monolayers,” *Physical Review Letters*, vol. 107, no. 2, p. 027801, 2011 (pages 11, 49).
- [65] J. Schnadt, P. A. Bruhwiler, L. Patthey, J. N. O’Shea, S. Sodergren, M. Odelius, R. Ahuja, O. Karis, M. Bassler, P. Persson, H. Siegbahn, S. Lunell, and N. Mårtensson, “Experimental evidence for sub-3-fs charge transfer from an aromatic adsorbate to a semiconductor,” *Nature*, vol. 418, no. 6898, pp. 620–623, 2002 (pages 11, 49).
- [66] O. Björneholm, S. Sundin, S. Svensson, R. R. T. Marinho, A. Naves de Brito, F. Gel'mukhanov, and H. Ågren, “Femtosecond dissociation of core-excited hcl monitored by frequency detuning,” *Physical Review Letters*, vol. 79, no. 17, pp. 3150–3153, 1997 (pages 11, 49).
- [67] M. Ohno, “Deexcitation processes in adsorbates,” *Physical Review B*, vol. 50, no. 4, pp. 2566–2575, 1994 (pages 11, 49).
- [68] M. Zharnikov, “Probing charge transfer dynamics in self-assembled monolayers by core hole clock approach,” *Journal of Electron Spectroscopy and Related Phenomena*, 2015 (pages 11, 49, 55).
- [69] O. Adak, R. Korytar, A. Y. Joe, F. Evers, and L. Venkataraman, “Impact of electrode density of states on transport through pyridine-linked single molecule junctions,” *Nano Letters*, vol. 15, no. 6, pp. 3716–3722, 2015 (pages 16, 110, 114, 126).
- [70] N. J. Tao, “Electron transport in molecular junctions,” *Nature Nanotechnology*, vol. 1, no. 3, pp. 173–181, 2006 (pages 17, 48).

BIBLIOGRAPHY

- [71] S. V. Aradhya and L. Venkataraman, “Single-molecule junctions beyond electronic transport,” *Nature Nanotechnology*, vol. 8, no. 6, pp. 399–410, 2013 (pages 17, 48, 103).
- [72] B. Ludoph and J. M. van Ruitenbeek, “Conductance fluctuations as a tool for investigating the quantum modes in atomic-size metallic contacts,” *Physical Review B*, vol. 61, no. 3, pp. 2273–2285, 2000 (pages 17, 68, 71).
- [73] Y. Kim, H. Song, F. Strigl, H. F. Pernau, T. Lee, and E. Scheer, “Conductance and vibrational states of single-molecule junctions controlled by mechanical stretching and material variation,” *Physical Review Letters*, vol. 106, no. 19, 2011 (pages 17, 22).
- [74] S. V. Aradhya, M. Frei, A. Halbritter, and L. Venkataraman, “Correlating structure, conductance, and mechanics of silver atomic-scale contacts,” *ACS Nano*, vol. 7, no. 4, pp. 3706–3712, 2013 (page 19).
- [75] M. Kamenetska, S. Y. Quek, A. C. Whalley, M. L. Steigerwald, H. J. Choi, S. G. Louie, C. Nuckolls, M. S. Hybertsen, J. B. Neaton, and L. Venkataraman, “Conductance and geometry of pyridine-linked single-molecule junctions,” *Journal of the American Chemical Society*, vol. 132, no. 19, pp. 6817–6821, 2010 (pages 20, 23).
- [76] S. Y. Quek, M. Kamenetska, M. L. Steigerwald, H. J. Choi, S. G. Louie, M. S. Hybertsen, J. B. Neaton, and L. Venkataraman, “Mechanically controlled binary conductance switching of a single-molecule junction,” *Nature Nanotechnology*, vol. 4, no. 4, pp. 230–234, 2009 (pages 20, 23, 25, 26, 111, 112, 114).
- [77] S. V. Aradhya, M. Frei, M. S. Hybertsen, and L. Venkataraman, “Van der waals interactions at metal/organic interfaces at the single-molecule level,” *Nature Materials*, vol. 11, no. 10, pp. 872–876, 2012 (page 20).
- [78] J. Visser, “On hamaker constants: A comparison between hamaker constants and lifshitz-van der waals constants,” *Advances in Colloid and Interface Science*, vol. 3, no. 4, pp. 331–363, 1972 (page 20).

BIBLIOGRAPHY

- [79] S. Datta, *Quantum Transport - Atom to Transistor*. Cambridge University Press, 2005 (pages 22, 106).
- [80] M. Paulsson and S. Datta, “Thermoelectric effect in molecular electronics,” *Physical Review B*, vol. 67, no. 24, p. 241403, 2003 (pages 22, 79, 95, 106).
- [81] E. H. Huisman, C. M. Guedon, B. J. van Wees, and S. J. van der Molen, “Interpretation of transition voltage spectroscopy,” *Nano Letters*, vol. 9, no. 11, pp. 3909–13, 2009 (page 22).
- [82] J. M. Thijssen and H. S. J. Van der Zant, “Charge transport and single-electron effects in nanoscale systems,” *Physica status solidi (b)*, vol. 245, no. 8, pp. 1455–1470, 2008 (page 22).
- [83] L. A. Zotti, T. Kirchner, J.-C. Cuevas, F. Pauly, T. Huhn, E. Scheer, and A. Erbe, “Revealing the role of anchoring groups in the electrical conduction through single-molecule junctions,” *Small*, vol. 6, no. 14, pp. 1529–1535, 2010 (pages 22, 42).
- [84] J. M. van Ruitenbeek, A. Alvarez, I. Pineyro, C. Grahmann, P. Joyez, M. H. Devoret, D. Esteve, and C. Urbina, “Adjustable nanofabricated atomic size contacts,” *Review of Scientific Instruments*, vol. 67, no. 1, pp. 108–111, 1996 (page 22).
- [85] H. Park, A. K. L. Lim, A. P. Alivisatos, J. Park, and P. L. McEuen, “Fabrication of metallic electrodes with nanometer separation by electromigration,” *Applied Physics Letters*, vol. 75, no. 2, pp. 301–303, 1999 (page 22).
- [86] D. R. Ward, G. D. Scott, Z. K. Keane, N. J. Halas, and D. Natelson, “Electronic and optical properties of electromigrated molecular junctions,” *Journal of Physics-Condensed Matter*, vol. 20, no. 37, p. 374118, 2008 (page 22).
- [87] T. Kim, P. Darancet, J. R. Widawsky, M. Kotiuga, S. Y. Quek, J. B. Neaton, and L. Venkataraman, “Determination of energy level alignment and coupling strength in 4,4'-bipyridine single-molecule junctions,” *Nano Lett*, vol. 14, no. 2, pp. 794–8, 2014 (page 23).

BIBLIOGRAPHY

- [88] A. Batra, J. Meisner, P. Darancet, Q. Chen, M. L. Steigerwald, C. Nuckolls, and L. Venkataraman, “Molecular diodes enabled by quantum interference,” *Faraday Discussions*, 2014 (pages 23, 78).
- [89] J. Hölzl and F. K. Schulte, “Work function of metals,” in *Solid Surface Physics*, J. Hölzl, F. Schulte, and H. Wagner, Eds., ser. Springer Tracts in Modern Physics. Springer Berlin Heidelberg, 1979, vol. 85, ch. 1, pp. 1–150 (pages 23, 24).
- [90] M. Galperin, M. A. Ratner, and A. Nitzan, “Inelastic electron tunneling spectroscopy in molecular junctions: Peaks and dips,” *The Journal of Chemical Physics*, vol. 121, no. 23, pp. 11 965–11 979, 2004 (page 23).
- [91] O. Jepsen, D. Glötzel, and A. R. Mackintosh, “Potentials, band structures, and fermi surfaces in the noble metals,” *Physical Review B*, vol. 23, no. 6, pp. 2684–2696, 1981 (page 26).
- [92] P. Pyykko and J. P. Desclaux, “Relativity and the periodic system of elements,” *Accounts of Chemical Research*, vol. 12, no. 8, pp. 276–281, 1979 (page 26).
- [93] M. Koentopp, K. Burke, and F. Evers, “Zero-bias molecular electronics: Exchange-correlation corrections to landauer’s formula,” *Physical Review B*, vol. 73, no. 12, p. 121 403, 2006 (page 27).
- [94] S. Y. Quek, L. Venkataraman, H. J. Choi, S. G. Louie, M. S. Hybertsen, and J. B. Neaton, “Amine-gold linked single-molecule circuits: Experiment and theory,” *Nano Letters*, vol. 7, no. 11, pp. 3477–3482, 2007 (pages 27, 79, 97).
- [95] M. Strange, C. Rostgaard, H. Hakkinen, and K. S. Thygesen, “Self-consistent gw calculations of electronic transport in thiol- and amine-linked molecular junctions,” *Physical Review B*, vol. 83, no. 11, p. 115 108, 2011 (page 27).
- [96] K. Wandelt, “Surface characterization by photoemission of adsorbed xenon (pax),” *Journal of Vacuum Science & Technology A*, vol. 2, no. 2, pp. 802–807, 1984 (page 28).

BIBLIOGRAPHY

- [97] K. Wandelt, W. Jacob, N. Memmel, and V. Dose, “Inverse photoemission of adsorbed xenon multilayers on ru(001): Refutation of final-state screening effects,” *Physical Review Letters*, vol. 57, no. 13, pp. 1643–1646, 1986 (page 28).
- [98] V. B. Engelkes, J. M. Beebe, and C. D. Frisbie, “Length-dependent transport in molecular junctions based on sams of alkanethiols and alkanedithiols: Effect of metal work function and applied bias on tunneling efficiency and contact resistance,” *Journal of the American Chemical Society*, vol. 126, no. 43, pp. 14 287–14 296, 2004 (pages 28, 67).
- [99] J. G. Wang, E. Prodan, R. Car, and A. Selloni, “Band alignment in molecular devices: Influence of anchoring group and metal work function,” *Physical Review B*, vol. 77, no. 24, p. 245 443, 2008 (page 28).
- [100] J. P. Perdew, K. Burke, and M. Ernzerhof, “Generalized gradient approximation made simple,” *Physical Review Letters*, vol. 77, no. 18, pp. 3865–3868, 1996 (pages 30, 76).
- [101] V. Blum, R. Gehrke, F. Hanke, P. Havu, V. Havu, X. Ren, K. Reuter, and M. Scheffler, “Ab initio molecular simulations with numeric atom-centered orbitals,” *Computer Physics Communications*, vol. 180, no. 11, pp. 2175–2196, 2009 (pages 30, 31, 45).
- [102] A. Arnold, F. Weigend, and F. Evers, “Quantum chemistry calculations for molecules coupled to reservoirs: Formalism, implementation, and application to benzenedithiol,” *Journal of Chemical Physics*, vol. 126, no. 17, p. 174 101, 2007 (page 31).
- [103] A. Bagrets, “Spin-polarized electron transport across metal-organic molecules: A density functional theory approach,” *Journal of Chemical Theory and Computation*, vol. 9, no. 6, pp. 2801–2815, 2013 (page 31).
- [104] E. v. Lenthe, E. J. Baerends, and J. G. Snijders, “Relativistic regular two-component hamiltonians,” *The Journal of Chemical Physics*, vol. 99, no. 6, pp. 4597–4610, 1993 (page 45).

BIBLIOGRAPHY

- [105] A. K. Geim and K. S. Novoselov, “The rise of graphene,” *Nature Materials*, vol. 6, no. 3, pp. 183–191, 2007 (page 48).
- [106] Y. B. Zhang, Y. W. Tan, H. L. Stormer, and P. Kim, “Experimental observation of the quantum hall effect and berry’s phase in graphene,” *Nature*, vol. 438, no. 7065, pp. 201–204, 2005 (page 48).
- [107] J. H. Chen, C. Jang, S. D. Xiao, M. Ishigami, and M. S. Fuhrer, “Intrinsic and extrinsic performance limits of graphene devices on sio₂,” *Nature Nanotechnology*, vol. 3, no. 4, pp. 206–209, 2008 (page 48).
- [108] M. J. Allen, V. C. Tung, and R. B. Kaner, “Honeycomb carbon: A review of graphene,” *Chemical Reviews*, vol. 110, no. 1, pp. 132–145, 2010 (page 48).
- [109] Y.-M. Lin, C. Dimitrakopoulos, K. A. Jenkins, D. B. Farmer, H.-Y. Chiu, A. Grill, and P. Avouris, “100-ghz transistors from wafer-scale epitaxial graphene,” *Science*, vol. 327, no. 5966, p. 662, 2010 (page 48).
- [110] C. Lee, X. D. Wei, J. W. Kysar, and J. Hone, “Measurement of the elastic properties and intrinsic strength of monolayer graphene,” *Science*, vol. 321, no. 5887, pp. 385–388, 2008 (page 48).
- [111] C. Chen, S. Rosenblatt, K. I. Bolotin, W. Kalb, P. Kim, I. Kymissis, H. L. Stormer, T. F. Heinz, and J. Hone, “Performance of monolayer graphene nanomechanical resonators with electrical readout,” *Nature Nanotechnology*, vol. 4, no. 12, pp. 861–867, 2009 (page 48).
- [112] X. Wang, L. Zhi, and K. Müllen, “Transparent, conductive graphene electrodes for dye-sensitized solar cells,” *Nano Letters*, vol. 8, no. 1, pp. 323–327, 2008 (page 48).
- [113] Z. Fei, A. S. Rodin, G. O. Andreev, W. Bao, A. S. McLeod, M. Wagner, L. M. Zhang, Z. Zhao, M. Thiemens, G. Dominguez, M. M. Fogler, A. H. C. Neto, C. N. Lau, F. Keilmann, and D. N. Basov, “Gate-tuning of graphene plasmons revealed by infrared nano-imaging,” *Nature*, vol. 487, no. 7405, pp. 82–85, 2012 (page 48).

BIBLIOGRAPHY

- [114] K. F. Mak, M. Y. Sfeir, Y. Wu, C. H. Lui, J. A. Misewich, and T. F. Heinz, “Measurement of the optical conductivity of graphene,” *Physical Review Letters*, vol. 101, no. 19, p. 196 405, 2008 (page 48).
- [115] C. Joachim and M. A. Ratner, “Molecular electronics: Some views on transport junctions and beyond,” *Proceedings of the National Academy of Sciences of the United States of America*, vol. 102, no. 25, pp. 8801–8808, 2005 (page 48).
- [116] M. L. Perrin, E. Burzuri, and H. S. van der Zant, “Single-molecule transistors,” *Chemical Society Reviews*, vol. 44, no. 4, pp. 902–919, 2015 (page 48).
- [117] M. W. Rowell, M. A. Topinka, M. D. McGehee, H.-J. Prall, G. Dennler, N. S. Sariciftci, L. Hu, and G. Gruner, “Organic solar cells with carbon nanotube network electrodes,” *Applied Physics Letters*, vol. 88, no. 23, p. 233 506, 2006 (page 48).
- [118] J. Wu, M. Agrawal, H. A. Becerril, Z. Bao, Z. Liu, Y. Chen, and P. Peumans, “Organic light-emitting diodes on solution-processed graphene transparent electrodes,” *ACS Nano*, vol. 4, no. 1, pp. 43–48, 2010 (page 48).
- [119] P. Matyba, H. Yamaguchi, G. Eda, M. Chhowalla, L. Edman, and N. D. Robinson, “Graphene and mobile ions: The key to all-plastic, solution-processed light-emitting devices,” *ACS Nano*, vol. 4, no. 2, pp. 637–642, 2010 (page 48).
- [120] L. Gomez De Arco, Y. Zhang, C. W. Schlenker, K. Ryu, M. E. Thompson, and C. Zhou, “Continuous, highly flexible, and transparent graphene films by chemical vapor deposition for organic photovoltaics,” *ACS Nano*, vol. 4, no. 5, pp. 2865–2873, 2010 (page 48).
- [121] D. Menzel, “Ultrafast charge transfer at surfaces accessed by core electron spectroscopies,” *Chemical Society Reviews*, vol. 37, no. 10, pp. 2212–2223, 2008 (page 49).
- [122] A. Föhlisch, P. Feulner, F. Hennies, A. Fink, D. Menzel, D. Sanchez-Portal, P. M. Echenique, and W. Wurth, “Direct observation of electron dynamics in the attosecond domain,” *Nature*, vol. 436, no. 7049, pp. 373–376, 2005 (page 49).

BIBLIOGRAPHY

- [123] P. Vilmercati, D. Cvetko, A. Cossaro, and A. Morgante, “Heterostructured organic interfaces probed by resonant photoemission,” *Surface Science*, vol. 603, no. 10-12, pp. 1542–1556, 2009 (pages 49, 58).
- [124] M. Weinelt, A. Nilsson, M. Magnuson, T. Wiell, N. Wassdahl, O. Karis, A. Föhlisch, N. Mårtensson, J. Stöhr, and M. Samant, “Resonant photoemission at the 2π edges of ni: Resonant raman and interference effects,” *Phys. Rev. Lett.*, vol. 78, pp. 967–970, 5 Feb. 1997 (page 49).
- [125] D. A. Racke, L. L. Kelly, H. Kim, P. Schulz, A. Sigdel, J. J. Berry, S. Graham, D. Nordlund, and O. L. A. Monti, “Disrupted attosecond charge carrier delocalization at a hybrid organic/inorganic semiconductor interface,” *The Journal of Physical Chemistry Letters*, vol. 6, no. 10, pp. 1935–1941, 2015 (page 49).
- [126] N. V. Smith, C. T. Chen, and M. Weinert, “Distance of the image plane from metal-surfaces,” *Physical Review B*, vol. 40, no. 11, pp. 7565–7573, 1989 (page 50).
- [127] L. Yang, C.-H. Park, Y.-W. Son, M. L. Cohen, and S. G. Louie, “Quasiparticle energies and band gaps in graphene nanoribbons,” *Physical Review Letters*, vol. 99, no. 18, p. 186 801, 2007 (pages 51, 55, 57).
- [128] M. Coville and T. D. Thomas, “Molecular effects on inner-shell lifetimes: Possible test of the one-center model of auger decay,” *Physical Review A*, vol. 43, no. 11, pp. 6053–6056, 1991 (page 52).
- [129] J. Schnadt, J. N. O’Shea, L. Patthey, J. Krempaský, N. Mårtensson, and P. A. Brühwiler, “Alignment of valence photoemission, x-ray absorption, and substrate density of states for an adsorbate on a semiconductor surface,” *Physical Review B*, vol. 67, no. 23, p. 235 420, 2003 (page 55).
- [130] S. Flügge, W. Mehlhorn, and V. Schmidt, “Angular distribution of auger electrons following photoionization,” *Physical Review Letters*, vol. 29, no. 1, pp. 7–9, 1972 (page 56).
- [131] E. G. Berezhko and N. M. Kabachnik, “Theoretical study of inner-shell alignment of atoms in electron impact ionisation: Angular distribution and polarisation of

BIBLIOGRAPHY

- x-rays and auger electrons,” *Journal of Physics B: Atomic and Molecular Physics*, vol. 10, no. 12, p. 2467, 1977 (page 56).
- [132] M. López, A. Gutiérrez, C. Laubschat, and G. Kaindl, “Resonant photoemission versus incoherent superposition of auger and photoemission signals,” *Journal of Electron Spectroscopy and Related Phenomena*, vol. 71, no. 1, pp. 73–77, 1995 (page 57).
- [133] L. Floreano, A. Cossaro, R. Gotter, A. Verdini, G. Bavdek, F. Evangelista, A. Ruocco, A. Morgante, and D. Cvetko, “Periodic arrays of cu-phthalocyanine chains on au(110),” *Journal of Physical Chemistry C*, vol. 112, no. 29, pp. 10 794–10 802, 2008 (page 58).
- [134] D. Cvetko, A. Lausi, A. Morgante, F. Tommasini, K. C. Prince, and M. Sastry, “Compact he beam scattering apparatus for surface studies,” *Measurement Science & Technology*, vol. 3, no. 10, pp. 997–1000, 1992 (page 58).
- [135] L. L. Patera, C. Africh, R. S. Weatherup, R. Blume, S. Bhardwaj, C. Castellarin-Cudia, A. Knop-Gericke, R. Schloegl, G. Comelli, S. Hofmann, and C. Cepek, “In situ observations of the atomistic mechanisms of ni catalyzed low temperature graphene growth,” *ACS Nano*, vol. 7, no. 9, pp. 7901–7912, 2013 (page 58).
- [136] A. Batra, D. Cvetko, G. Kladnik, O. Adak, C. Cardoso, A. Ferretti, D. Prezzi, E. Molinari, A. Morgante, and L. Venkataraman, “Probing the mechanism for graphene nanoribbon formation on gold surfaces through x-ray spectroscopy,” *Chemical Science*, vol. 5, p. 4419, 2014 (pages 59, 126).
- [137] O. Adak, E. Rosenthal, J. Meisner, E. F. Andrade, A. N. Pasupathy, C. Nuckolls, M. S. Hybertsen, and L. Venkataraman, “Flicker noise as a probe of electronic interaction at metal-single molecule interfaces,” *Nano Letters*, vol. 15, no. 6, pp. 4143–4149, 2015 (pages 66, 126).
- [138] S. Braun, W. R. Salaneck, and M. Fahlman, “Energy-level alignment at organic/metal and organic/organic interfaces,” *Advanced Materials*, vol. 21, no. 14–15, pp. 1450–1472, 2009 (page 67).

BIBLIOGRAPHY

- [139] D. Cahen and A. Kahn, “Electron energetics at surfaces and interfaces: Concepts and experiments,” *Advanced Materials*, vol. 15, no. 4, pp. 271–277, 2003 (page 67).
- [140] R. Hoffmann, “Interaction of orbitals through space and through bonds,” *Accounts of Chemical Research*, vol. 4, no. 1, pp. 1–9, 1971 (page 67).
- [141] S. M. Wu, M. T. Gonzalez, R. Huber, S. Grunder, M. Mayor, C. Schonenberger, and M. Calame, “Molecular junctions based on aromatic coupling,” *Nature Nanotechnology*, vol. 3, no. 9, pp. 569–574, 2008 (page 67).
- [142] J. S. Meisner, S. Ahn, S. V. Aradhya, M. Krikorian, R. Parameswaran, M. Steigerwald, L. Venkataraman, and C. Nuckolls, “Importance of direct metal- π -coupling in electronic transport through conjugated single-molecule junctions,” *Journal of the American Chemical Society*, vol. 134, no. 50, pp. 20 440–20 445, 2012 (pages 67, 70, 77, 78, 95).
- [143] G. S. Tulevski, Q. Miao, A. Afzali, T. O. Graham, C. R. Kagan, and C. Nuckolls, “Chemical complementarity in the contacts for nanoscale organic field-effect transistors,” *Journal of the American Chemical Society*, vol. 128, no. 6, pp. 1788–1789, 2006 (page 68).
- [144] R. Ochs, D. Secker, M. Elbing, M. Mayor, and H. B. Weber, “Fast temporal fluctuations in single-molecule junctions,” *Faraday Discussions*, vol. 131, pp. 281–289, 2006 (pages 68, 70).
- [145] M. Tsutsui, M. Taniguchi, and T. Kawai, “Single-molecule identification via electric current noise,” *Nature Communications*, vol. 1, p. 138, 2010 (pages 68, 70).
- [146] V. A. Sydoruk, D. Xiang, S. A. Vitusevich, M. V. Petrychuk, A. Vladyska, Y. Zhang, A. Offenhausser, V. A. Kochelap, A. E. Belyaev, and D. Mayer, “Noise and transport characterization of single molecular break junctions with individual molecule,” *Journal of Applied Physics*, vol. 112, no. 1, p. 014 908, 2012 (pages 68, 70).

BIBLIOGRAPHY

- [147] D. Xiang, T. Lee, Y. Kim, T. Mei, and Q. Wang, “Origin of discrete current fluctuations in a single molecule junction,” *Nanoscale*, vol. 6, no. 22, pp. 13 396–13 401, 2014 (page [68](#)).
- [148] H. E. van den Brom and J. M. van Ruitenbeek, “Quantum suppression of shot noise in atom-size metallic contacts,” *Physical Review Letters*, vol. 82, no. 7, pp. 1526–1529, 1999 (pages [68](#), [86](#)).
- [149] A. Sperl, J. Kröger, and R. Berndt, “Direct observation of conductance fluctuations of a single-atom tunneling contact,” *Physical Review B*, vol. 81, no. 3, p. 035 406, 2010 (pages [71](#), [90](#)).
- [150] M. Tsutsui, S. Kurokawa, and A. Sakai, “Bias-induced local heating in atom-sized metal contacts at 77 k,” *Applied Physics Letters*, vol. 90, no. 13, p. 133 121, 2007 (pages [71](#), [90](#)).
- [151] K. Hubert, L. Thomas, Z. Remi, D. Philippe, and S. Andres, “Conductance fluctuations in gold point contacts: An atomistic picture,” *Nanotechnology*, vol. 23, no. 23, p. 235 707, 2012 (pages [71](#), [90](#)).
- [152] F. N. Hooge and P. A. Bobbert, “On the correlation function of 1/f noise,” *Physica B*, vol. 239, no. 3-4, pp. 223–230, 1997 (page [72](#)).
- [153] J. Armstrong, R. Schaub, S. Hua, and H. Chopra, “Channel saturation and conductance quantization in single-atom gold constrictions,” *Physical Review B*, vol. 82, no. 19, p. 195 416, 2010 (page [72](#)).
- [154] P. Hänggi, P. Talkner, and M. Borkovec, “Reaction-rate theory: Fifty years after kramers,” *Reviews of Modern Physics*, vol. 62, no. 2, pp. 251–341, 1990 (pages [74](#), [81](#)).
- [155] T. N. Todorov, “Local heating in ballistic atomic-scale contracts,” *Phil. Mag. B*, vol. 77, no. 4, pp. 965–973, 1998 (page [74](#)).

BIBLIOGRAPHY

- [156] C. J. Muller, J. M. van Ruitenbeek, and L. J. de Jongh, “Conductance and supercurrent discontinuities in atomic-scale metallic constrictions of variable width,” *Physical Review Letters*, vol. 69, no. 1, pp. 140–143, 1992 (pages 75, 90).
- [157] G. Kresse and J. Furthmüller, “Efficient iterative schemes for ab initio total-energy calculations using a plane-wave basis set,” *Physical Review B*, vol. 54, no. 16, p. 11 169, 1996 (page 76).
- [158] G. Kresse and D. Joubert, “From ultrasoft pseudopotentials to the projector augmented-wave method,” *Physical Review B*, vol. 59, no. 3, pp. 1758–1775, 1999 (page 76).
- [159] P. E. Blochl, “Projector augmented-wave method,” *Physical Review B*, vol. 50, no. 24, pp. 17 953–17 979, 1994 (page 76).
- [160] R. Chen, P. J. Wheeler, and D. Natelson, “Excess noise in STM-style break junctions at room temperature,” *Physical Review B*, vol. 85, no. 23, p. 235 455, 2012 (pages 77, 86).
- [161] S. V. Aradhya, J. S. Meisner, M. Krikorian, S. Ahn, R. Parameswaran, M. L. Steigerwald, C. Nuckolls, and L. Venkataraman, “Dissecting contact mechanics from quantum interference in single-molecule junctions of stilbene derivatives,” *Nano Letters*, vol. 12, no. 3, pp. 1643–1647, 2012 (page 78).
- [162] H. Basch, R. Cohen, and M. A. Ratner, “Interface geometry and molecular junction conductance: Geometric fluctuation and stochastic switching,” *Nano Letters*, vol. 5, no. 9, pp. 1668–1675, 2005 (page 79).
- [163] W. Tian, S. Datta, S. Hong, R. Reifenberger, J. I. Henderson, and C. P. Kubiak, “Conductance spectra of molecular wires,” *The Journal of Chemical Physics*, vol. 109, no. 7, pp. 2874–2882, 1998 (page 79).
- [164] M. Kamenetska, M. Koentopp, A. Whalley, Y. S. Park, M. Steigerwald, C. Nuckolls, M. Hybertsen, and L. Venkataraman, “Formation and evolution of single-molecule junctions,” *Physical Review Letters*, vol. 102, no. 12, p. 126 803, 2009 (pages 79, 81).

BIBLIOGRAPHY

- [165] Z. J. Donhauser, B. A. Mantooth, K. F. Kelly, L. A. Bumm, J. D. Monnell, J. J. Stapleton, D. W. Price, A. M. Rawlett, D. L. Allara, J. M. Tour, and P. S. Weiss, “Conductance switching in single molecules through conformational changes,” *Science*, vol. 292, no. 5525, pp. 2303–2307, 2001 (page 79).
- [166] R. S. Mulliken and C. C. J. Roothaan, “The twisting frequency and the barrier height for free rotation in ethylene,” *Chemical Reviews*, vol. 41, no. 2, pp. 219–231, 1947 (page 80).
- [167] Y. S. Park, J. R. Widawsky, M. Kamenetska, M. L. Steigerwald, M. S. Hybertsen, C. Nuckolls, and L. Venkataraman, “Frustrated rotations in single-molecule junctions,” *Journal of the American Chemical Society*, vol. 131, no. 31, pp. 10 820–10 821, 2009 (pages 81, 99, 100).
- [168] A. Batra, P. T. Darancet, Q. Chen, J. Meisner, J. R. Widawsky, J. B. Neaton, C. Nuckolls, and L. Venkataraman, “Tuning rectification in single-molecular diodes,” *Nano Letters*, vol. 13, no. 12, pp. 6233–7, 2013 (page 95).
- [169] Y. S. Park, A. C. Whalley, M. Kamenetska, M. L. Steigerwald, M. S. Hybertsen, C. Nuckolls, and L. Venkataraman, “Contact chemistry and single- molecule conductance: A comparison of phosphines, methyl sulfides, and amines,” *Journal of the American Chemical Society*, vol. 129, no. 51, pp. 15 768–15 769, 2007 (page 100).
- [170] S. Kohler, J. Lehmann, and P. Hänggi, “Driven quantum transport on the nanoscale,” *Physics Reports*, vol. 406, no. 6, pp. 379–443, 2005 (pages 103, 105).
- [171] G. Platero and R. Aguado, “Photon-assisted transport in semiconductor nanostructures,” *Physics Reports*, vol. 395, no. 1-2, pp. 1–157, 2004 (pages 103, 105, 106).
- [172] B. Pettinger, B. Ren, G. Picardi, R. Schuster, and G. Ertl, “Nanoscale probing of adsorbed species by tip-enhanced raman spectroscopy,” *Physical Review Letters*, vol. 92, no. 9, p. 096 101, 2004 (pages 103, 104).
- [173] A. Campion and P. Kambhampati, “Surface-enhanced raman scattering,” *Chemical Society Reviews*, vol. 27, no. 4, pp. 241–250, 1998 (pages 103, 104).

BIBLIOGRAPHY

- [174] A. Giugni, B. Torre, A. Toma, M. Francardi, M. Malerba, A. Alabastri, R. Proietti Zaccaria, M. I. Stockman, and E. Di Fabrizio, “Hot-electron nanoscopy using adiabatic compression of surface plasmons,” *Nature Nanotechnology*, vol. 8, no. 11, pp. 845–852, 2013 (pages [103](#), [104](#)).
- [175] S. Lal, S. Link, and N. J. Halas, “Nano-optics from sensing to waveguiding,” *Nat Photon*, vol. 1, no. 11, pp. 641–648, 2007 (pages [103](#), [104](#)).
- [176] E. Ozbay, “Plasmonics: Merging photonics and electronics at nanoscale dimensions,” *Science*, vol. 311, no. 5758, pp. 189–193, 2006 (pages [103](#), [104](#)).
- [177] Z. Junxi, Z. Lide, and X. Wei, “Surface plasmon polaritons: Physics and applications,” *Journal of Physics D: Applied Physics*, vol. 45, no. 11, p. 113 001, 2012 (pages [103](#), [104](#)).
- [178] M. Lenner, P. Rácz, P. Dombi, G. Farkas, and N. Kroó, “Field enhancement and rectification of surface plasmons detected by scanning tunneling microscopy,” *Physical Review B*, vol. 83, no. 20, p. 205 428, 2011 (page [103](#)).
- [179] N. Ittah, G. Noy, I. Yutsis, and Y. Selzer, “Measurement of electronic transport through 1g0 gold contacts under laser irradiation,” *Nano Letters*, vol. 9, no. 4, pp. 1615–1620, 2009 (page [103](#)).
- [180] D. Benner, J. Boneberg, P. Nürnberg, R. Waitz, P. Leiderer, and E. Scheer, “Lateral and temporal dependence of the transport through an atomic gold contact under light irradiation: Signature of propagating surface plasmon polaritons,” *Nano Letters*, vol. 14, no. 9, pp. 5218–5223, 2014 (page [103](#)).
- [181] D. C. Guhr, D. Rettinger, J. Boneberg, A. Erbe, P. Leiderer, and E. Scheer, “Influence of laser light on electronic transport through atomic-size contacts,” *Physical Review Letters*, vol. 99, no. 8, p. 086 801, 2007 (page [103](#)).
- [182] H. Q. Nguyen, P. H. Cutler, T. E. Feuchtwang, Z. H. Huang, Y. Kuk, P. J. Silverman, A. A. Lucas, and T. E. Sullivan, “Mechanisms of current rectification in an stm tunnel junction and the measurement of an operational tunneling time,”

BIBLIOGRAPHY

- Electron Devices, IEEE Transactions on*, vol. 36, no. 11, pp. 2671–2678, 1989 (page 103).
- [183] A. V. Bragas, S. M. Landi, and O. E. Martinez, “Laser field enhancement at the scanning tunneling microscope junction measured by optical rectification,” *Applied Physics Letters*, vol. 72, no. 17, pp. 2075–2077, 1998 (page 103).
- [184] D. R. Ward, F. Huser, F. Pauly, J. C. Cuevas, and D. Natelson, “Optical rectification and field enhancement in a plasmonic nanogap,” *Nat Nano*, vol. 5, no. 10, pp. 732–736, 2010 (page 103).
- [185] R. Arielly, A. Ofarim, G. Noy, and Y. Selzer, “Accurate determination of plasmonic fields in molecular junctions by current rectification at optical frequencies,” *Nano Letters*, vol. 11, no. 7, pp. 2968–2972, 2011 (page 103).
- [186] M. Vadai, N. Nachman, M. Ben-Zion, M. Bürkle, F. Pauly, J. C. Cuevas, and Y. Selzer, “Plasmon-induced conductance enhancement in single-molecule junctions,” *The Journal of Physical Chemistry Letters*, vol. 4, no. 17, pp. 2811–2816, 2013 (page 103).
- [187] P. Uri, “An introduction to the formulation of steady-state transport through molecular junctions,” *Journal of Physics B: Atomic, Molecular and Optical Physics*, vol. 43, no. 15, p. 153001, 2010 (page 104).
- [188] W. L. Barnes, A. Dereux, and T. W. Ebbesen, “Surface plasmon subwavelength optics,” *Nature*, vol. 424, no. 6950, pp. 824–830, 2003 (page 104).
- [189] R. Huber, M. Koch, and J. Feldmann, “Laser-induced thermal expansion of a scanning tunneling microscope tip measured with an atomic force microscope cantilever,” *Applied Physics Letters*, vol. 73, no. 17, pp. 2521–2523, 1998 (page 108).
- [190] S. Grafström, P. Schuller, J. Kowalski, and R. Neumann, “Thermal expansion of scanning tunneling microscopy tips under laser illumination,” *Journal of Applied Physics*, vol. 83, no. 7, pp. 3453–3460, 1998 (page 108).

BIBLIOGRAPHY

- [191] P. B. Johnson and R. W. Christy, “Optical constants of the noble metals,” *Physical Review B*, vol. 6, no. 12, pp. 4370–4379, 1972 (page [110](#)).
- [192] B. Pettinger, K. F. Domke, D. Zhang, G. Picardi, and R. Schuster, “Tip-enhanced raman scattering: Influence of the tip-surface geometry on optical resonance and enhancement,” *Surface Science*, vol. 603, no. 1012, pp. 1335–1341, 2009 (page [111](#)).
- [193] B. Pettinger, P. Schambach, C. J. Villagomez, and N. Scott, “Tip-enhanced raman spectroscopy: Near-fields acting on a few molecules,” *Annual Review of Physical Chemistry*, vol. 63, no. 1, pp. 379–399, 2012 (page [115](#)).
- [194] D. J. Park, B. Piglosiewicz, S. Schmidt, H. Kollmann, M. Mascheck, P. GroSS, and C. Lienau, “Characterizing the optical near-field in the vicinity of a sharp metallic nanoprobe by angle-resolved electron kinetic energy spectroscopy,” *Annalen der Physik*, vol. 525, no. 1-2, pp. 135–142, 2013 (page [115](#)).
- [195] R. Bormann, M. Gulde, A. Weismann, S. V. Yalunin, and C. Ropers, “Tip-enhanced strong-field photoemission,” *Phys. Rev. Lett.*, vol. 105, no. 14, p. 147601, 2010 (page [115](#)).
- [196] C. Ropers, D. R. Solli, C. P. Schulz, C. Lienau, and T. Elsaesser, “Localized multi-photon emission of femtosecond electron pulses from metal nanotips,” *Phys. Rev. Lett.*, vol. 98, p. 043907, 2007 (page [115](#)).
- [197] O. Adak, D. Scarabelli, and L. Venkataraman, “Evidence for optically induced charge transfer through single-molecule junctions.,” In preparation (page [126](#)).
- [198] O. Adak, G. Kladnik, G. Bavdek, A. Cossaro, A. Morgante, D. Cvetko, and L. Venkataraman, “Ultrafast bidirectional charge transport and electron decoherence at molecule/surfaces interfaces: A comparison of gold, graphene and graphene nanoribbon surfaces,” Submitted (page [126](#)).
- [199] B. Capozzi, J. Xia, O. Adak, E. J. Dell, Z.-F. Liu, J. C. Taylor, J. B. Neaton, L. M. Campos, and L. Venkataraman, “Single-molecule diodes with high rectification ratios through environmental control,” *Nat Nano*, vol. 10, no. 6, pp. 522–527, 2015 (page [126](#)).

BIBLIOGRAPHY

- [200] Z.-F. Liu, S. Wei, H. Yoon, O. Adak, I. Ponce, Y. Jiang, W.-D. Jang, L. M. Campos, L. Venkataraman, and J. B. Neaton, “Control of single-molecule junction conductance of porphyrins via a transition-metal center,” *Nano Letters*, vol. 14, no. 9, pp. 5365–5370, 2014 (page 127).